Università degli Studi di Padova

Head Office: Università degli Studi di Padova

Department of Geosciences

Ph.D. COURSE IN: Geosciences
XXXV SERIES

Former melt inclusions in garnet from UHP gneisses of the Seve Nappe Complex, Scandinavian Caledonides

Coordinator: Prof. Claudia Agnini

Supervisor: Prof. Bernardo Cesare

Co-Supervisor: Prof. Omar Bartoli

Co-Supervisor: Prof. Jaroslaw Majka

Ph.D. student: Pawel Michal Slupski

"The only real failure is the failure to try, and the measure of success is how we cope with disappointment, as we always must."

From the movie: The Best Exotic Marigold Hotel, and email footnote of my supervisor Prof. Bernardo Cesare

Abstract

Ultrahigh pressure (UHP) metamorphism has been recently reported in gneisses from the Seve Nappe Complex (SNC) of the Scandinavian Caledonides. This study is focused on crystallized former melt inclusions - so-called *nanogranitoids* - and the information they preserve about anatectic processes occurring during ultradeep subduction. Nanogranitoids (NG) are small (< 20 µm) fully crystallized droplets of anatectic melt entrapped in peritectic phases. Paragneisses from the Åreskutan Mountain representing the SNC are part of the outermost Baltica margin, which has been subducted, metamorphosed, and melted during the closure of the Iapetus Ocean in Middle Ordovician. Closure of Iapetus Ocean led to subsequent collision between Baltica and Laurentia in Early Devonian.

The mineral assemblage of the paragneiss is K-feldspar, garnet, quartz, plagioclase, biotite, white mica, kyanite, sillimanite and rutile. Clusters of inclusions are composed of small (< 5 µm) multiphase inclusions (MPI). MPI represents former fluid inclusion and consists of carbonates, micas, pyrophyllite, kaolinite, quartz, graphite, diamond, rutile, and a residual fluid made of CO_2, CH_4 and N_2. Within the clusters MPI occur with larger (5 – 20 µm) and rarer NG inclusions, composed of quartz, biotite, K-feldspar, plagioclase and rarely carbonates.

Seven re-homogenization experiments at different P-T conditions were conducted in a multi-anvil apparatus to remelt nanogranitoids and determine the composition of the anatectic melt. The best homogenization was acquired at 850, 900˚C and 4, 4.5 GPa. The entrapped melt is mostly rhyolitic in composition, with a high alkali content (~10 wt% N_2O+K_2O). The H_2O and CO_2 content of the remelted nanogranitoids analysed by NanoSIMS are respectively ~4.6 wt% (3.3 – 6.6 wt%) and ~0.88 wt% (0.12 – 2.11 wt%). The chemical composition of reconstructed anatectic melt from paragneisses of SNC is consistent with experimental studies of UHP melts. Twp partial melting events in Åreskutan Mountain, SNC have been recognized, one at eclogite-facies conditions and the second at granulite-facies conditions (441 Ma).

Riassunto

Il metamorfismo ad altissima pressione (UHP) è stato recentemente riportato negli gneiss del complesso Seve Nappe (SNC) dei Caledonidi scandinavi. Questo studio è incentrato sulle inclusioni fuse cristallizzate - noti come nanogranitoidi - e sulle informazioni che esse conservano sui processi anatettici che si verificano durante la subduzione ultraprofonda. I nanogranitoidi (NG) sono piccole gocce (< 20 µm) completamente cristallizzate di fusione anatettica intrappolate in fasi peritettiche. I paragneiss del Monte Åreskutan che rappresentano il SNC fanno parte del margine più esterno del Baltica, che è stato subdotto, metamorfosato e fuso durante la chiusura dell'Oceano Iapeto, che ha causato la collisione tra la Baltica e la Laurentia nel periodo del primo Devoniano.

L'insieme dei minerali del paragneiss è costituito da K-feldspato, granato, quarzo, plagioclasio, biotite, mica bianca, cianite, sillimanite e rutilo. Gli ammassi di inclusioni sono composti da piccole (< 5 µm) inclusioni multifase (MPI). Le MPI rappresentano precedenti inclusioni fluide e sono costituite da carbonati, micas, pirofillite, caolinite ± quarzo, grafite, rutilo e da un residuo liquido composto da CO_2, CH_4 e N_2. Nei cluster MPI sono presenti inclusioni NG più grandi (5 - 20 µm) e più rare, composte da quarzo, biotite, K-feldspato, plagioclasio e raramente da carbonati.

Sono stati condotti sette esperimenti di riomogenizzazione a diverse condizioni di P-T attraverso un apparato multi-anvil per rifondere i nanogranitoidi e determinare la composizione del fuso anatettico. L'omogeneizzazione migliore è stata acquisita a 850 - 900˚C e 4 - 4,5 GPa. La composizione del fuso intrappolato è prevalentemente riolitica, con un elevato contenuto di alcali (~10 wt% N_2O+K_2O). I contenuti di H_2O e CO2 dei nanogranitoidi rifusi, analizzati mediante NanoSIMS, sono rispettivamente ~ 4,6 wt% (3,3 - 6,6 wt%) e ~0,88 wt% (0,12 - 2,11 wt%). La composizione chimica della fusione anatettica proveniente dai paragneiss della SNC è coerente con gli studi sperimentali sui fusi UHP. Sono stati riconosciuti due eventi di fusione parziale nel Monte Åreskutan, SNC, uno in condizioni di eclogite-facies e il secondo in condizioni di granulite-facies (441 Ma).

Table of Contents

Abstract ii

Riassunto iii

Table of Contents iv

Chapter I Partial melting (anatexis) at ultrahigh pressure conditions 1

1.1 Ultrahigh pressure metamorphism 1

1.2 Anatexis of metapelites at UHP conditions 3

1.3 Former melt and fluid inclusions 6

1.4 Aim of the study 7

Chapter II Geological background 8

2.1 The Caledonian Orogen 8

2.2 The Scandinavian Caledonides 8

2.3 Åreskutan Nappes 11

Chapter III Analytical methods 12

Chapter IV Petrography of the paragneiss 19

4.1 Macroscopic description 19

4.2 Garnet 21

4.3 K-feldspar 22

4.4 Plagioclase 22

4.5 Aluminosilicates 23

4.6 Quartz 25

4.7 Micas 25

4.8 Rutile 25

4.9 Other phases 26

4.10 Melt pseudomorphs 28
4.11 Deformation 30
Chapter V Mineral chemistry 32
5.1 Garnet 32
5.3 Feldspars 37
5.4 Biotite 38
5.5 Muscovite 39
5.6 Rutile 40
5.7 Zr-in-Rutile thermometry 43
Chapter VI Nanogranitoids, multiphase inclusions and diamonds in garnet 46
6.1 Occurrence of inclusions 46
6.2 Nanogranitoids 48
6.3 Multiphase inclusions 50
6.4 Metamorphic diamond in MPI 53
Chapter VII Re-melting experiments and melt composition 55
7.1 Homogenization of nanogranitoids 55
7.3 Composition of UHP anatectic melt 58
7.4 Volatile content of remelted nanogranitoids 63
Chapter VIII Discussion 67
8.1 Composition of UHP melts 67
8.2 Volatiles in UHP melts 72
8.3 Record of UHP fluid 75
8.4 Metamorphic evolution and partial melting in Åreskutan gneiss 79
8.5 Fate of UHP melts 86

8.6 Concluding remarks and future developments 88

Acknowledgments 90

References 91

Appendix 110

Chapter I

Partial melting (anatexis) at ultrahigh pressure conditions

1.1 Ultrahigh pressure metamorphism

The discovery of coesite (high-pressure polymorph of SiO_2) and diamond in gneisses (Chopin, 1984; Sobolev and Shatsky, 1990) has demonstrated that buoyant crustal material might be subducted to mantle depth experiencing pressures >2.7 GPa and 4 GPa, respectively. These pressures correspond to >100 km depth, significantly deeper than the thickest crust ~75 km depth that represents ~2 GPa (Fig. 1.1). The thickest crust (~75 km) is observed below large continental collision zones, e.g. Himalayas or Alps (Christensen and Mooney, 1995). The identification of coesite opened a new field of research in petrology, the so-called "ultrahigh-pressure metamorphism (UHP)". UHP metamorphism is defined by quartz-to-coesite phase transition (Fig. 1.1). See also classification of metamorphic facies by Brown (2007).

In the last decades substantial effort has been made to recognize and characterize UHP terranes. The main UHP terranes investigated so far are the Dora Maira Massif in Western Alps, Italy (Compagnoni and Rolfo, 2003), Western Gneiss Region, Norway (Carswell et al., 1999), Kokchetav Massif, Kazakhstan (Shatsky and Sobolev, 2003), Dabie-Sulu, China (Hirajima and Nakamura, 2003; Zhang et al., 2009), recently recognized Seve Nappe Complex in Scandinavian Caledonides, Sweden (Janák et al., 2013; Majka et al., 2014; Klonowska et al., 2017; Bukała et al., 2018; Petrík et al., 2019). For more UHP occurrences see the review of Liou et al. (2009) and Gilotti, (2013)

The number of features indicating that rock experienced UHP metamorphism has been revised and described by Chopin (2003); Hacker et al. (2006); Dobrzhinetskaya et al. (2011); Hermann and Rubatto (2014). One of the most direct and robust evidence for UHP metamorphism is the presence of metamorphic diamond (see graphite-to-diamond transition boundary in Fig. 1.1a). This transition (Gr-to-Dia) is sluggish, as

demonstrated by experimental studies (Kennedy and Kennedy, 1976). The occurrence of microdiamonds coexisting with graphite in natural rocks supports this experimental observations (Korsakov and Hermann, 2006; Klonowska et al., 2017). Conversely, coesite that tends to recrystallize quickly to quartz, as pressure drops and temperature remains above 400˚C (Perrillat, 2003). The significant volume change resulted from the coesite-quartz transition causes the formation of characteristic radial cracks around former coesite inclusions in stiff minerals (Chopin, 2003). However, the presence of radial cracks around quartz cannot be considered decisive evidence for determination of the UHP metamorphism (Chopin, 2003). Therefore, if the rock reached the stability field of diamond and the metamorphic diamond has crystallized, it will have much higher chance to survive the retrograde metamorphic re-equilibration (Hermann and Rubatto 2014).

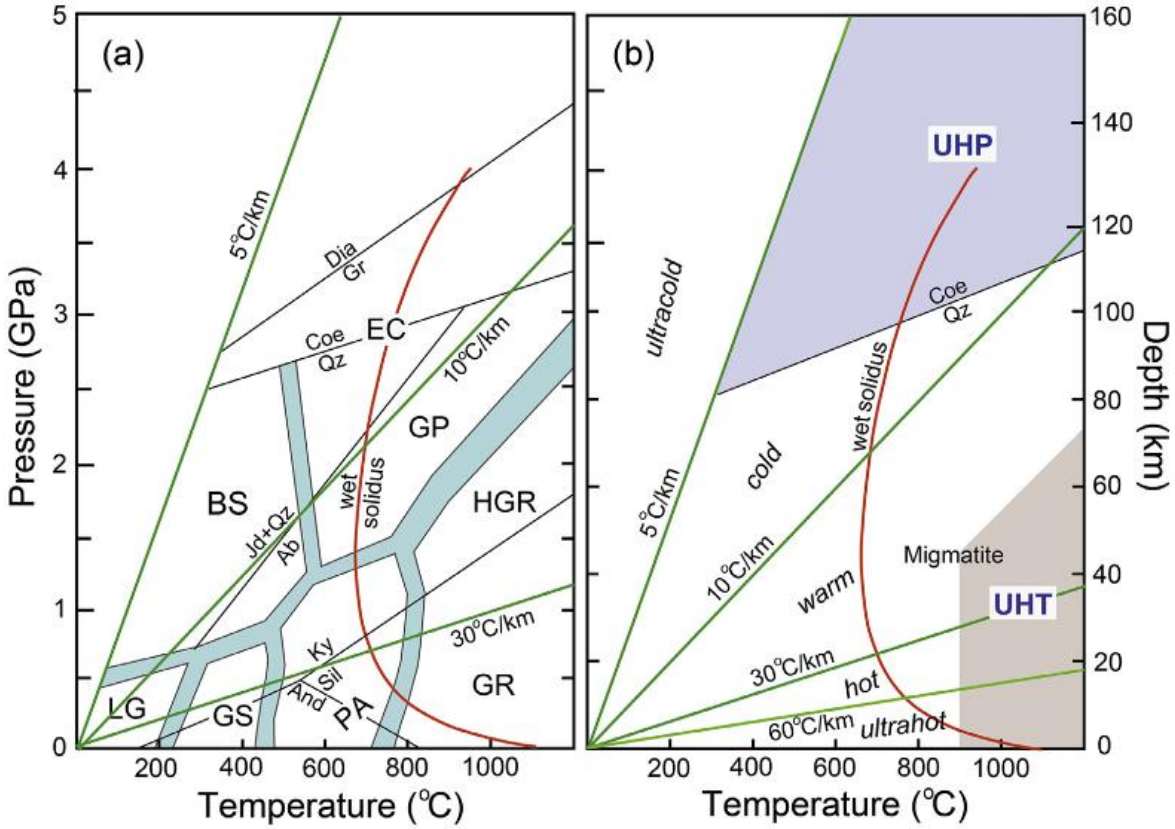

Figure 1.1 The pressure-temperature diagrams of metamorphic facies in terms of petrology **(a)** and tectonics **(b)**, with P-T fields for given mineral assemblages, taken from Zheng (2019). The vertical axes represent the pressure (a) and equivalent in depth (b). Bands delineating fields in (a) show variety with respect to different bulk rock composition of lithologies. Green lines in (b) show the thermal gradients of subduction zone processes, the red line indicate wet solidus for granite. Mineral abbreviation

according to Whitney and Evans (2010). GS – greenschist facies; BS – blueschist facies; EC – eclogite facies; UHP – ultrahigh pressure facies; GP – garnet pyroxenite facies; HGR – high pressure granulite facies; GR – granulite facies; PA – plagioclase amphibolite facies; UHT – ultrahigh temperature facies.

1.2 Anatexis of metapelites at UHP conditions

Partial melting (anatexis) in the lower crust was extensively studied over the years, recently reviewed by Clemens et al. (2020). These studies provided a better understanding of melt generation, extraction and, ascent to upper levels which drives chemical differentiation (Brown et al., 2011; Sawyer et al., 2011), weakening of the continental crust, and affect the tectonic processes (Jamieson et al., 2011).

Partial melting occurs when a portion of the rock changes its state from solid to liquid and forms two-phase system. This process is controlled by four crucial parameters: 1) pressure, 2) temperature, 3) content of volatiles, and 4) chemical composition of the system. The solid part of the unmelted rock is called residuum (Sawyer, 2008), while the liquid part is called melt (Vielzeuf et al., 1990; Clemens, 2006). The portion crystallized from the melt is called leucosome, while the residual part melanosome. The melt segregation and extraction might occur to various degree, therefore newly formed portion of the rock consisting of residuum and crystalized melt with not well-pronounced differentiation is called neosome.

The melts formed by anatexis of continental crustal rocks can form small droplets along grain boundary (Fig. 1.2a), with progressive melting they can connect to form intragranular films (Fig. 1.2b), then migrate along foliation planes accumulating in pockets (Fig. 1.2c) and finally coalescence into melt channels (Fig. 1.2d). The result of this process might be formation of residual (metasedimentary) granulitic bodies in the lower crust, S-type granites in mid-upper crust or felsic lavas. Alternatively, melts can interact with ultramafic rocks from the mantle wedge causing induced metasomatism, partial melting of the mantle, or ascent and mix. Introducing crustal signatures to the mantle rocks and melts. (Spandler et al., 2010; Spandler and Pirard, 2013; Campbell et al., 2014). Experimental studies have demonstrated that even a low percentage of anatectic melts can significantly reduce the rheological strength of crustal rocks and

promote localization of the strain (Rosenberg and Handy, 2005; Ganzhorn et al., 2014). Therefore, the presence of melt can promote, or initiate exhumation of deeply subducted continental chunks (Labrousse et al., 2011, 2015).

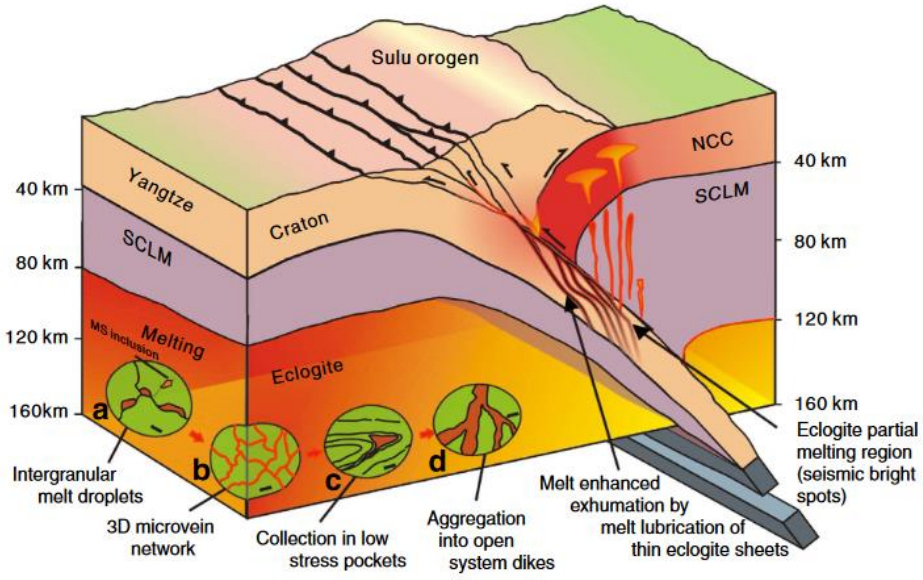

Figure 1.2 Model showing partial melting of subducted crustal rocks and formation of melt channels on example of Sulu Orogen, after Wang et al. (2014). The elliptical insets a-d represent progressive stages of anatexis of deeply subducted crust. Subducted rock initiates partial melting by formation of melt droplets along grain boundary (**a**, scale bar 50 µm), which connect into intergranular veinlets (**b**, scale bar 1 cm), then migrate along foliation planes, accumulating as melt pockets in low stress zones (**c**, scale bar 10 cm). This process finally leads to merging of melt pockets and formation of melt channels (**d**, scale bar 1 m) and magma transportation to higher lithospheric levels. SCLM, subcontinental lithospheric mantle, NCC, North China Craton.

Anatexis at UHP conditions is controlled mostly by accessibility of H_2O it may be initiated by saturation of percolating fluid (H_2O present melting) or by dehydration of phases present in the rock (dehydration melting). In the case of UHP rocks the main hydrous phase is phengite, therefore, stability of this phase controls initiation of anatexis (Schmidt et al., 2004). Phengite breakdown reaction was experimentally defined by Schmidt et al. (2004) and its position prevents melting during the UHP prograde metamorphism in the fluid absent system. Partial melting is expected to occur during the retrograde path for rocks experiencing temperature above 750˚C, which was observed in Erzgebirge and Kokchetav Massif (Hermann and Rubatto, 2014).

As concerns melting at UHP, experimental studies conducted by Nichols et al. (1994), Johnson and Plank (2000); Schmidt et al. (2004), Auzanneau et al. (2006), Hermann and Spandler (2008) have constrained the position of the wet solidus boundaries for metapelites up to 5.5 GPa (Fig. 1.3). These constraints have demonstrated that the wet solidus boundary might be easily crossed by subducting crustal rocks and stay in the supra-solidus field during the prograde and retrograde path. Therefore, depending on the temperature, composition of the rock, presence of H_2O melting may occur at UHP conditions.

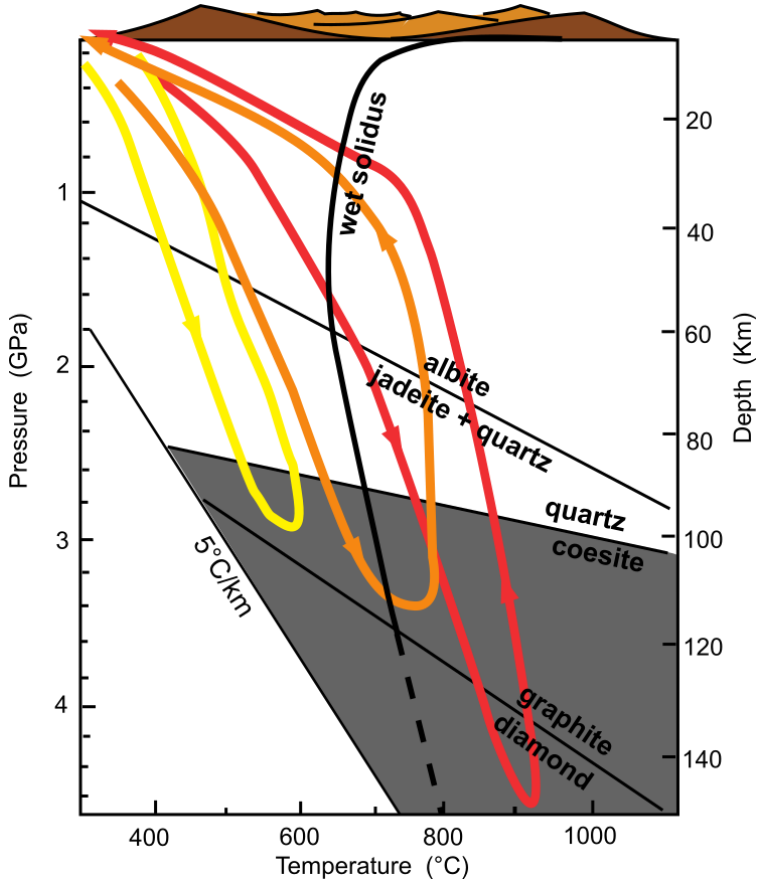

Figure 1.3 Pressure – temperature space diagram showing UHP metamorphism field (grey), and examples of P-T paths, modified after Gilotti (2013). The position of wet solidus is taken from Hermann and Spandler (2008).

1.3 Former melt and fluid inclusions

Extensive studies of melt inclusions in the last 30 years resulted with development of a new approach to study anatectic processes in situ in metamorphic rocks (Cesare et al., 2009; Ferrero et al., 2012; Bartoli et al., 2013a), reviewed by (Cesare et al., 2015; Ferrero et al., 2018). The main objects of these studies are small droplets (10 - 20 μm in diameter) of melt trapped in peritectic phases (e.g., garnet) during their growth in the presence of melt. Those small droplets of melt can crystallize during cooling, forming aggregates of minerals that resemble granites in mineral and chemical composition. Therefore, they are called 'nanogranites' (Cesare et al., 2009). Further studies on high-grade metamorphic rocks worldwide resulted in the discovery of trapped melts with wider compositions, therefore the new names were proposed to include more compositional variety of inclusions – 'nanogranitoids' and 'nanorocks' (Cesare et al., 2015; Bartoli et al., 2016; Bartoli and Cesare, 2020).

Nanogranitoids (NG) were found, characterized, and successfully remelted in high-grade metamorphic rocks reaching near UHP conditions (Ferrero et al., 2015; Bartoli et al., 2016). So far, there is only few studies that recovered the primary natural melt composition from UHP rocks by NG experimental re-homogenization (Stepanov et al., 2016; Acosta-vigil et al., 2017; Borghini et al., 2023).

Alongside entrapped melt inclusions i.e., NGs, small droplets of COH-fluid might be trapped as well (Ferrero et al., 2014, 2016). Primary fluid inclusions interact with hosting phase e.g., garnet upon cooling crystalizing stepdaughter solid phases (Carvalho et al., 2020). Inclusions composed of solids crystalized from the fluid interacting with garnet are called multiphase inclusions (MPI). They are similar in texture to NGs (e.g. negative crystal shape). Presence of NGs and MPIs together is strong microstructural evidence for fluid and melt immiscibility during the entrapment. Mineral composition, texture and the origin of MPIs were described by Tacchetto et al. (2019), and Carvalho et al. (2019, 2020).

1.4 Aim of the study

This multidisciplinary study is focused mainly on understanding how anatexis takes place during the ultradeep subduction and how fluids, melts and rocks are interacting with each other at UHP conditions. Dia-bearing migmatitic paragneisses from Åreskutan in Seve Nappe Complex of the Scandinavian Caledonides were selected to investigate anatectic processes at mantle depth. The focus of the study is concentrated on characterization of NGs and MPIs as they are primary agents of information about in situ anatexis in subduction zone. The new developments in inclusions studies allow for retrieval of primary melt compositions from NGs through re-homogenization experiments and their subsequent analysis with use of state-of-art techniques. This work includes collecting representative samples in the Central Jämtland, Sweden, performing classical petrological studies on the paragneisses, conducting re-homogenization experiments, and application of cutting-edge instruments in order to decipher information saved within inclusions.

Chapter II

Geological background

2.1 The Caledonian Orogen

The Caledonian Orogen comprises Scandinavian Mountains, British Isles, Svalbard Archipelago, east Greenland, and Appalachian Mountains in North America. The Caledonian orogeny was initiated by contraction of Iapetus Ocean and ocean-continent subduction in early Ordovician period. Complete closing of the ocean took 50 million years and led to collision between two palaeocontinents Baltica and Laurentia in Late Ordovician to Early Devonian. During the closure of Iapetus Ocean arc-continent collision occurred in Late Ordovician times and main continent-continent collision leading to deep subduction of Baltica margins occurred in Early Devonian period. At its peak Caledonides were comparable with Himalayan Orogens separating low-laying cratons of eastern Europe and Greenland (Gee et al. 2010, 2013). The Caledonian Orogen was divided in half when supercontinent Pangea break up driven by spreading of mid-Atlantic ridge. Due to this event Caledonides can be found on both sides of North Atlantic Ocean. Period prior the collision of two continents comprises events of sedimentation, magmatism, deformation, and metamorphism. Final event shaping present Caledonides was emplacement of allochthonous westward across the Laurentian margin and eastwards on the Baltica.

2.2 The Scandinavian Caledonides

The Scandinavian Caledonides was formed at the peak of collision between Baltica and Laurentia during the Early Devonian. Baltoscandian margin of Baltica was subducted beneath Laurentia creating series of nappes and thrusts transported onwards Baltica for more than 100 km. Exposed orogen stretches for almost 1800 km in Norway and western Sweden with width of 300 km in central and southern parts. Due to its age and occurred erosion give a great insight into internal structure of Himalaya-type orogen. In Scandinavian Caledonides four major tectonic units have

been recognized (Fig. 2.1) (Gee et al., 2008). First of them is Autochthon, which is described as the Fennoscandian Shield, consisting mostly of igneous rocks. It is a bedrock on which allochthon units were thrusted. Second is Lower Allochthon which consist mostly of sedimentary rocks as part of foreland basin with rare parts derived from crystalline basement of the Baltoscandian platform. The third one is Middle Allochthon which comprise the Baltoscandian rifted margin and continent-ocean transition zone. The Middle Allochthon is divided into lower and upper part representing outer margin of Baltica and outermost margin of Baltica, respectively. The upper part of Middle Allochthon is described as Seve Nappe Complex, which comprises various metamorphic rocks. The last distinguished unit is the Upper Allochthon, consisting of the Köli Nappe Complex which is ascribed part of former tectonic plate of Iapetus Ocean. The Upper-most Allochthon id composed of rocks with Laurentian margin affinities.

The Seve Nappe Complex (SNC) is an important element for understanding the evolution of Scandinavian Caledonides, and a key locality for understanding Wilson cycle in Scandinavian Caledonides (rifting-subduction-collision). SNC can be traced almost along all the Caledonides in Scandinavia (Fig. 2.3). Strongly deformed high grade metamorphic rocks (from amphibolite to eclogite facies) distinguish them from undelaying Särve nappes (greenschist facies). The age of metamorphism varies from c. 420 to 455 Ma, with exception of recently reported much older ages - 480 Ma (Walczak et al., 2022; Barnes et al., 2022) in the different parts of the Seve with the oldest units occurring more north-east. This study is focused on part of SNC localised in west central Jämtland outcropping as Åre synform (Lower and Middle Seve nappes). These napes have been thrusted over metasedimentary rocks of Särve Nappe as shown in geological profile of Fig. 2.3.

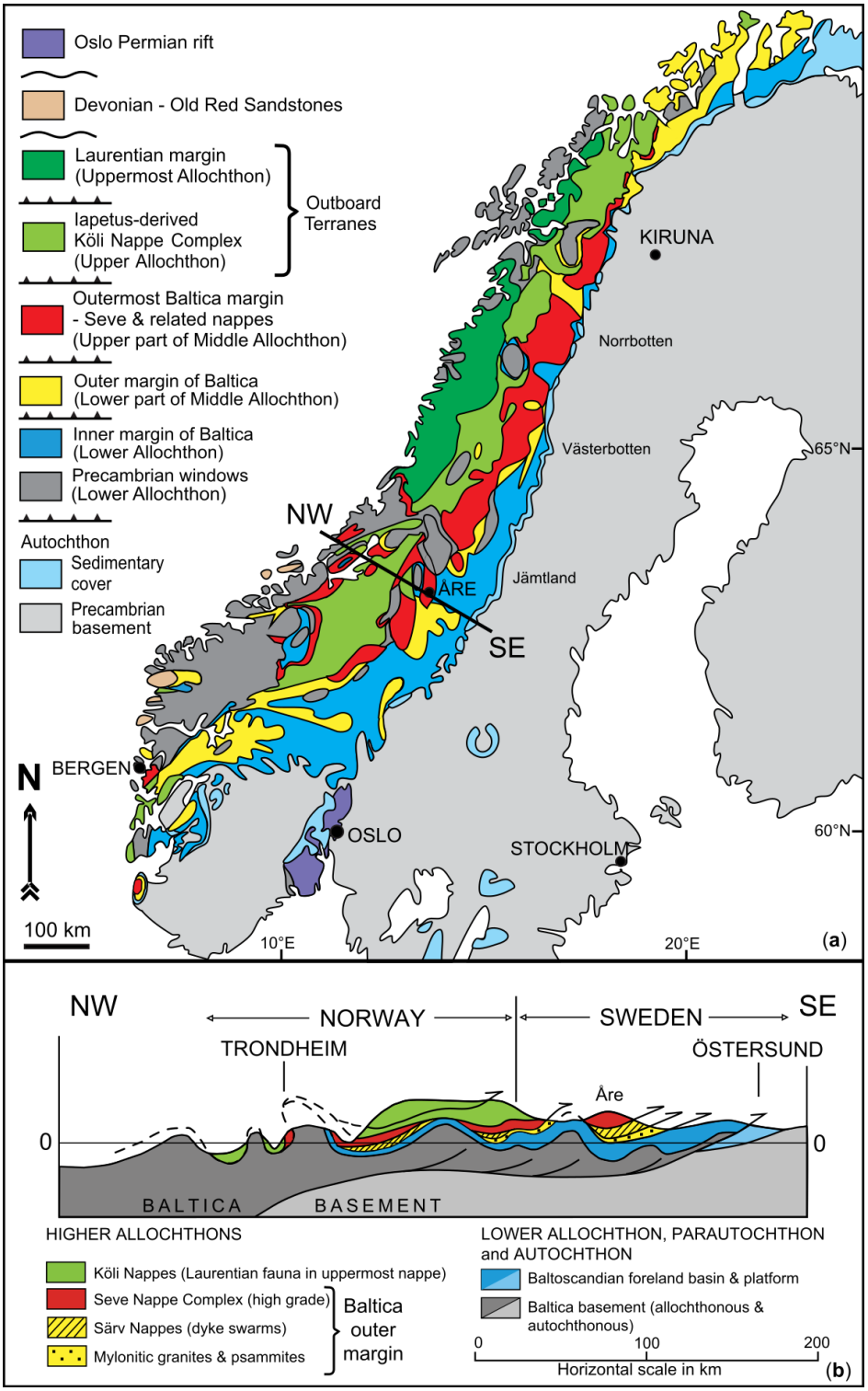

Figure 2.3 Tectonostratigraphic map of the Scandinavian Caledonides, with inferred provenance of the major tectonic units, and schematic profile across central-west Jämtland in the Scandinavian Caledonides after Gee et al. (2013).

2.3 Åreskutan Nappes

The Åreskutan (Middle Seve) Nappe outcrop on the upper levels of Åreskutan Mountain. The Åreskutan Nappe is approximately 500 m thick and it is composed of paragneisses, migmatites, leucogranites and metabasites (Ladenberger et al., 2014) The Majority of the rocks are garnet-, sillimanite-bearing paragneisses, rarely kyanite-bearing gneisses. The study of Klonowska 2014, 2017 documented presence of micro-diamonds included in the garnet within kyanite-bearing paragneisses. The paragneisses often show features of migmatiaztion as well separated leucosome and paleosome layers. Lithologies forming Åreskutan Nappe are cut by late discordant pegmatites that are strongly deformed in the basal thrust defining the border between Middle Seve and the underlying Lover Seve lithologies (Fig. 2.4). The focused area for this study is located on the east slops of Åreskutan Mountain as marked PS20-A1 and PS20-A2 on the Fig. 2.4.

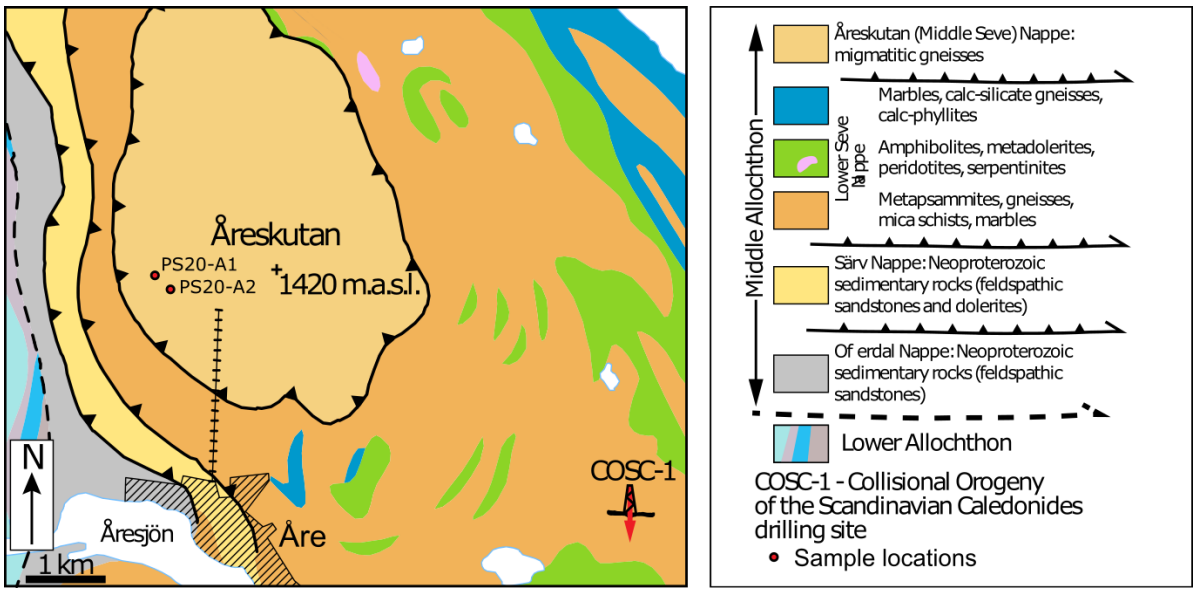

Figure 2.4 Geological map of the Åre aera with sample locations, PS20-A1 and PS20-A2 sampled in exact location of IK16-11 and IK18-11, respectively. Geological map and position of IK16-11, IK18-11 sampling area are taken from Klonowska et al. 2017.

Chapter III

Analytical methods

Sample preparation. Approximately 50 samples were prepared from the paragneisses of Åreskutan at the Department of Geosciences (DG), University of Padua (UniPD), Italy. The type of preparation depends on analytical goals: 1) standard thin-section (around 30 µm thickness) for petrographic description, 2) thick (50 – 100 µm) double polished section for inclusion investigation, 3) thin and thick-section polished with carbon-free medium and cleaned in ultrasonic bath for documenting presence of diamond, 4) 1 mm thick polished section for garnet extraction, 5) epoxy resin mount with metallographic polishing for the microstructural characterization of nanogranitoids.

Optical microscopy was extensively used for petrographic analysis in both transmitted and reflected light using several microscopes at the DG, UniPD, Italy. Two thin sections were analysed by the ZEISS AxioScan 7 Geo system. The system acquires high-resolution digital images of the entire thin sections, under plane-polarized light (PPL) and crossed polarizers (XPL). Both light modes PPL and XPL are collected as a set of 6 channels that enable variations to be observed as the polariser set is rotated relative to the sample. Data collected in this way might be displayed and processed with ZEISS Zen software recreating the digital petrographic microscope. The thin section scanning was conducted at the ZEISS Customer Centre in Jena, Germany.

Scanning electron microscopy (SEM) was applied for Back-scattered Electrons (BSE) and Secondary Electrons (SE) imaging, and semi-quantitative chemical analysis by Energy Dispersive X-Ray Spectroscopy (EDS). Analytical work was performed using five SEM instruments including high-resolution Field Emission Gun (FEG) electron microscopes:

1) Camscan MX3000 equipped with W filament, and LaB_6 cathode and semi-quantitative detector EDAX EDS, at the DG, UniPD, Italy.

2) FEI Quanta 200 with variable-pressure chamber (ESEM) equipped with W filament and energy dispersive X-ray detector EDAX (EDS) Element- C2B at the Centro di Analisi e Servizi Per la Certificazione (CEASC), UniPD, Italy.

3) Dual-beam FIB-FE-SEM Tescan SOLARIS, with a variable-pressure chamber, equipped with Oxford Instruments microanalytical system, at the DG, UniPD, Italy.

4) FEG-SEM equipped with EDS detector at the Department of Physics, UniPD, Italy.

5) ZEISS Sigma 300VP FEG-SEM equipped with the Zeiss Mineralogic 2D software for the automated quantitative petrology. The full section scans were performed at the ZEISS Customer Centre in Cambridge, United Kingdom. Analytical conditions for BSE, SE imaging and EDS analysis varied as a function of instruments and of observed object, usually 10-15 kV accelerating voltage and variable magnification up to 15000x for inclusion imaging.

Electron Microprobe (EMP). Composition of minerals, chemical profiles and elemental maps were acquired with the Jeol JXA 8200 Superprobe, equipped with 5 wavelength dispersive spectrometers (WDS) at the Dipartimento di Scienze della Terra (DST), Università di Milano (UniMi), Italy. Measurements were performed 20 kV accelerating voltage, 120 nA beam current and 5 µm spot size for mineral analysis. Natural, synthetic silicates and oxides were used as standards. The same EMP was used to measure major element composition of glass and minerals in re-melted nanogranitoids. Analytical parameters were: 15 kV accelerating voltage, 2 nA beam current and 1 µm beam spot size diameter, counting time of 10 s on peak and 2 s on background. Sodium and potassium were analysed as first due to their migration from the electron beam excitation volume. This effect may cause underestimation of those elements in re-homogenised inclusions. Therefore, the procedure suggested by (Morgan and London, 1996, 2005) and successfully used by (Ferrero et al., 2012;

Bartoli et al., 2013b, 2013a), was applied. Secondary standards with known composition were used to calculate correction factors for Na, K, Si and Al. Three leucogranitic glasses with major chemical composition as similar as possible to analysed samples were chosen. The glass standards are: LGB-5 with 10.11 wt% H_2O (Behrens and Jantos, 2001), DL with 5.53 wt% H_2O (Acosta-Vigil et al., 2003), and almost anhydrous 0.03 wt% H_2O SAND (Acosta-Vigil et al., 2003). Measurement of the glass was carried out just after analysis of the secondary standards during the same analytical session, using the same working conditions.

Micro-Raman spectroscopy was used for non-destructive recognition of phases inside the multiphase inclusions and nanogranitoids. This technique was also applied to localise and analyse microdiamonds occurring in the rock. Two instruments were used: 1) a Thermo-Scientific DXR Raman Microscope at the Dipartimento di Scienze Chimiche, UniPD, Italy, 2) a WITec alpha300 R Raman Imaging Microscope at the DG, UniPD, Italy. Green laser (532 nm) was used as an excitation source. Spectra were collected in the range 100 – 4000 cm^{-1}. Conditions for the analysis were as follows: emission power 2-5 mW, 100x objective lens, pinhole aperture 50 µm. Each spectrum was collected in two accumulations of 3-30 s in order to avoid cosmic radiation.

Micro computed tomography (µ-CT). Three-dimensional investigation of the spatial relationship between MPI, NG, diamonds and other mineral inclusions was performed by µ-CT using the ZEISS Xradia 510 Versa X-Ray microscope (XRM). Analytical work was conducted at Karlsruher Institut für Technologie, Oberkochen, Germany.

X-ray Fluorescence (XRF). Bulk rock compositions were obtained by XRF on pressed powder pellets using a PANalytical Axios wavelength dispersive XRF spectrometer at the Biological, Geological and Environmental Department, University of Bologna, Italy.

Re-homogenization experiments. To obtain the chemical composition of the melt generated during the partial melting of investigated rocks, nanogranitoids were

experimentally remelted using a Walker type multi-anvil module on a 1000-ton uniaxial press at the Laboratorio di Petrologia Sperimentale, DST, UniMi, Italy following the procedure tested by Bartoli et al. (2013a)

Several 1 mm thick sections were prepared in order to localise the most promising garnets, in terms of nanogranitoid occurrence and preservation, and extract them by core-drilling at the DG, UniPD, Italy. This procedure resulted with 2.7 mm-wide garnet disks with a thickness of 1 mm (Fig 3.1a). Two garnet discs were charged into Au capsules (external diameter of 3 mm) and filled with powdered graphite and quartz (proportion of the mixture 1:1 wt%). The Au capsule was crimped (Fig. 3.1b) and sealed with a micro arc-welder, then surrounded with MgO spacers and put in a graphite sleeve which works as a heater. Subsequently a combined setup was inserted into the ceramic octahedron. The temperature was controlled with a S-type ($Pt_{90\%}$ – $Rh_{10\%}$ / $Pt_{100\%}$) thermocouple with an estimated accuracy of ± 1.5˚C. The thermocouple was inserted into a pre-prepared hole as close as possible to the capsule. All parts of the assembly are shown in Fig. 3.1c. The assembled octahedron (Fig. 3.1d) was positioned between eight W (tungsten) anvils and set in the hydraulic press (Fig. 3.1e and f). Experiments were started from gradual pressurization to the target pressure value. Then the isobaric heating was initiated at a constant rate of 50˚C/min. When the target temperature was reached, the experiment was let run for the planned time (24 or 48h), then quenched by turning off the heating and letting still active cooling system to lower the temperature. Finally, gradually depressurized to the ambient conditions. After each experiment, the capsule was recovered from the press, embedded in the epoxy resin, and opened by grinding the surface on abrasive papers. All analyses were corrected according to DL standard that contain 5.52 wt% of H_2O. Sodium and potassium loss during the EMP analysis was estimated as 44 - 49% and 9 - 23%, respectively.

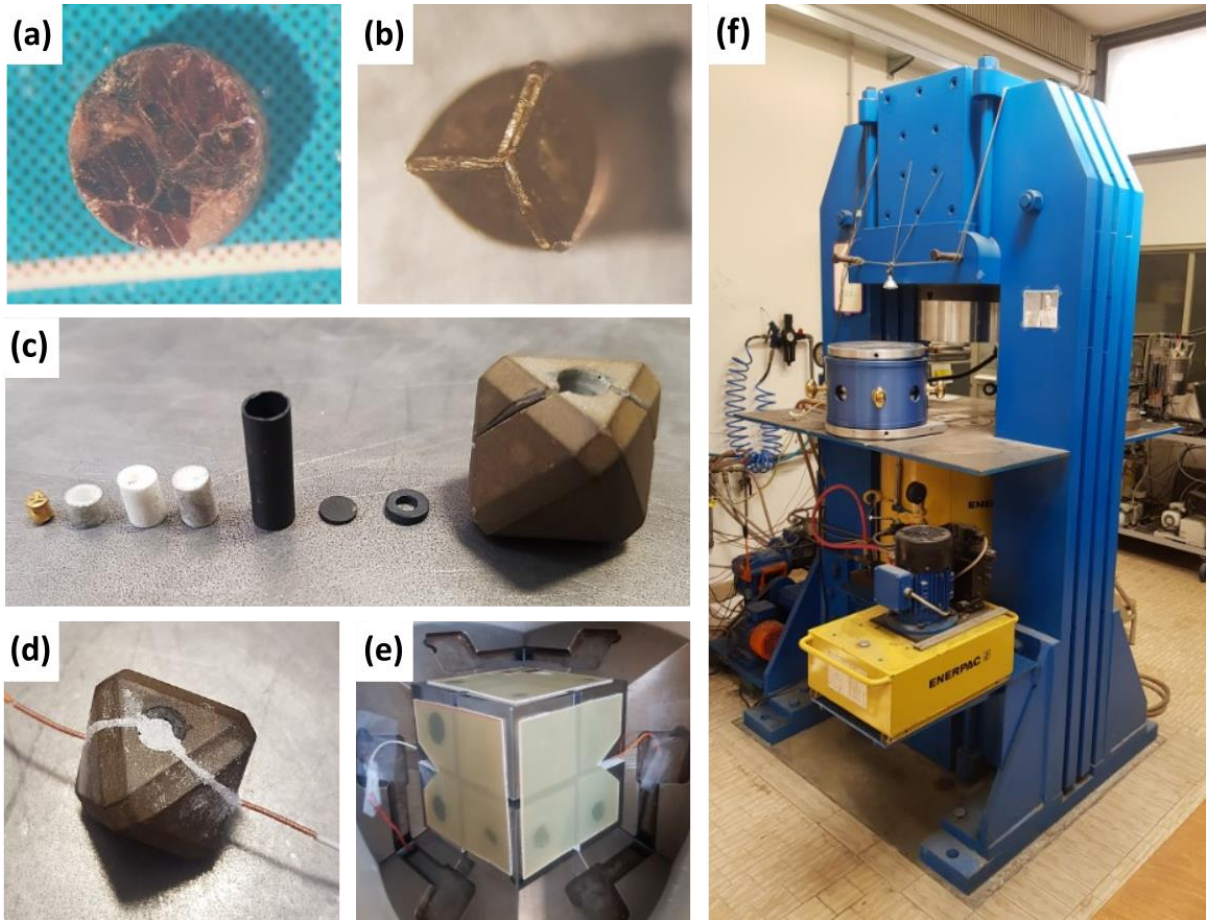

Figure 3.1 Photographs showing preparation of multi-anvil experiment, **(a) –** garnet disc extracted from the 1 mm thick section (Ø 2.7 mm), **(b) –** loaded and crimped golden capsule (Ø 3.1 mm x 4 mm), ready to be sealed, **(c) –** parts ready to be assembled, from left: golden capsule with the sample, three pieces of MgO salt spacers, graphite heater sleeve with bottom cup and upper ring, ceramic octahedron. **(d)** – cemented octahedron, **(e)** – octahedron aligned between W anvils and mounted in the hydraulic press **(f)**.

Nano Secondary Ion Mass Spectrometry (NanoSIMS) was used to determine content of volatiles (H_2O and CO_2) in the remelted nanogranitoids. Analysis was conducted with the Cameca NanoSIMS 50 at Muséum National d'Histoire Naturelle of Paris, France, following the approach described by Bartoli et al. (2014). Polished experimental capsules with re-homogenized nanogranitoids on the surface of the garnet were mounted in In (indium) as shown by Aubaud et al. (2007). Due to the Au-coating of the surface remelted nanogranitoids could be recognized only by collecting secondary images of Si, K, and Fe. For every identified melt inclusion pre-sputtering was performed, to remove coating and clean the surface for the analysis. Conditions for the pre-sputtering were as follows: surface area up to 20 x 20 µm (depending on

inclusion size) for 2 min with 400 pA primary Cs^+ beam. To exclude possibility of carbon contamination secondary images of C and H were collected and all remnants of former carbon coating located inside the micro-fractures of melt inclusions and hosting garnet were removed by repeating the pre-sputtering process until all visible imperfections were removed and only homogenous glass remained. Then a primary beam of 37 pA was used for data acquisition in a raster of 3 x 3 μm^2 surface area but collecting signal only from the centre part 1 x 1 μm^2 (beam blanking mode) to minimize surface contamination. Every analysis is composed of 200 cycles, a cycle last 1.024 s long. Ions as $^{16}OH^-$, $^{28}Si^-$, ^{27}Al, $^{56}Fe^{16}O^-$, $^{12}C^-$ were collected simultaneously in multicollection mode. H_2O and CO_2 contents were estimated measuring ratios $^{16}OH^-/^{28}Si^-$ for water and $^{12}C^-/^{28}Si$ for carbon dioxide (Bartoli et al., 2014; Créon et al., 2018)**.** Then the measured ratios were recalculated with calibration curves. Data for calibration were obtained from analysis of standards with known content of H_2O and CO_2. The leucocratic glass standards were used for calibration of H_2O content: 1) hydrous glass DL with 5.53 wt% H_2O (Acosta-Vigil et al., 2003), 2) anhydrous glass B 0.03 wt% H_2O (Acosta-Vigil et al., 2003), 3) LGB-1 4.86wt% H_2O (Behrens and Jantos, 2001). The standards for calibrating CO_2 content are trachyandesites from the Stromboli Volcano experimentally doped in carbon and water by (Bureau et al., 2003)**.** All standards contain from 556 to 864 ppm of CO_2 (STR9, STR10, STR11, STR13), with the exception for B which was used as carbonless glass.

Au-coated capsules were mounted in indium (Fig. 3.2a) and pre-sputtering procedure was conducted to remove the coating and prepare surface of inclusions for the analysis (Fig. 3.2b). The few larger inclusions (>10 µm) were analysed by NanoSIMS and EMP to acquire major element composition and volatile content for cross-comparison (Fig. 3.2c). Procedure is described in detail in methods chapter. Before each analytical session secondary standards were measured to calculate calibration line.

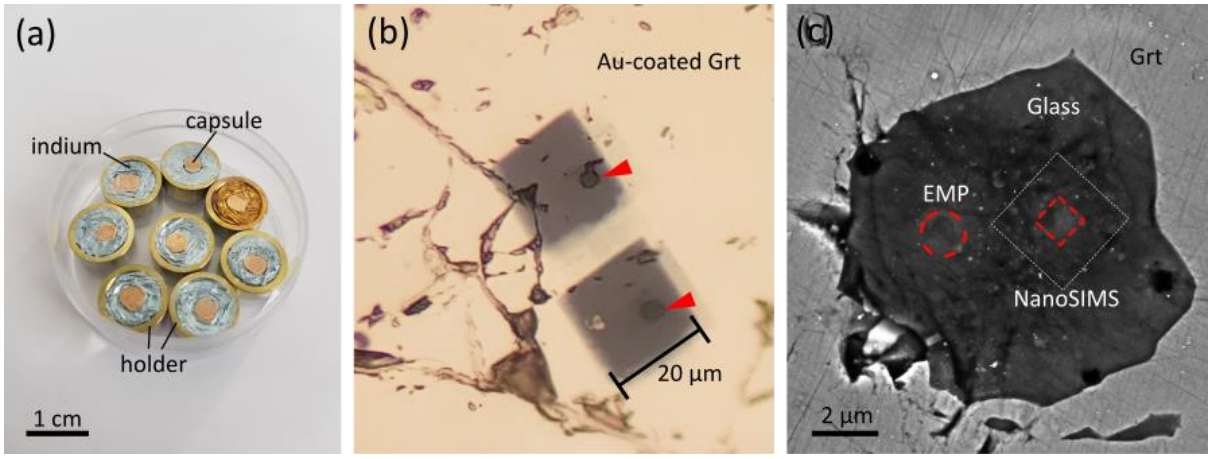

Figure 3.2 (a) – capsules mounted in indium mounts for NanoSIMS analysis, **(b)** –photomicrograph in reflected light showing Au-coated garnet with pre-sputted areas (20 x 20 µm), red arrow indicates position of inclusions **(c)** – BSE image of remelted nanogranitoid after NanoSIMS analysis, surface polishing, and EMP analysis. Dashed red line indicates the EMP pit (1 Øµm) and NanoSIMS acquisition area in blank mode (1 x 1 µm), whereas the white dashed line shows area of preliminary acquisition raster (3 x 3 µm).

Chapter IV

Petrography of the paragneiss

4.1 Macroscopic description

The studied rocks are paragneisses, that underwent various degrees of deformation, high-grade metamorphic conditions and partial melting. Despite of strongly weathered surfaces visible in the field, the gneissic foliation can still be seen in the outcrops (Fig. 4.1a). On the fresh unweathered surface these rocks are fine- to medium-grained, with well-developed foliation underlined by dark- and light-coloured bands. Discontinuous dark and white bands might be assigned to melanosome and leucosome, respectively (Fig. 4.1b). Macroscopically visible garnet porphyroblasts (< 5 mm) are predominating the melanocratic domains, but they are also common and spread randomly in the leucocratic white bands.

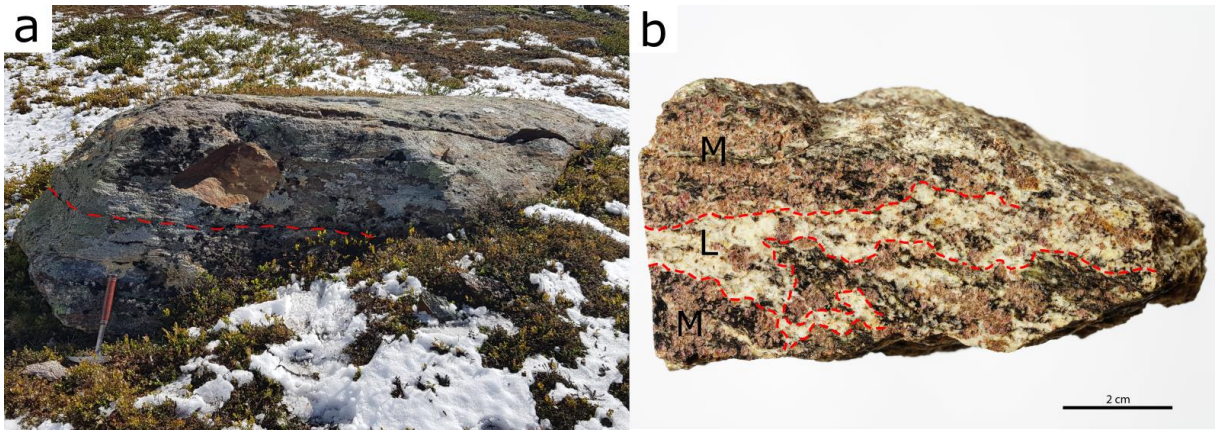

Figure 4.1 (a) - photographs of outcrop A1, dashed red line indicates the foliation. **(b)** - photograph of the paragneiss hand-specimen PS20-A1. M – melanosome, L – leucosome.

Under the microscope, the thin sections revealed a well-developed foliation, underlined by the alignment of quartz, biotite crystals and sillimanite needles. Garnet porphyroblasts are present, sometimes they consist of aggregates of smaller garnet blasts. The mineral assemblage of paragneiss is K-feldspar, garnet, biotite, plagioclase, quartz, muscovite, kyanite, sillimanite and rutile (Fig. 4.2a). Based on the mineral classification image of section PS20-A1B-02 (Fig. 4.2a), modal abundances of minerals

were calculated as: K-feldspar = 31%, quartz = 20%, garnet = 17%, biotite = 15%, aluminosilicates = 9%, plagioclase = 7%, muscovite = 1%, rutile = <1%. Leucocratic bands are dominated by coarse-grained K-feldspar, quartz, and plagioclase (Fig. 4.2b) which represent crystallized segregated melt. Whereas melanocratic domains ascribed as solid fraction left after melt separation are composed mostly of garnet aggregates, biotite, and muscovite (Fig. 4.2c).

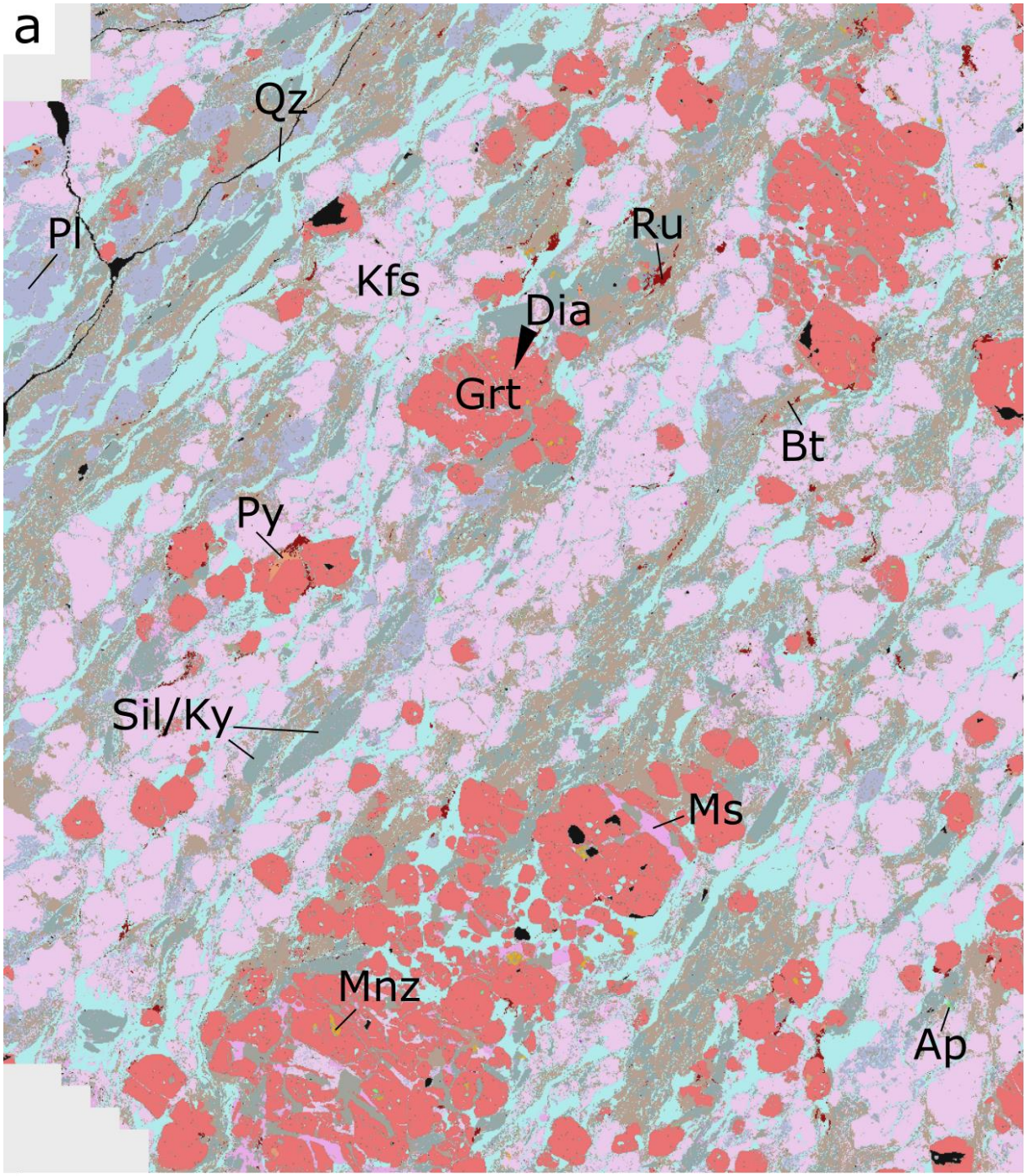

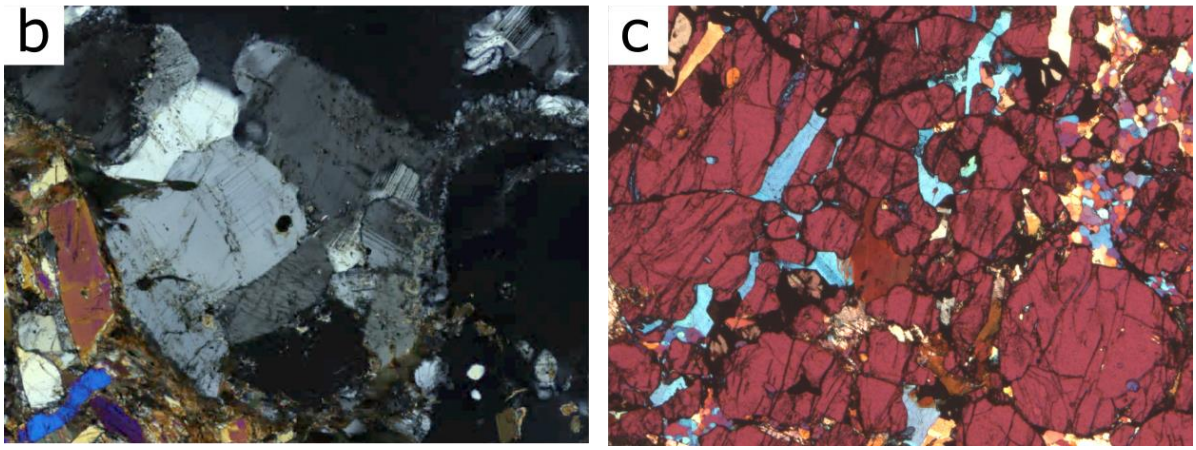

Figure 4.2 (a) – mineral assemblage classification image based on BSE scan of the entire section (PS20-A1B-02) with SEM and processed with Zeiss Mineralogic 2D software; chemical information from the EDS has been converted into mineral classifications that have been assigned a unique colour (abbreviations of minerals according to Whitney and Evans, 2010). **(b) –** photomicrograph in crossed polarized light (XPL) of a portion of leucosome (centre of the image), composed of K-feldspar, plagioclase, and quartz showing igneous texture. **(c) –** photomicrograph XPL with lambda filter of melanosome consisting of garnet aggregates (red), mica+plagioclase (blue), and quartz (yellow, orange, blue polygons).

4.2 Garnet

Garnet commonly occurs as a subhedral to anhedral single porphyroblast (< 5 mm) or aggregate of smaller (0,2 - 0,5 mm) crystals (Fig. 4.3a). Smaller garnets (around 200 µm in diameter) occurring at the edge of aggregates or as isolated crystals in the matrix often exhibit sub- to euhedral shape. Most of the garnets present fractures cutting through the whole porphyroblasts/aggregates, filled with biotite or muscovite. Garnet contains mineral inclusions of quartz, K-feldspar, plagioclase, biotite and muscovite, (< 50 µm), zircon, apatite, pyrite, ilmenite, graphite and microdiamond. Rutile inclusions are present as small (< 20 µm) rounded crystals in the garnet core and mantle (Fig. 5.6e) and larger elongated aggregates of crystals in the vicinity of the garnet rim, sometimes partially embedded in the matrix (Fig. 5.6d). In the core of the garnet, clusters of inclusions are present (Fig. 4.3b): the smaller (< 5 µm), are mostly MPI whereas the larger inclusions (< 20 µm), are NG (see Chapter VI). In few garnets, clusters of sillimanite needles are present, but they never overlap with clusters of MPI or NG inclusions and they are separated by inclusion free area (Fig. 5.1). Garnets containing sillimanite inclusions usually are sub- to euhedral, in contrary garnets

hosting NG and MPI are anhedral, rounded, sometimes showing embayment of the rim filled with quartz, feldspar or rutile (Fig. 4.3a and b). Two generations of garnet can be distinguished based on texture and presence of the inclusions: 1) Grt I, associated with NG, MPI, diamond and kyanite (Fig. 4.3a and b), 2) Grt II, associated with sillimanite and biotite (Fig. 4.3a and b).

4.3 K-feldspar

K-feldspar appears usually as coarse-grained lens-shaped crystals (< 2 mm) oriented parallel to the foliation. It often occurs subhedral in leucocratic domains (Fig. 4.2b). Some of the larger (> 1 mm) crystals are poikoblastic and contain rounded mineral inclusions (< 200 µm) of quartz, biotite and plagioclase which often occur with a sub- to euhedral shape. Some of the inclusions in K-feldspar are filled with products of alteration (chlorite, iron oxides). Some of medium-grained K-feldspar crystals occurring in the matrix are partially resorbed and substituted by biotite (Fig. 4.3c) or they have a fine-grained intergrowth of biotite and sillimanite in the rim. Four generations of K-feldspars can be distinguished based on the textural position: 1) medium-grained partially resorbed K-feldspar, 2) coarse-grained intact K-feldspar, 3) fine-grained K-feldspar occurring in the interstitial position, formerly occupied by melt filled pores, 4) K-feldspar inclusions in the garnet. The K-feldspar inclusions are usually rounded, sometimes they exhibit 'moat' texture. The size of the inclusions varies from 50 to 200 µm. K-feldspar occurring in the garnet in larger polyphase inclusion (> 50 µm) can be associated with muscovite, biotite, quartz and kyanite or sillimanite. Myrmekites are often present along the rims of K-feldspar blasts in the matrix.

4.4 Plagioclase

In leucosome plagioclase occurs as coarse-grained lens shaped crystals, or in aggregates of subhedral grains often associated with K-feldspar. Grain boundaries of plagioclase are often euhedral in contact with K-feldspar or quartz (Fig. 4.3d). Many grains of plagioclase are partially substituted by biotite. Plagioclase is also included in K-feldspar, as rounded to subhedral grains (< 200 um), or as smaller rounded inclusions

in garnet (< 50 um). In the melanocratic domains plagioclase occurs in interstitial position between garnet blasts and as a common filling of the larger cracks in the garnet alongside other minerals like muscovite, biotite, carbonates, and iron oxides.

4.5 Aluminosilicates

Kyanite is present in the matrix as elongated iso-oriented coarse-grained crystals sometimes fractured and bent according to the deformed foliation (Fig. 4.3e). Kyanite is often substituted by sillimanite to various degree, from partial to almost total substitution with remaining skeletal crystals (Fig. 4.3f). Inclusions of kyanite are present in the garnet, usually in vicinity or within clusters of NG and MPI in Grt I (Fig. 6.6a).

Four textural generations of sillimanite are present: 1) anastomosing folia of fibrolite in the matrix, 2) coarse prismatic crystals sometimes associated with kyanite in the matrix (Fig. 4.3e), 3) fine-grained idiomorphic crystals included in quartz, 4) clusters of sillimanite needles included in the garnet ascribed as Grt II (Fig. 4.4d).

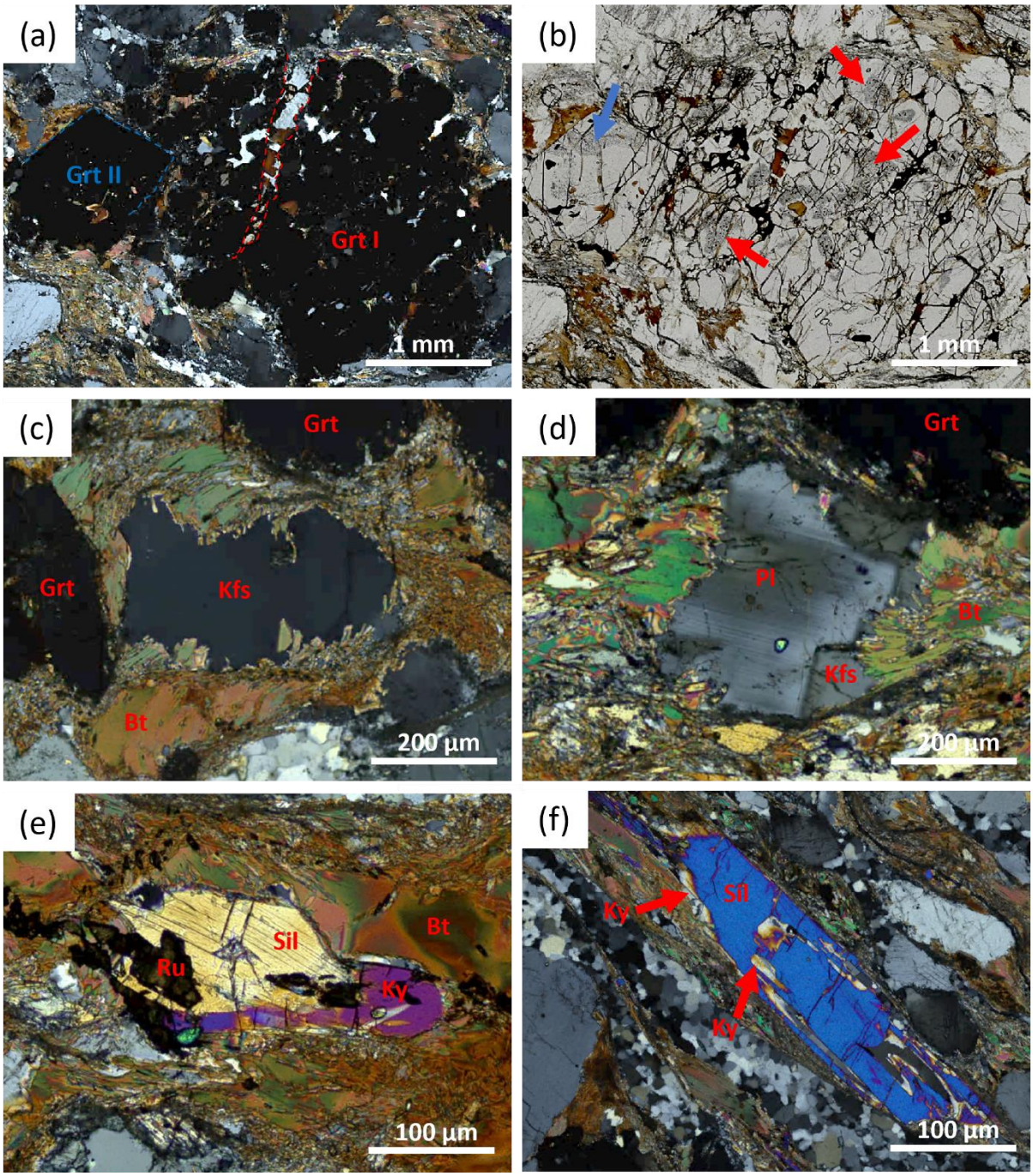

Figure 4.3 Photomicrographs of representative minerals occurring in the matrix of the paragneiss, **(a)** – photomicrograph in XPL of garnet porphyroblast/aggregate defining two generations; red dashed line indicates fractured filled with plagioclase, biotite, carbonates and iron-oxides; blue dashed line indicates euhedral boundaries of garnet II, **(b)** – photomicrograph in plane polarized light (PPL) of garnet porphyroblast/aggregate; red arrows indicate clusters of nanogranitoids and MPI while the blue arrow points cluster of sillimanite needles, **(c)** – photomicrograph in XPL of K-feldspar blast partially resorbed and substituted by biotite, **(d)** – photomicrograph in XPL of plagioclase crystal associated with K-feldspar. Plagioclase exhibits euhedral walls. K-feldspar and plagioclase are partially resorbed and substituted by biotite, **(e)** – photomicrograph in XPL of sillimanite associated with kyanite, **(f)** – photomicrograph of skeletal kyanite almost fully replaced by sillimanite.

4.6 Quartz

Quartz occurs mostly in leucocratic domains as ribbons consisting of dynamically recrystallized crystals. Quartz can be found often in pressure shadows next to the garnet, crystallized as polygonal quartz. The ribbons define the foliation in the rock. Fine-grained quartz crystals occur in interstitial position filling the space after former films of melt. In the garnet and K-feldspar inclusions of quartz are commonly present. Rounded quartz inclusions occurring in the garnet are sometimes surrounded by radial cracks (Fig. 4.4e). Intergrowths of quartz and feldspar are present as myrmekites.

4.7 Micas

Biotite occurs in the rock in three textural positions; in the matrix as large (1 mm) subhedral crystals oriented and bent following foliation of the rock, or medium grained crystals randomly oriented, often forming aggregates (Bt in Mtx) (Fig. 4.4a). Biotite occurs also as inclusions in the garnet (Bt in Grt) and K-feldspar or as fine-grained crystals filling cracks in the garnet (Bt in cracks). Biotite present in the matrix is particularly common in the melanocratic portion of the rock.

Muscovite rarely occurs in the leucosome. When it occurs in the matrix, it can be found as fine-grained crystals associated with biotite, localized usually in the centre of biotite aggregate. In melanosome muscovite is medium-grained and it occurs in interstitial position between garnet blasts, or as filling of the fractures in the garnet (Fig. 4.4b). In the matrix crystals of muscovite are usually less than 200 µm in size. Muscovite is also present as inclusions in the garnet.

4.8 Rutile

Rutile is present in the matrix as coarse rounded crystals and as fine-grained interstitial crystals close to garnet (Fig. 4.4c and d). Sometimes rutile adjacent to the garnet is partially included in the garnet rim. Rounded rutile grains (20 µm) can occur also as inclusions in the garnet core and in the mantle. Oriented rutile needles occur in the garnet core in vicinity of NG and MPI clusters. Rutile is also observed associated with the ilmenite.

Considering the different textural positions, five textural generations of rutile can be distinguished; 1) Rutile in matrix – grains occurring in the matrix, often as rounded single crystals, 2) Rutile in corona of garnet – grains occurring as fine grain aggregates of crystals in interstitial position often adjacent to the garnet, sometimes filling cracks in the garnet. 3) Rutile in garnet core – grains occurring in the core of the garnet, often in close vicinity of NG and MPI clusters, sometimes as an accessory part of NG assemblage, 4) Rutile in garnet mantle – grains occurring in inner part of the garnet, 5) Rutile in garnet rim– grain occurring in the rim of the garnet but entirely enclosed by it.

4.9 Other phases

Accessory minerals like zircon, monazite, apatite, ilmenite, and pyrite are present in the matrix and included in the garnet porphyroblasts. Graphite is present rarely in the matrix as flakes, but it can also occur as inclusion in the garnet. Another important accessory mineral included in the garnet is microdiamond. Sometimes, carbonates may be observed associated with iron oxides, usually occurring in fractures of rigid minerals.

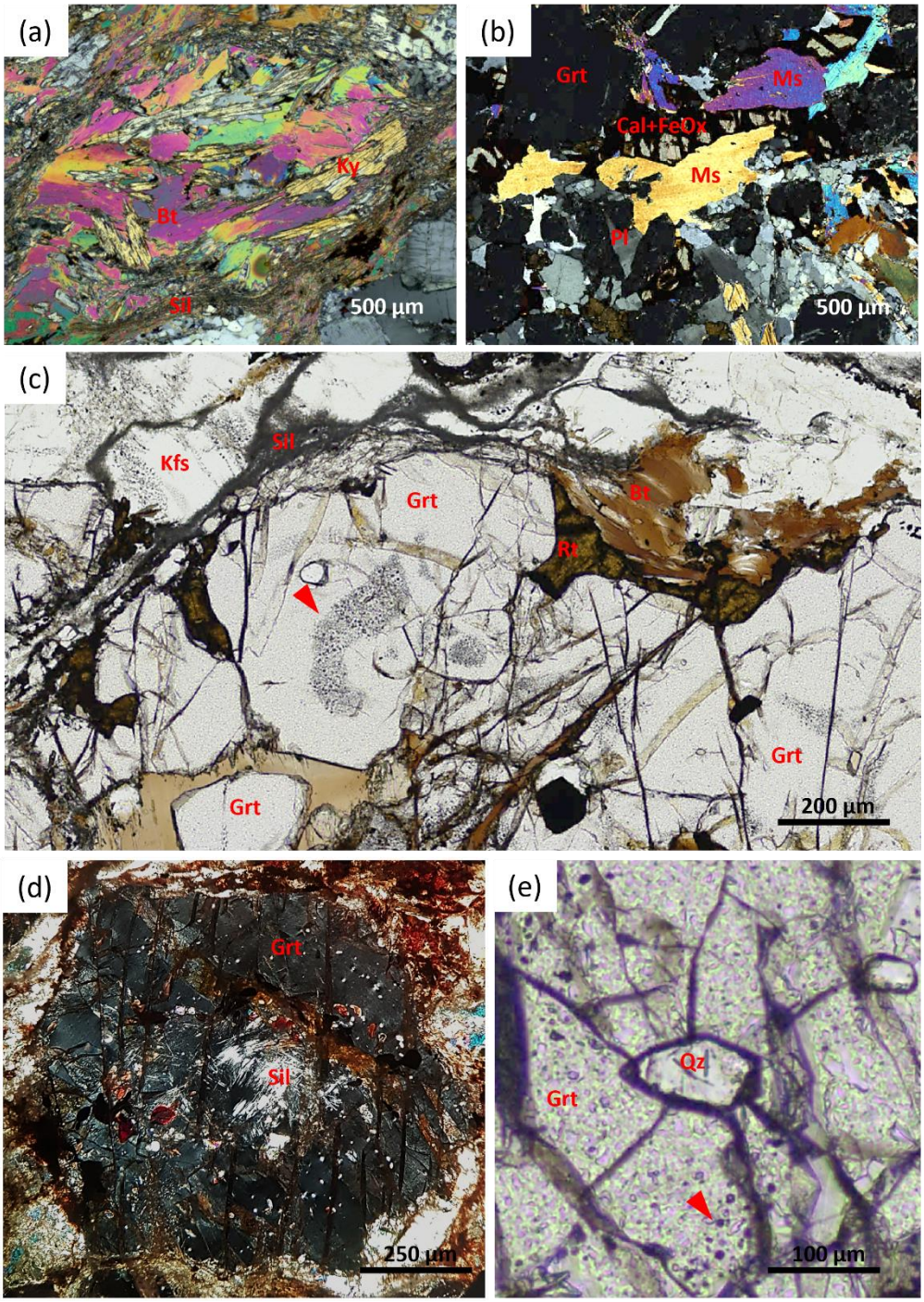

Figure 4.4 Photomicrographs of minerals from the paragneiss, **(a) –** photomicrograph in XPL of a lens-shaped aggregate of biotite associated with skeletal kyanite, **(b) –** photomicrograph in XPL of muscovite in melanosome, sillimanite, **(c) –** photomicrograph in PPL of interstitial rutile associated with garnet, red arrow indicate cluster of NGs, MPIs, Dia, **(d) –** photomicrograph in XPL of garnet II with sillimanite needles, **(e) –** photomicrograph in PPL of quartz inclusion in garnet surrounded by radial cracks.

4.10 Melt pseudomorphs

Diagnostic features that have been attributed to the former presence of melt were described in detail by Vernon (2004). Textures which are recognized in the paragneisses from Åreskutan are: 1) the string of beads texture (Holness and Isherwood, 2003), composed of small beads of quartz representing former melt, located along grain boundaries of garnet and K-feldspar (Fig. 4.5a and b); 2) cuspate crystals with low dihedral angles (Holness and Sawyer, 2008), in this case composed of K-feldspars and quartz that crystalized in formerly melt filled pores (Fig. 4.5c and d); 3) pseudomorphs after melt filled films along grain boundaries of different phases, e.g. K-feldspar crystals between plagioclase and sillimanite grains (Sawyer, 2001); 4) Presence of straight subgrain boundaries of K-feldspar and plagioclase that are ascribed as crystalized in the presence of melt (Fig. 4.5e and 4.3d). 5) The 'moat' texture in K-feldspar inclusion in the garnet, that represent former film of melt (Fig. 4.5f). Many of the pseudomorphs after the melt films are obscured by formed later sillimanite needles.

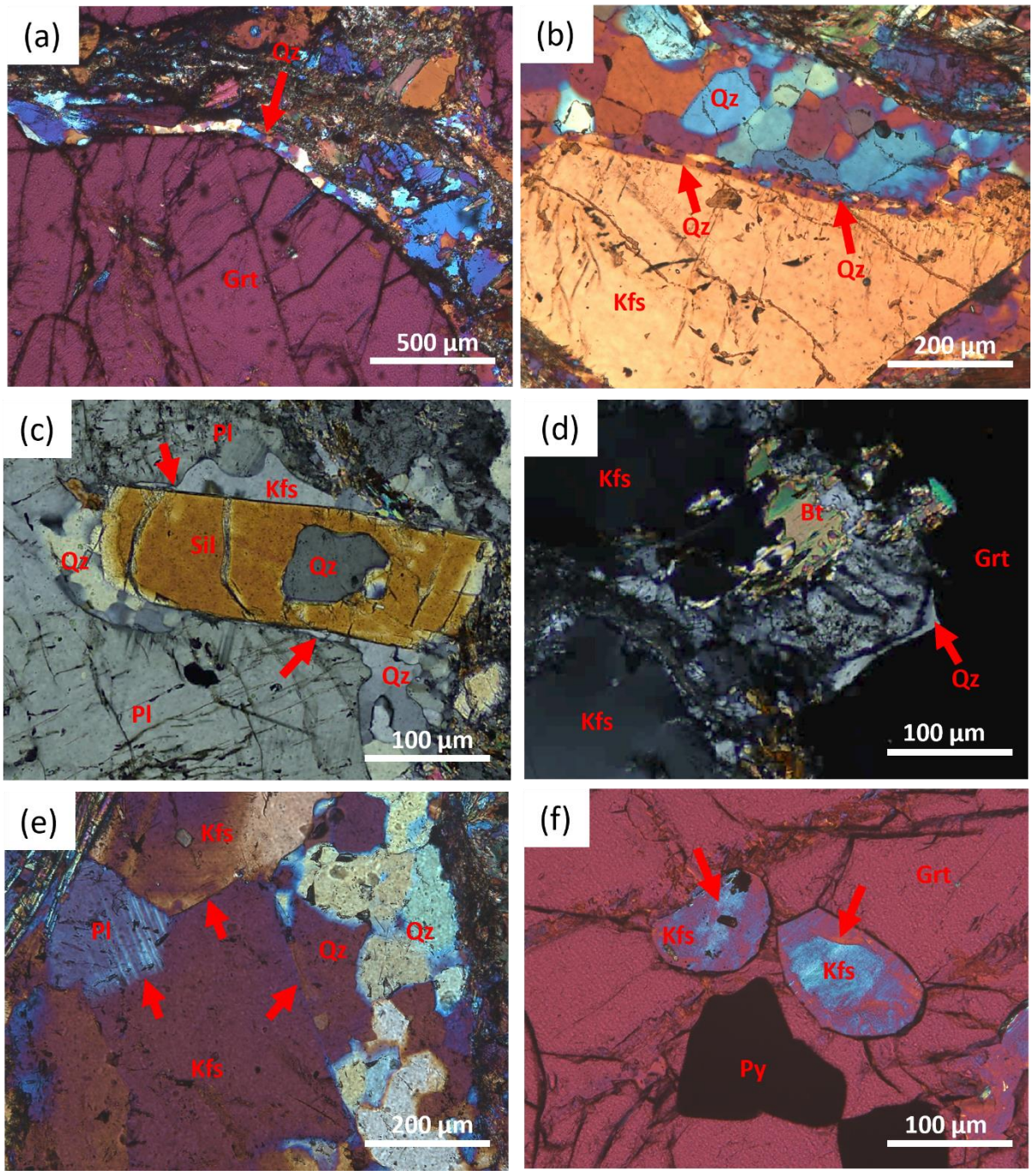

Figure 4.5 Photomicrographs of textures indicating former presence of melt in the paragneiss, **(a) –** photomicrograph in XPL with lambda plate showing 'string of beads' texture composed of quartz grains surrounding garnet porphyroblast, **(b) –** photomicrograph in XPL with lambda plate of 'string of beads' texture composed of quartz along K-feldspar boundary **(c) –** photomicrograph in XPL showing quartz and K-feldspar cuspate crystals (red arrows) interpreted as melt pseudomorphs, **(d) –** photomicrograph in XPL showing quartz cuspate crystal (red arrow) interpreted as melt pseudomorph, **(e) –** photomicrograph in XPL with lambda plate showing euhedral boundaries of K-feldspar and plagioclase (red arrows) interpreted as crystalized in the presence of melt, **(f) –** photomicrograph in XPL of K-feldspar inclusion in garnet exhibiting 'moat' texture formed in the position of formerly present melt.

4.11 Deformation

The paragneiss from Åreskutan is strongly deformed. The microstructures suggesting strong brittle and ductile deformation can be observed: 1) pressure shadows around garnet porphyroblast consisting of biotite (Fig. 4.6a), sometimes with well pronounced kinematic indicators such as two sided σ-type mantled porphyroblast (Fig. 4.6b), 2) bent sillimanite crystals that follow the foliation of the rock (Fig. 4.6c), 3) boudinage of prismatic sillimanite crystals resulted from pure shearing (Fig. 4.6d), 4) fractured garnet porphyroblasts (Fig. 4.6e), 5) simple sheared offset K-feldspar crystals (Fig. 4.6f), and 6) dynamically recrystallized quartz occurring as ribbons. These observations confirm the presence of ductile and brittle deformation. Deformation related features are not further investigated, as they are beyond the focus of this work.

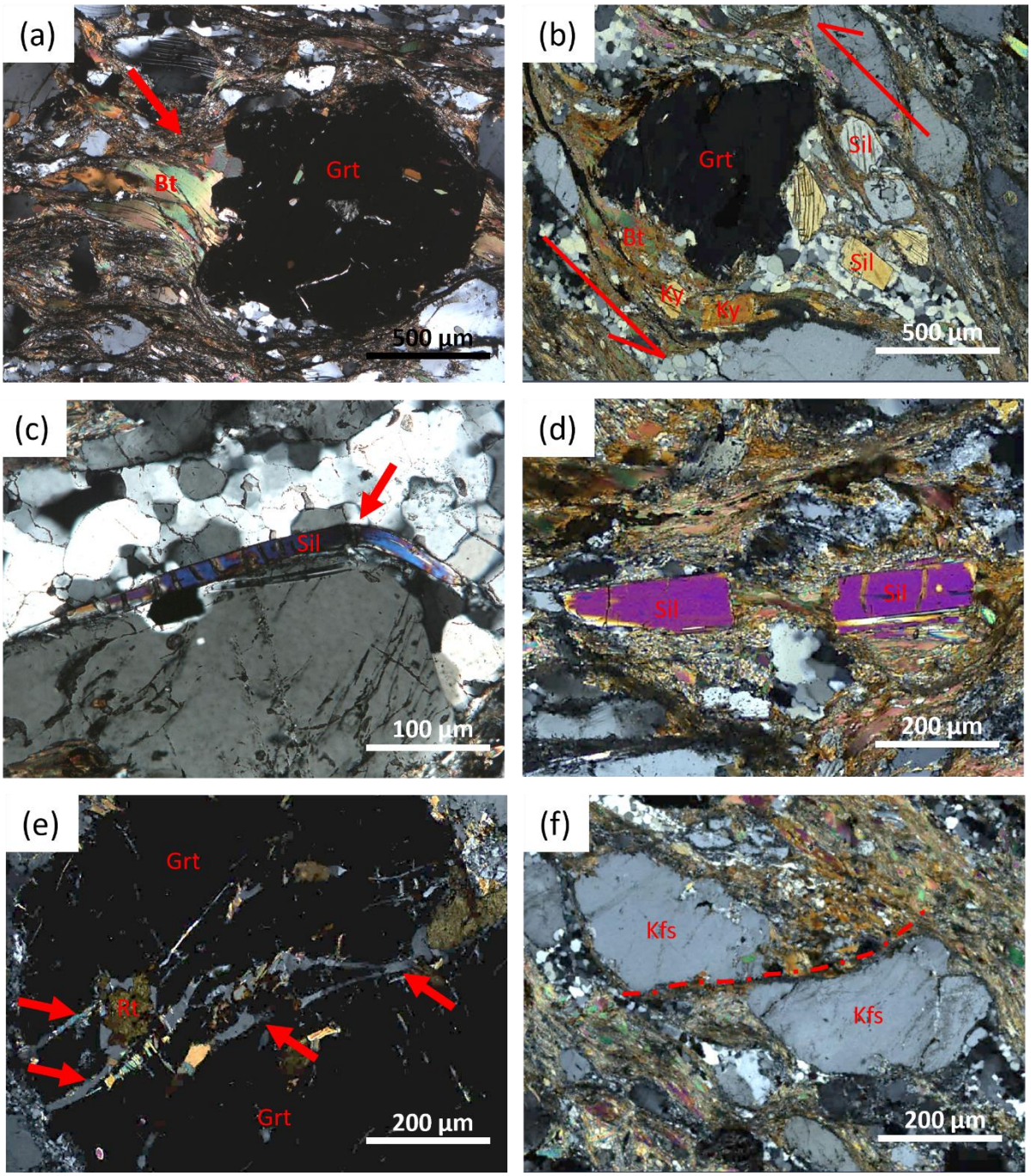

Figure 4.6 Photomicrographs of deformation related microstructures, **(a) –** photomicrograph in XPL of pressure shadow next to the garnet, **(b) -** photomicrograph in XPL of garnet porphyroblast with pressure shadow and shearing indicators, **(c) –** photomicrograph in XPL of a bent sillimanite crystal, **(d) –** photomicrograph in XPL of broken and shifted sillimanite, after pure shearing, **(e) –** photomicrograph in XPL of fractured garnet, **(f) -** photomicrograph in XPL of offset K-feldspar

Chapter V

Mineral chemistry

The composition of garnet, K-feldspar, plagioclase, biotite, and muscovite of sample PS20-A1-02 was analysed by EMP. Results are reported in tables 5.1-5.4.

5.1 Garnet

Garnet is an almandine-rich solid solution, containing pyrope and small amounts of grossular and spessartine (Tab. 5.1). It is generally chemically homogenous, with slight zonation visible in calcium (Grs), magnesium (Prp), and iron (Alm) endmember component. The chemical zoning in large porphyroblast (>2 mm) can be correlated with occurrence of the different inclusions: Grt I (containing NG+MPI+Dia) and Grt II (containing Sil) (Fig 5.1a).

The average composition of inclusion-free garnet is $Alm_{67}Prp_{27}Grs_4Sps_2$ with X_{Mg} = 29 (X_{Mg} = Mg/(Mg+Fe) x 100. The content of all garnet endmembers in % is shown is Fig. 5.1b. The composition of Grt II is characterized by lower X_{Grs} and X_{Alm} contents (3.5 and = 66, respectively) and higher X_{Prp} values (X_{Prp} = 29) than the average composition of garnet. Grt I is characterized by higher content of calcium (X_{Grs} = 5) and iron (X_{Alm} = 68), and lower X_{Prp}= 26, than average garnet (Fig. 5.1c, d, e).

Table 5.1 Representative EMP analyses of garnet, normalized on the basis of 12 O atoms. NG – composition of garnet within the clusters with NG, MPI and Dia. SIL – composition of garnet within clusters of sillimanite needles. Grt I – first generation of garnet, Grt II – second generation of garnet.

	Grt I	Grt II	Grt	Grt	Grt	Grt
Position	NG	SIL	core	mantle	rim	avg.
n. analysis	74	134	52	125	4	
Na_2O	0.02	0.05	0.00	0.00	0.04	0.04
Al_2O_3	21.46	21.93	21.57	21.50	21.64	21.88
TiO_2	0.00	0.02	0.00	0.01	0.02	0.03
MnO	1.17	1.21	1.16	1.29	1.02	1.25
K_2O	0.00	0.01	0.02	0.01	0.03	0.01
MgO	6.71	7.13	7.06	7.28	7.66	7.22
SiO_2	36.48	36.96	37.22	37.29	37.07	37.12
Cr_2O_3	0.00	0.05	0.05	0.02	0.01	0.04
FeO	31.82	31.07	31.25	31.73	31.36	31.43
CaO	1.51	1.23	1.51	1.30	1.53	1.45
P_2O_5	0.00	0.06	0.07	0.00	0.08	0.03
V_2O_3	0.03	0.00	0.00	0.00	0.00	0.02
Total	99.21	99.74	99.91	100.44	100.47	100.51
Na	0.00	0.01	0.00	0.00	0.01	0.01
Al	2.02	2.05	2.01	2.00	2.01	2.03
Ti	0.00	0.00	0.00	0.00	0.00	0.00
Mn	0.06	0.07	0.06	0.07	0.06	0.07
K	0.00	0.00	0.00	0.00	0.00	0.00
Mg	0.80	0.84	0.83	0.86	0.90	0.85
Si	2.92	2.93	2.94	2.94	2.92	2.92
Cr	0.00	0.00	0.00	0.00	0.00	0.00
Fe	2.13	2.06	2.07	2.09	2.06	2.07
Ca	0.13	0.10	0.13	0.11	0.13	0.12
P	0.00	0.00	0.00	0.00	0.00	0.00
V	0.00	0.00	0.00	0.00	0.00	0.00
Total	8.07	8.05	8.05	8.06	8.08	8.07
X_{Prp}	25.6	27.4	26.9	27.4	28.6	27.3
X_{Alm}	68.2	67.0	66.9	66.9	65.6	66.6
X_{Sps}	2.1	2.2	2.1	2.3	1.8	2.2
X_{Grs}	4.1	3.4	4.1	3.5	4.1	3.9
X_{Mg}	27.3	29.0	28.7	29.0	30.3	29.0

X_Z = Z/(Mg+Fe+Mn+Ca) x 100, Z – endmember, X_{Mg} = Mg/(Fe+Mg) x 100,

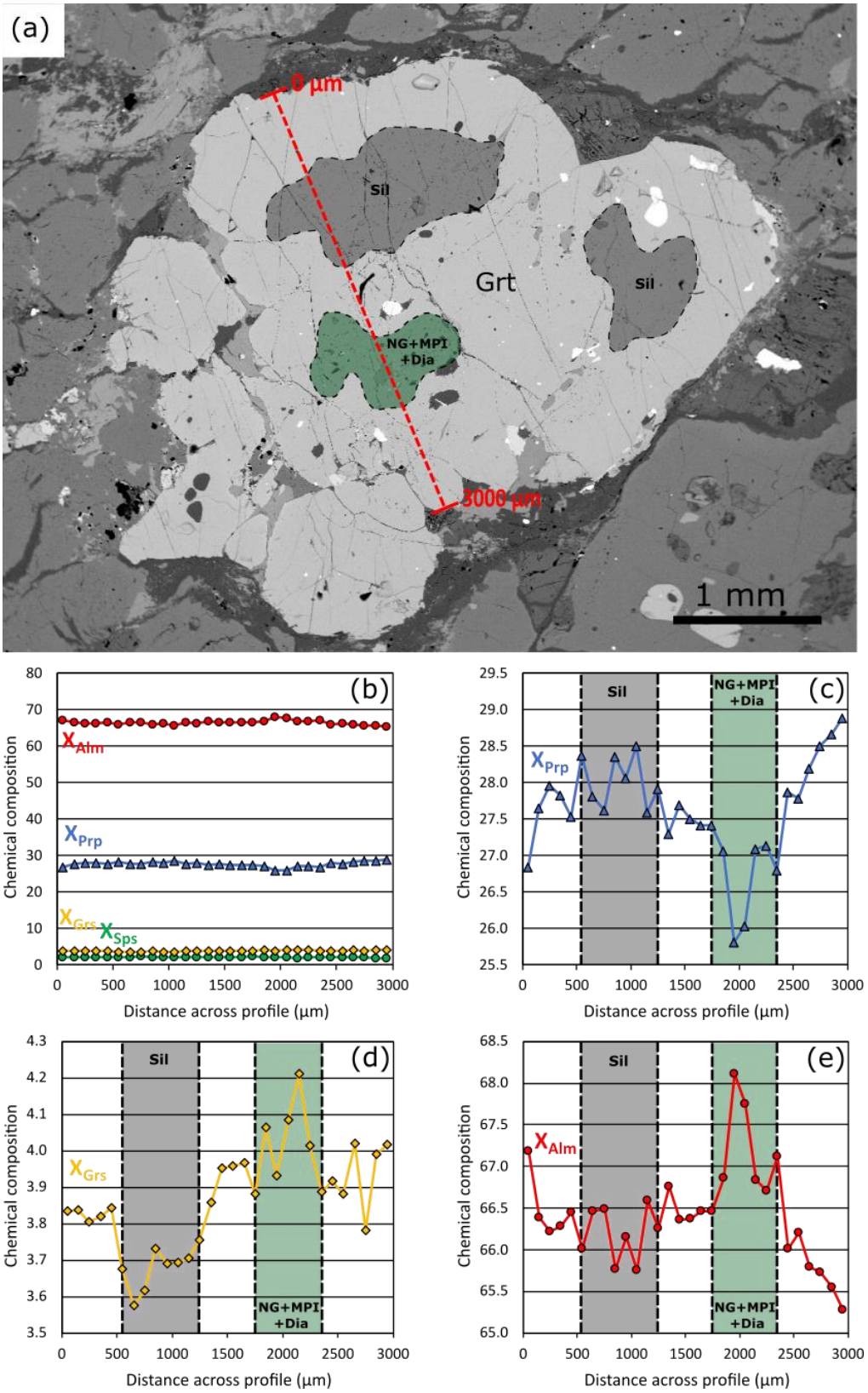

Figure 5.1 (a) – BSE image of a garnet porphyroblast with marked area occupied by clusters of NG, MPI and Dia (NG+MPI+Dia, green field), and area occupied by sillimanite needles (Sil, grey field). Red dashed line indicates position of chemical profile from 0 to 3000 µm shown in plots **(b)** – percentage of all garnet endmembers, **(c)** – close-up at pyrope endmember, **(d)** – close-up at grossular endmember, **(e)** – close-up at almandine endmember.

Elemental mapping of the garnets was conducted for the major elements and less mobile elements such as yttrium, phosphorus, and titanium. Titanium maps of garnet did not display any significant zonation, unlike yttrium and phosphorus which are shown in Fig. 5.2. Garnet interpreted as Grt II displays a sharp, euhedral yttrium enriched zone in the core (Fig. 5.2a). The yttrium-rich zone is positively correlated to the concentration of phosphorus. Phosphorus in garnet II (Fig. 5.2a) displays oscillatory zonation with enriched core and rim. The coarse garnet porphyroblast (shown in Fig. 5.2b) that contain NG, MPI, diamonds (zone ascribed as Grt I) and sillimanite needles (zone ascribed as Grt II) shows a complex zonation, both in yttrium and phosphorus. NG+MPI zone (Grt I) is correlated to high yttrium concentration and low phosphorus concentration while Sil zone (Grt II) is located in a low yttrium area. The same behaviour of yttrium and phosphorus is seen in other garnets containing NG, MPI (Fig. 5.2c and d). Yttrium content is high where NG and MPI occurs, then gradually decrees outwards. In the few larger porphyroblasts (Fig. 5.2b and c), a second yttrium enriched zone might be noticed. Zone where NG+MPI+Dia occurs shows sharp and well visible depletion in phosphorus (Fig. 5.2b,c and d).

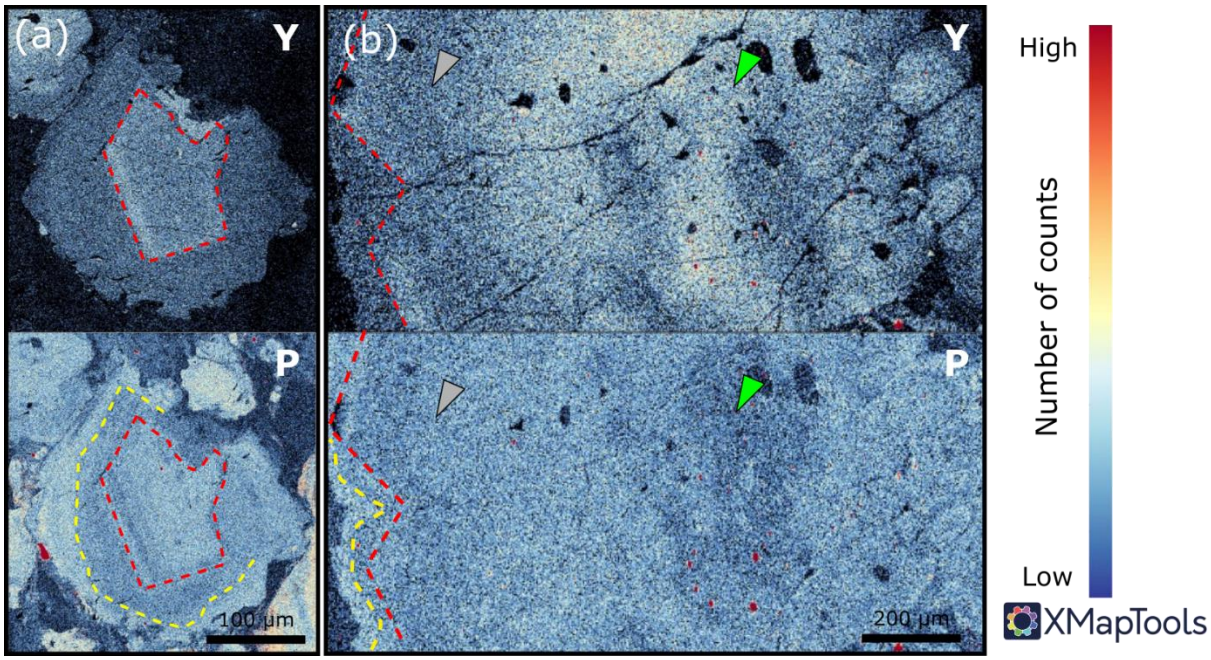

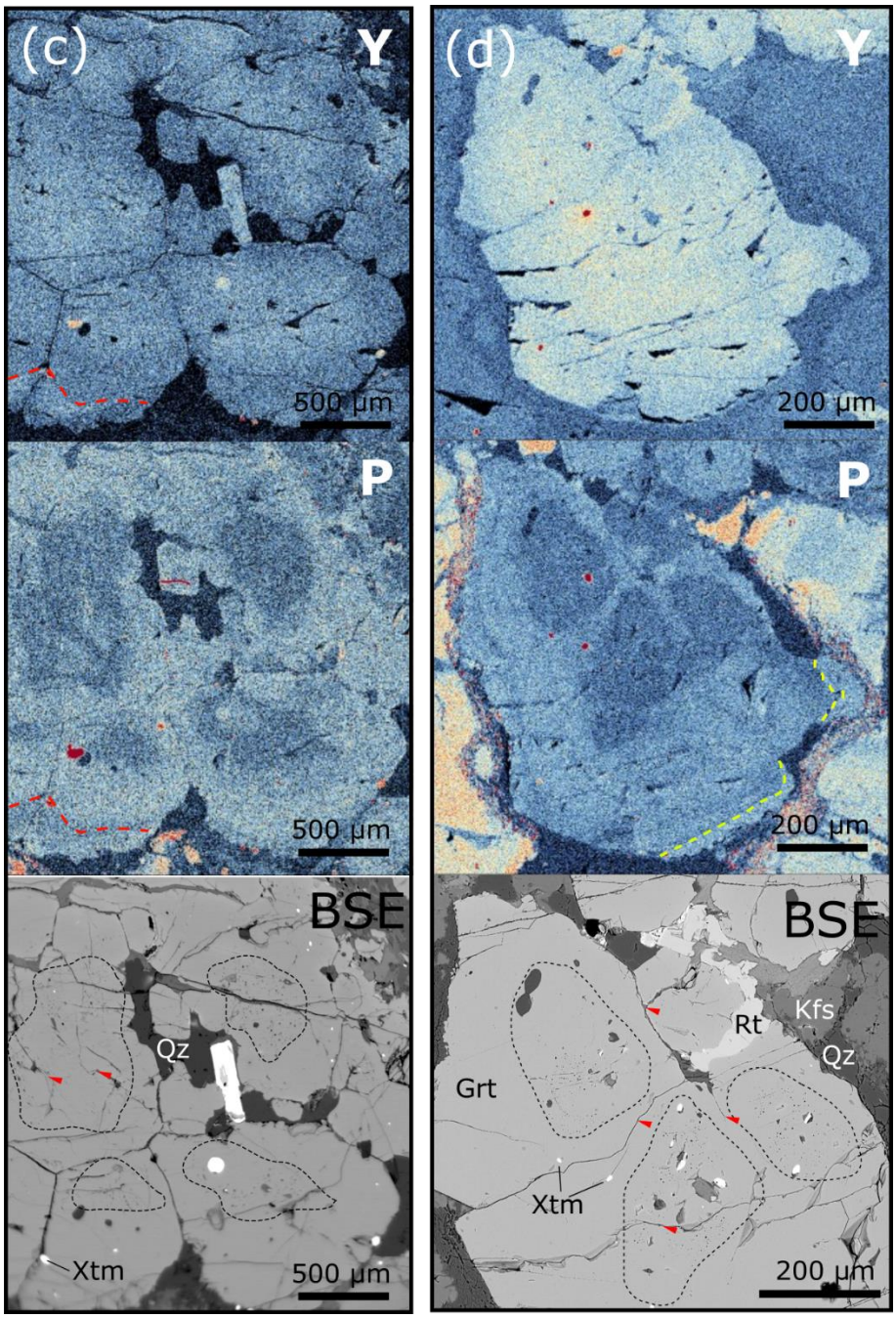

Figure 5.2 Yttrium and phosphorus maps of garnet, **(a)** – garnet ascribed as second generation (Grt II), **(b)** – large garnet (3 mm in diameter) porphyroblast with complex zonation (Grt I in the core and Grt II in the mantle), grey arrow indicate position of sillimanite needles (Sil), green arrow indicate position of NG+MPI+Dia cluster. The same porphyroblast is shown in Fig. 5.1a. **(c)** – aggregate of coalesced garnets ascribed as Grt I, and BSE image with marked clusters of NG+MPI+Dia (black dashed line) and fractures (red arrows), **(d)** – garnet ascribed as first generation (Grt I), dashed black line indicate position of NG+MPI+Dia clusters, red arrows indicate fractures, visible also on phosphorus map. Red dashed line indicates second high-yttrium zone. Yellow dashed line indicates high-phosphorus zone. Elemental maps were processed and enhanced with use of XMapTools (Lanari et al., 2014, 2019).

5.3 Feldspars

K-feldspar in the matrix shows restricted composition (Fig. 5.3) with an average of $Or_{87}Ab_{13}An_{0}$. K-feldspar included in the garnet, instead, shows larger compositional variability ($Or_{78\text{-}93}Ab_{6\text{-}22}An_{<1}$) (Fig. 5.3).

Plagioclase occurring in the matrix is classified as andesine $Ab_{54}An_{45}Or_{1}$, while plagioclase included in garnet varies in composition from andesine to oligoclase. Plagioclase included in the garnet is generally more enriched in albite component, up to $Ab_{87}An_{13}Or_{<0.4.}$ Representative analyses of feldspars are shown in Tab. 5.2.

Table 5.2 Representative microprobe analyses of feldspars, normalization on the basis of 8 O atoms.

	Kfs1	Kfs2	Kfs3	Pl1	Pl2	Pl3	Pl4
position	in mtx	in grt	in grt	in mtx	in grt	in grt	in grt
n. analysis	231	2	44	47	172	216	43
Na_2O	1.46	1.04	5.60	6.54	9.91	9.53	7.65
Al_2O_3	18.39	19.31	19.74	27.96	21.42	21.53	26.78
TiO_2	0.02	0.02	0.05	0.00	0.12	0.00	0.00
MnO	0.01	0.00	0.00	0.00	0.03	0.04	0.05
K2O	14.61	15.40	8.61	0.18	0.06	0.19	0.12
MgO	0.01	0.02	0.00	0.00	0.02	0.03	0.02
SiO_2	64.74	64.93	66.00	56.69	66.24	65.51	58.57
Cr_2O_3	0.04	0.00	0.00	0.00	0.05	0.00	0.01
FeO	0.04	0.46	0.23	0.00	0.45	0.24	0.27
CaO	0.09	0.03	0.07	9.53	2.65	3.45	7.97
Total	99.41	101.21	100.30	100.90	100.95	100.52	101.44
Na	0.13	0.09	0.49	0.57	0.84	0.81	0.66
Al	1.00	1.04	1.04	1.47	1.10	1.11	1.40
Ti	0.00	0.00	0.00	0.00	0.00	0.00	0.00
Mn	0.00	0.00	0.00	0.00	0.00	0.00	0.00
K	0.86	0.90	0.49	0.01	0.00	0.01	0.01
Mg	0.00	0.00	0.00	0.00	0.00	0.00	0.00
Si	2.99	2.96	2.96	2.53	2.89	2.87	2.59
Cr	0.00	0.00	0.00	0.00	0.00	0.00	0.00
Fe	0.00	0.02	0.01	0.00	0.02	0.01	0.01
Ca	0.00	0.00	0.00	0.46	0.12	0.16	0.38
Total	5.00	5.01	5.00	5.03	4.98	4.98	5.04
X_{Ab}	13.1	9.3	49.5	54.9	86.8	82.4	63.0
X_{Or}	86.4	90.6	50.1	1.0	0.4	1.1	0.7
X_{An}	0.4	0.1	0.4	44.2	12.8	16.5	36.3

X_Z = Z/(Na+K+Ca) x 100, Z – endmember component

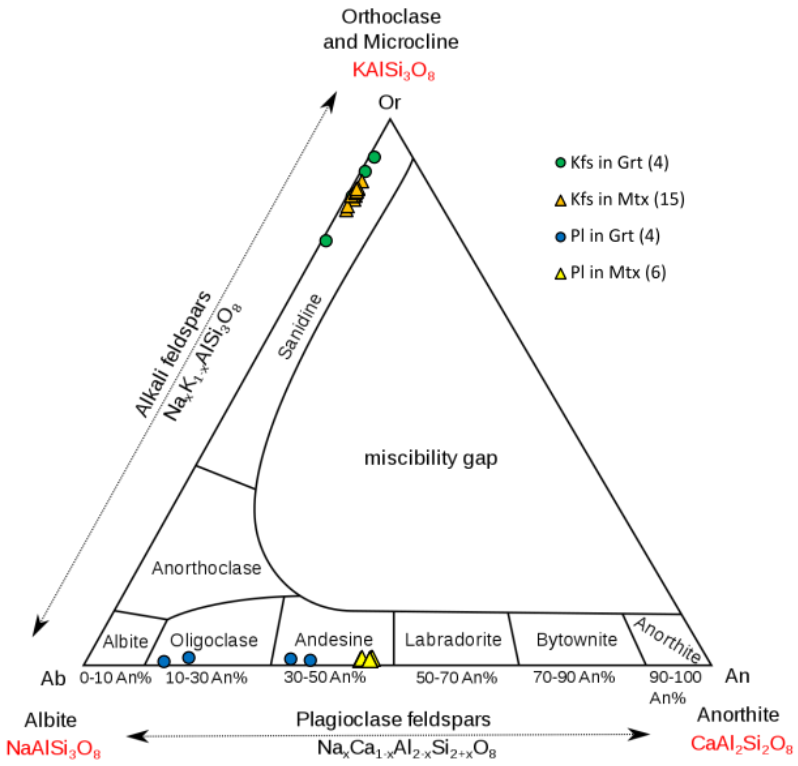

Figure 5.3 Kfs-Ab-An ternary classification diagram. Feldspars were divided according to their textural position: in Grt – included in garnet, in Mtx – occurring in the matrix. Number of analytical points is in brackets.

5.4 Biotite

The composition of biotite varies depending on its microstructural position (Fig. 5.4). Biotite occurring in the matrix (Bt in Mtx) has an average X_{Mg} of 0.6, and Ti (apfu) = 0.2. X_{Mg} and Ti content show negative correlation. Biotite occurring in microfractures of the garnet (Bt in cracks) has similar content of Ti (apfu) = 0.2 and X_{Mg} = 0.5 in comparison to the biotite from the matrix. Biotite included in garnet (Bt in Grt) shows wider compositional differences (ranging from 0.1 to 0.4 Ti (apfu)) and similarly displays a negative correlation between X_{Mg} and Ti. In general, it has higher content of Ti (apfu) = 0.3 and X_{Mg} = 0.7 than biotite from the matrix and from the microfractures in garnet. Two distinctive trends well visible in Fig. 5.4 may be noticed: one formed from Bt in Mtx and Bt in microfractures and a second trend formed by Bt in Grt. Representative analyses of biotite from different textural position are shown in Tab. 5.3.

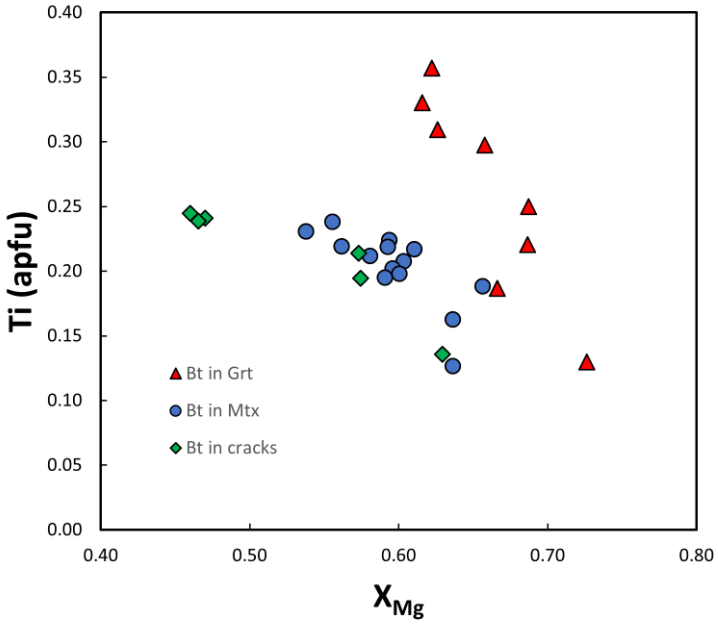

Figure 5.4 Plot of X_{Mg} versus Ti (apfu) of analysed biotite; classification according to the microstructural position.

5.5 Muscovite

Muscovite in the matrix contains a phengitic component to various degrees, shown in Fig. 5.5, and contains from 3.07 to 3.21 Si (apfu). Muscovite in garnet shows higher affinity to phengite and contains 3.12 Si (apfu). The muscovite included in the garnet shows significant contents of Na indicating a paragonite component (Na from 0.2 to 0.4 apfu). Representative analyses of white mica are in Tab. 5.3.

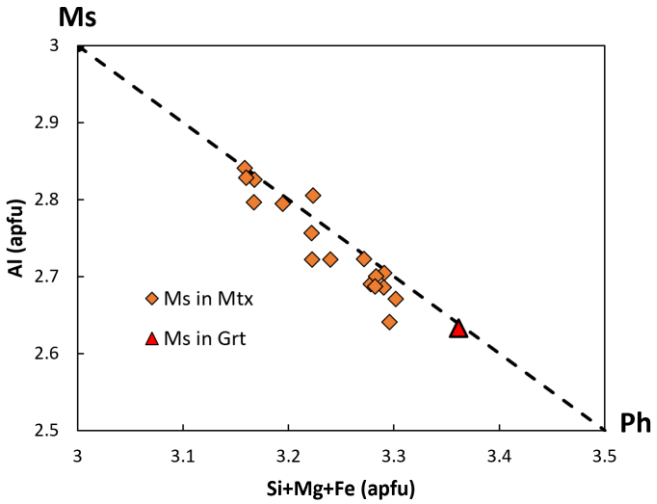

Figure 5.5 Plot of Al vs. Si+Mg+Fe of analyzed white micas; the dashed line indicates the theoretical celadonite substitution ($Al^{VI}\ Al^{IV} \leftrightarrow (Mg, Fe)^{VI}\ Si^{IV}$) in phengite solid solution. After Park et al. (2020).

Table 5.3 Representative microprobe analyses of micas, normalization done based on 11 O atoms.

	Bt1	Bt2	Bt3	Bt4	Ms1	Ms2	Ms3	Pg1
Position	in grt	in grt	in cracks	in mtx	in grt	in mtx	in mtx	in grt
n. analysis	171	168	169	210	214	238	15	40
wt%								
Na_2O	0.33	0.12	0.07	0.09	0.30	0.38	0.53	2.96
$Al2O_3$	17.71	17.94	18.20	17.42	33.67	35.67	34.32	38.68
TiO_2	6.28	4.14	3.75	3.74	0.75	0.41	0.91	0.25
MnO	0.07	0.01	0.05	0.01	0.02	0.02	0.02	0.00
K_2O	9.52	9.90	9.94	9.92	10.71	10.67	10.86	6.84
MgO	12.54	9.46	11.67	11.12	1.00	0.19	1.06	0.25
SiO_2	36.83	36.19	37.72	36.99	47.32	46.84	46.62	45.59
Cr_2O_3	0.14	0.00	0.00	0.00	0.00	0.02	0.03	0.01
FeO	13.56	19.02	15.49	15.45	2.20	0.58	1.43	0.65
CaO	0.03	0.00	0.03	0.00	0.00	0.01	0.01	0.51
Total	96.99	96.78	96.92	94.74	95.98	94.80	95.78	95.74
Na	0.05	0.02	0.01	0.01	0.04	0.05	0.07	0.37
Al	1.58	1.64	1.63	1.60	2.63	2.80	2.67	2.97
Ti	0.36	0.24	0.21	0.22	0.04	0.02	0.05	0.01
Mn	0.00	0.00	0.00	0.00	0.00	0.00	0.00	0.00
K	0.92	0.98	0.96	0.99	0.91	0.91	0.92	0.57
Mg	1.41	1.09	1.32	1.29	0.10	0.02	0.06	0.02
Si	2.78	2.80	2.86	2.88	3.14	3.12	3.21	2.97
Cr	0.01	0.00	0.00	0.00	0.00	0.00	0.00	0.00
Fe	0.86	1.23	0.98	1.01	0.12	0.03	0.04	0.04
Ca	0.00	0.00	0.00	0.00	0.00	0.00	0.00	0.04
Total	7.97	8.00	7.97	8.00	6.98	6.94	7.01	7.00
X_{Mg}	0.62	0.47	0.57	0.56				

X_{Mg} = Mg/(Mg+Fe)

5.6 Rutile

Rutile crystals present in the rock were divided into five types based on textural position: Rt in Grt core, Rt in Grt mantle, Rt in Grt rim, Rt in Grt corona and Rt in rock matrix (Rt in Mtx) (detailed description of rutile generations is in Chapter IV). The concentrations of Al, Ti, V, Zr, Cr, Fe and Nb were measured in 22 rutile grains by EMP. Analyses of representative rutile grains are shown in Tab. 5.4. In addition, 21 analyses of rutile grains included in garnet were provided by Klonowska et al. (in preparation).

Special care was given in the analysis of Zr in rutile, which has been later evaluated for its geothermometric significance. All Zr contents of rutile from the different textural positions are shown in Fig 5.6a. Rutile in garnet core is characterized by low Zr concentration (40 to 300 ppm) which, instead, increases in rutile in garnet mantle (400 to 700 ppm). Regarding rutile grains included in garnet, the highest values were detected in crystals located at the host rim (up to 875 ppm), even though rutile in this textural position shows high variability of Zr content (300 to 875 ppm). In the rock matrix, rutile shows the widest range of Zr concentration (100 – 908 ppm). Rutile classified as Rt in Grt corona shows Zr contents from 100 to 420 ppm. The variability of Zr contents within single rutile grain is significant, but it does not exceed 450 ppm difference. Representative rutile compositions are shown in Tab. 5.4.

The concentration of Fe in rutile varies from 1500 to 10000 ppm. However, most analyses show Fe contents close to the mean value (3200 ppm). Such high (>1000 ppm) Fe concentrations are typical of high-grade metamorphic rocks (Meinhold, 2010). The few analyses showing extreme contents of Fe >6000 ppm might be contaminated by secondary fluorescence artifact on the EMP due to proximity of garnet or ilmenite (Kooijman et al., 2012; Ewing et al., 2013). However, SEM backscattered observations show that rutile grains do not contain ilmenite exsolutions or zircon inclusions at micron scale (Fig. 5.6c).

Rutile grains included in garnet show variable concentrations of Nb (300 – 10000 ppm) and Cr (13 – 2000 ppm), which generally increase from garnet core to the rim (Fig. 5.6b). The rutile from the rock matrix and garnet corona contains relatively high content of Nb (up to 10000 ppm), and low content of Cr (up to 500 ppm). Almost all rutile analyses show negative values of log(Cr/Nb) ranging from -2.4 to 0.34, as expected for metasedimentary rocks (Triebold et al., 2012).

Table 5.4 Representative microprobe analyses of rutile.

no. analysis	17	123	79	99	130	138	147	124	159
grain	Rt18	Rt20	Rt27	Rt42	Rt40	Rt13	Rt15	Rt3	Rt2
position	in Grt core	in Grt core	in Grt mantle	in Grt rim	in Grt rim	in Grt corona	in Grt corona	in Mtx	in Mtx
wt%									
Al_2O_3	0.01	0.04	0.01	0.07	0.08	0.05	0.05	0.22	0.09
SiO_2	0.00	0.05	0.01	0.01	0.01	0.01	0.01	0.01	0.00
TiO_2	99.99	101.32	101.93	102.15	101.61	102.98	102.54	102.65	101.30
V_2O_3	0.54	0.00	0.00	0.00	0.00	0.00	0.00	0.00	0.00
ZrO_2	0.04	0.02	0.08	0.12	0.08	0.04	0.05	0.11	0.12
Cr_2O_3	0.18	0.02	0.04	0.00	0.05	0.02	0.02	0.02	0.03
FeO	0.14	1.39	0.48	1.00	0.91	0.29	0.53	0.24	0.69
Nb_2O_5	0.40	0.36	0.22	0.58	0.73	0.15	0.40	0.30	1.21
Total	101.00	103.19	102.78	103.93	103.46	103.53	103.61	103.55	103.44
ppm									
Zr	296	148	601	875	578	301	360	825	908
Cr	1259	109	306	31	352	105	135	164	189
Nb	2774	2531	1518	4076	5114	1068	2823	2062	8472
Fe	1120	10809	3733	7754	7045	2243	4129	1900	5377

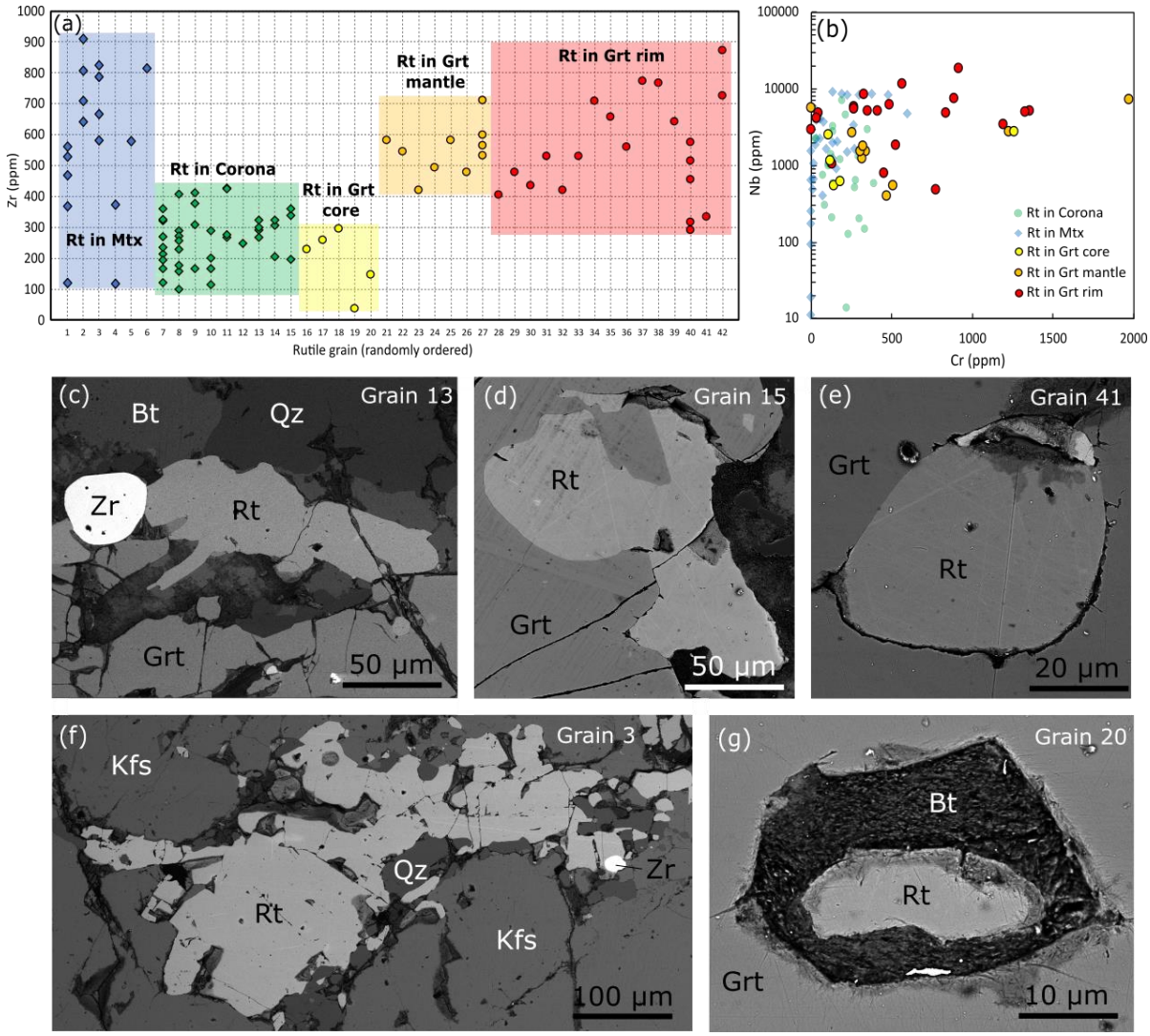

Figure 5.6 (a) – Zr content in rutile grains from different textural positions, **(b)** – Nb (ppm) vs. Cr (ppm) binary diagram of rutile from different textural positions; **(c)** – BSE image of rutile grain (Rt in corona) adjacent to zircon and quartz, **(d)** – BSE image of rutile grain (Rt in corona), merged with garnet, **(e)** – BSE image of rutile grain (Rt in Grt rim), **(f)** – BSE image of rutile grain (Rt in Mtx), **(g)** - BSE image of rutile grain (Rt in Grt core).

5.7 Zr-in-Rutile thermometry

Zirconium-in-rutile thermometry (ZiR) is extensively used in metamorphic petrology since the temperature-dependent reaction (1) was empirically and experimentally calibrated in a number of studies (Zack et al., 2004; Watson et al., 2006; Tomkins et al., 2007) and most recently revised by Kohn (2020).

$$ZrSiO_4 = SiO_2 + ZrO_2 \quad (1)$$

In order to be applicable and quantitative, the ZiR requires that zircon, quartz and rutile are present in the rock and can exchange components. This requirement is fulfilled as shown on Fig. 5.6c and 5.6f, where the three minerals seem to be microstructurally in equilibrium. The thermometer equations refined by Kohn (2020) for the coesite and α-quartz stability fields (equations 2 and 3, respectively) are:

$$T(°C) = \frac{73910+0.247\cdot P(bar)-0.130\cdot C(ppm)}{129.65-R\cdot\ln[C(ppm)]} - 273.15 \quad (2)$$

$$T(°C) = \frac{71360+0.378\cdot P(bar)-0.130\cdot C(ppm)}{130.66-R\cdot\ln[C(ppm)]} - 273.15 \quad (3)$$

where T is the calculated temperature, C represents the zirconium content in rutile, R is the gas constant (8,31 $J\cdot mol^{-1}\cdot K^{-1}$) and P is the assumed pressure.

To estimate then temperature experienced by the studied paragneiss during partial melting, rutile grains were selected for ZiR thermometry based on textural position. Rt in Grt core, Rt in Mtx and in addition Rt in Grt rim. The highest concentrations of zirconium were used from each rutile as the maximum concentration of zirconium reflects maximum experienced temperature.

Pressure used to calculate temperatures were taken from work of Klonowska et al. (2017). Two metamorphic stages were defined in Åreskutan paragneiss, one at UHP conditions (4.2 GPa) and second at HP conditions (1.1 GPa). Therefore, isolines for each textural generation of rutile were calculated.

The results of ZiR thermometry are shown in Fig. 5.7. The Rt in Grt core displayed temperature of 744 ± 20˚C at 4.2 GPa, Rt in Grt mantle show 860 ± 20˚C at 4.3 GPa while Rt in Grt rim gave temperature of 741 ± 20˚C, at 1.1 GPa. Rt in Mtx gave a temperature of 880 ± 20˚C, for 4.2 GPa. Temperatures recorded by rutile included in garnet core are lower than previous estimations obtained with use of Ti-in-Quartz thermometry (T = 875˚C; Klonowska et al., 2017). However, the temperature obtained from Rt in Grt mantle, and Rt in Mtx for 4.3 GPa are consistent with previous works.

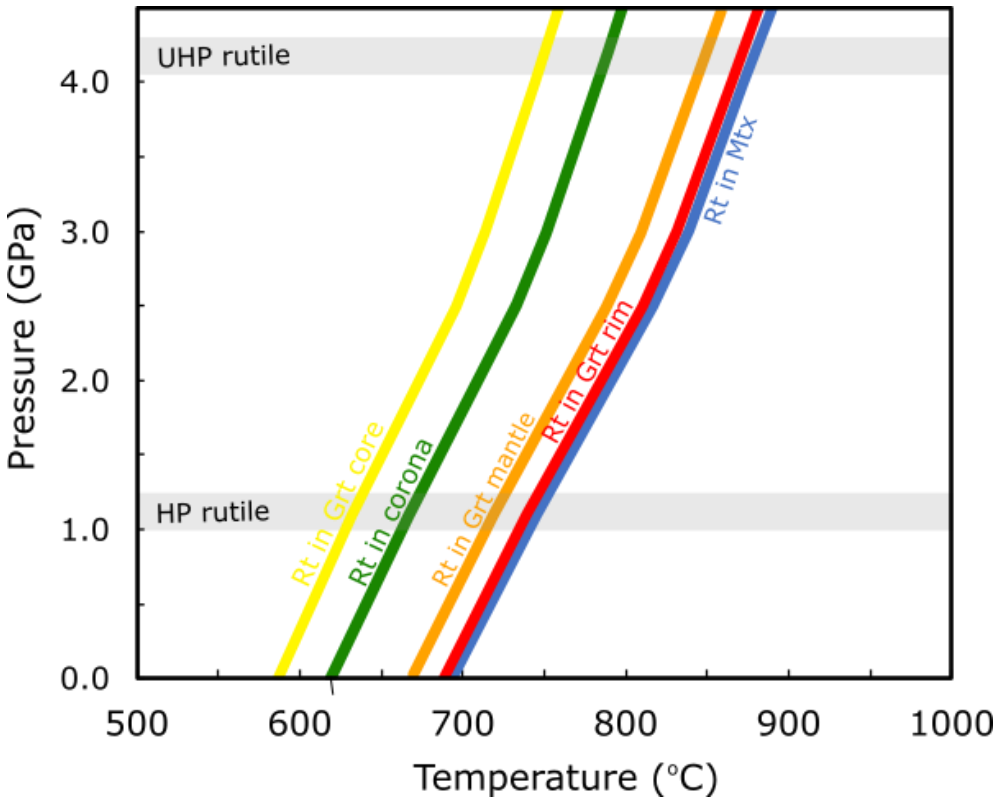

Figure 5.7 P-T diagram showing the results of Zr-in-rutile geothermometry for the rutile form different textural position. Gray shades indicate inferred pressure for UHP rutile, (P = 4.2 GPa), and HP rutile, (P = 1.1 GPa).

Chapter VI

Nanogranitoids, multiphase inclusions and diamonds in garnet

6.1 Occurrence of inclusions

Garnet that contains clusters of NG, MPI and diamond inclusions is commonly found in the leucocratic parts of the rock, while in the melanocratic portions garnet is usually inclusion-free or contains small number of mineral inclusions (Qz, Bt, Fs). Irregular clusters containing NG and MPI inclusions occur in Grt I, precisely in their cores and mantles (Fig. 6.1a). The larger (< 20 μm) inclusions are filled with solid phases, whereas the smaller ones (< 10 μm) often contain voids. The larger inclusions are interpreted as NG while smaller ones as MPI (Fig. 6.1b). Both NG (Fig. 6.1c, d) and MPI (Fig. 6.1e, f) often display well developed negative crystal shape imposed by the host garnet. The NG observed in 2D cuts are relatively rare with respect to MPI, the number of NG within the single cluster varies from 3 to 10 inclusions, whereas the rest – 15 to 40 are MPI or mixed inclusions. The differentiation between NG and MPI occurring abundantly in analysable size (10 μm) was done mostly by SEM-EDS analysis due to similarities in mineral composition and difficulties with detecting feldspar by micro-Raman spectroscopy. The detailed investigation also showed the presence of mixed inclusions, composed of minerals characteristic for both, NG and MPI. Within the investigated clusters, metamorphic microdiamond occurs as a single mineral inclusion or as one of the solid phases in MPI (Fig. 6.1f). Investigation of NG and MPI spatial distribution within the clusters was performed by XRM microtomography with an approach similar to that used by Parisatto et al. (2018). Three-dimensional (3D) reconstruction of the clusters (Fig. 6.2) clearly showed that NG and MPI always occur together within the clusters, and they are randomly distributed therein. Another mineral inclusion often presents in the proximity to the NG+MPI+Dia clusters is kyanite and rutile.

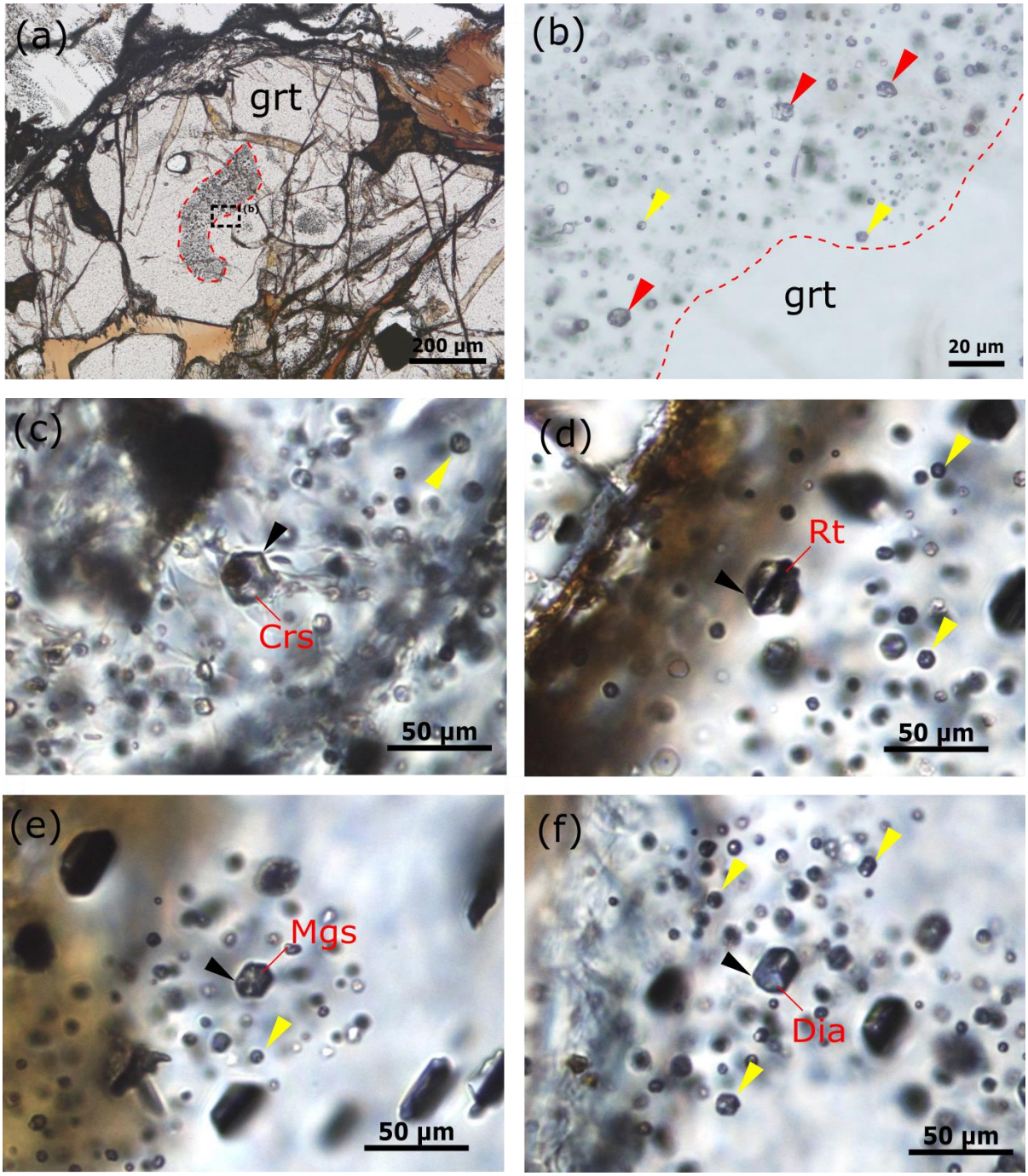

Figure 6.1 (a) – photomicrograph in PPL of garnet with irregular cluster of NG and MPI inclusions located in the core (dashed red line), **(b)** – close-up of the cluster, showing the spatial relationship between NG (red arrow) and MPI (yellow arrow), **(c)** – photomicrograph in PPL of NG with cristobalite, **(d)** – photomicrographs in PPL of NG with rutile, **(e)** – photomicrograph in PPL of MPI with magnesite, **(f)** – photomicrograph in PPL of MPI with microdiamond. Black arrows indicate well developed negative crystal shape. Yellow arrows indicate small (< 5µm) MPI.

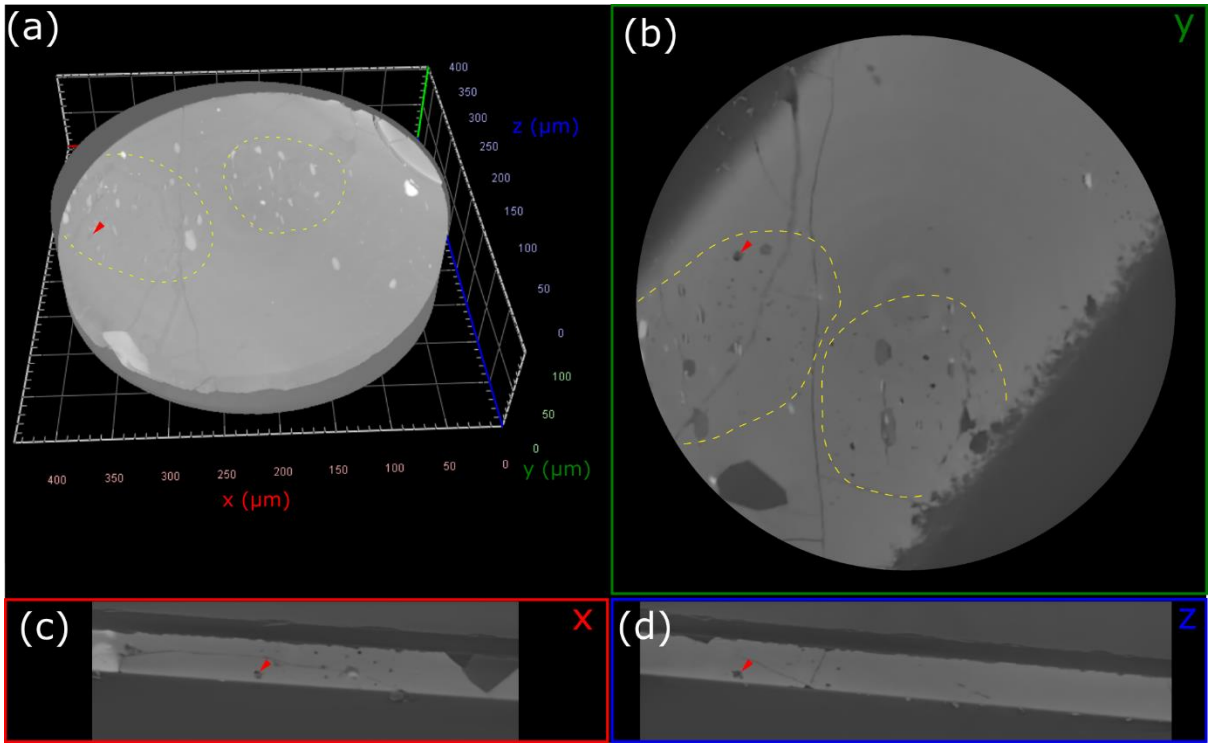

Figure 6.2 (a) – 3D reconstructed part of garnet core with two inclusion (NG, MPI) clusters (marked with yellow dashed line). Tomographic 2D slice (Z = 853) oriented along Y (b), X (c) and Z (d) axis direction. Red arrows point at the same NG at different cross sections.

6.2 Nanogranitoids

NGs in most cases show negative crystal shape, range in size from 10 to 20 µm in diameter, and often display typical decrepitation 'tails' (Fig. 6.3). Fractures commonly propagate radially from the inclusion towards the hosting garnet (Fig. 6.3a). Sometimes, fractures can be filled with biotite as shown on Fig. 6.5b. The "necking" texture is observed (Fig. 6.5d), showing a snapshot of NG in the shape maturation process.

NGs are composed of quartz or cristobalite, various micas (biotite, phlogopite, white mica), K-feldspar, plagioclase, rarely pyrophyllite and rarely? carbonates (magnesite, siderite, calcite or REE-calcite and dolomite), as shown in Fig. 6.3b-f. NGs also contain apatite, rutile, zircon, pyrite or pseudobrookite, which are interpreted as trapped accessory phases (Fig. 6.3e). Few features may indicate that these accessory minerals were accidentally trapped with melt (Barich et al., 2014) such as: 1) their relatively large size with respect to the size of whole inclusion, 2) their low solubility

in granitic melts, 3) the presence of indentations of these minerals within the walls of inclusion, 4) the presence of these minerals in the host. The micrometre-scale droplets of melt chemically adhered to accessory phases during the peritectic garnet growth and were entrapped together as shown for trapped zircon by Darling (2013). Texture of phases inside NG suggests the following order of crystallization: mica -> feldspar -> quartz -> (in case of mixed inclusions – Fig. 6.3e) carbonate and aluminosilicate. (Fig. 6.3b).

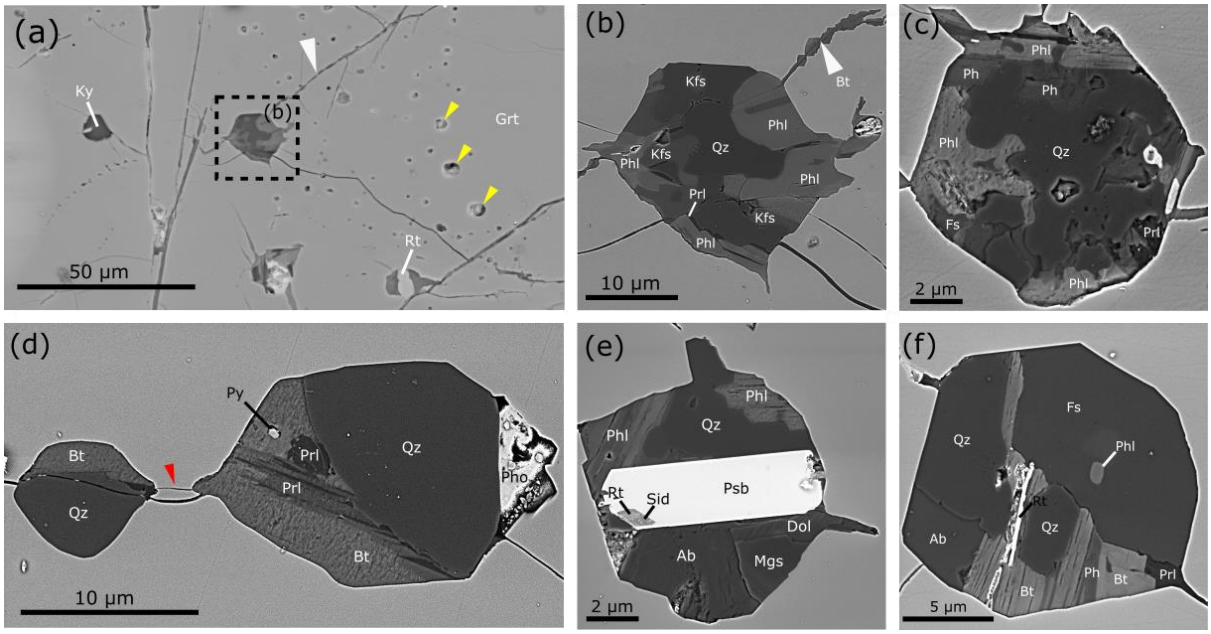

Figure 6.3 BSE images of **(a)** – a NG in a cluster of MPI inclusions (marked with yellow arrow) occurring in close vicinity of kyanite and rutile inclusions, from **(b)** to **(f)** - texture and shape of single NG inclusion. White arrows **(a)** and **(b)** indicate decrepitation fractures filled with biotite. Red arrow in **(d)** indicates well matured necking of NG. Psb – pseudobrookite.

In addition to electron microscopy imagining coupled with EDS, micro-Raman spectroscopy analisys was carried out to identify mineral phases in NG. The most abundant phases detected by Raman spectroscopy are quartz (Fig. 6.4d, c), cristobalite (Fig. 6.4b), phlogopite (Fig. 6.4a), phengite (Fig. 6.4e), biotite (Fig. 6.4b) and carbonates, namely magnesite (Fig. 6.6b). Feldspar is commonly ocuring mineral in NG, confirmed by BSE and EDS, however during the Raman anaysis it was rarerly detected (Fig. 6.4f).

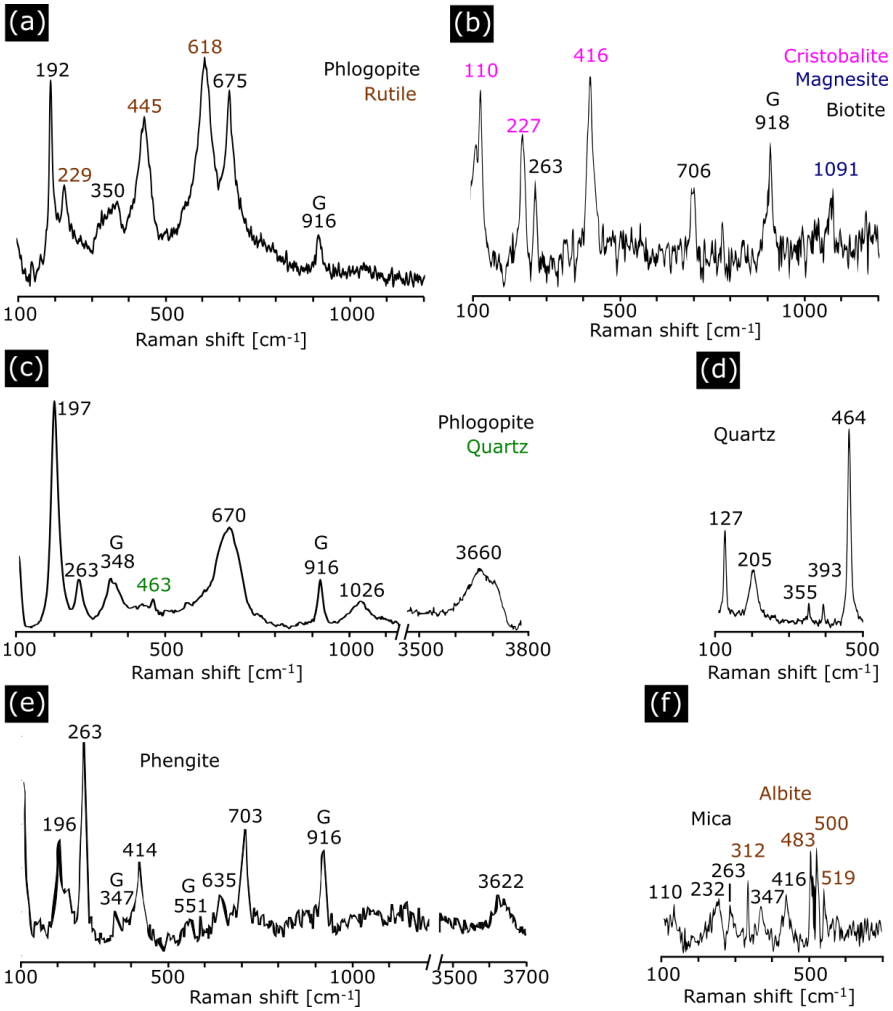

Figure 6.4 Representative Raman spectra (cm^{-1}) of the NG. **(a)** – mixed spectrum of phlogopite and rutile, **(b)** – mixed spectrum of cristobalite, magnesite and biotite, **(c)** – mixed spectrum of phlogopite and quartz, **(d)** – quartz, **(e)** – phengite, **(f)** – rarely observed spectrum of feldspar – albite, mixed with mica bands.

6.3 Multiphase inclusions

The MPIs, similarly to NGs, often display well developed negative crystal shape (Fig. 6.5a, b, and c). They are composed of solid phases (Fig. 6.5a - f), but most of them also contain cavities. The size of the observed empty spaces varies from small interstitial cavities (Fig. 6.5g, h) to almost entire empty inclusions (Fig. 6.5i). These empty spaces in the exposed polished inclusions are interpreted as formerly occupied by fluid. Only the smallest MPIs (< 5 µm) are almost entirely empty after the exposing on the surface therefore, they were composed mainly of the liquid phase (Fig. 6.5i).

This feature was also confirmed by Raman spectroscopy, as smallest MPIs (< 5 µm) usually contain residual fluid. The major mineral assemblage of MPI is carbonates, quartz/cristobalite, pyrophyllite and phlogopite. MPI may rarely contain feldspar, graphite, or diamond.

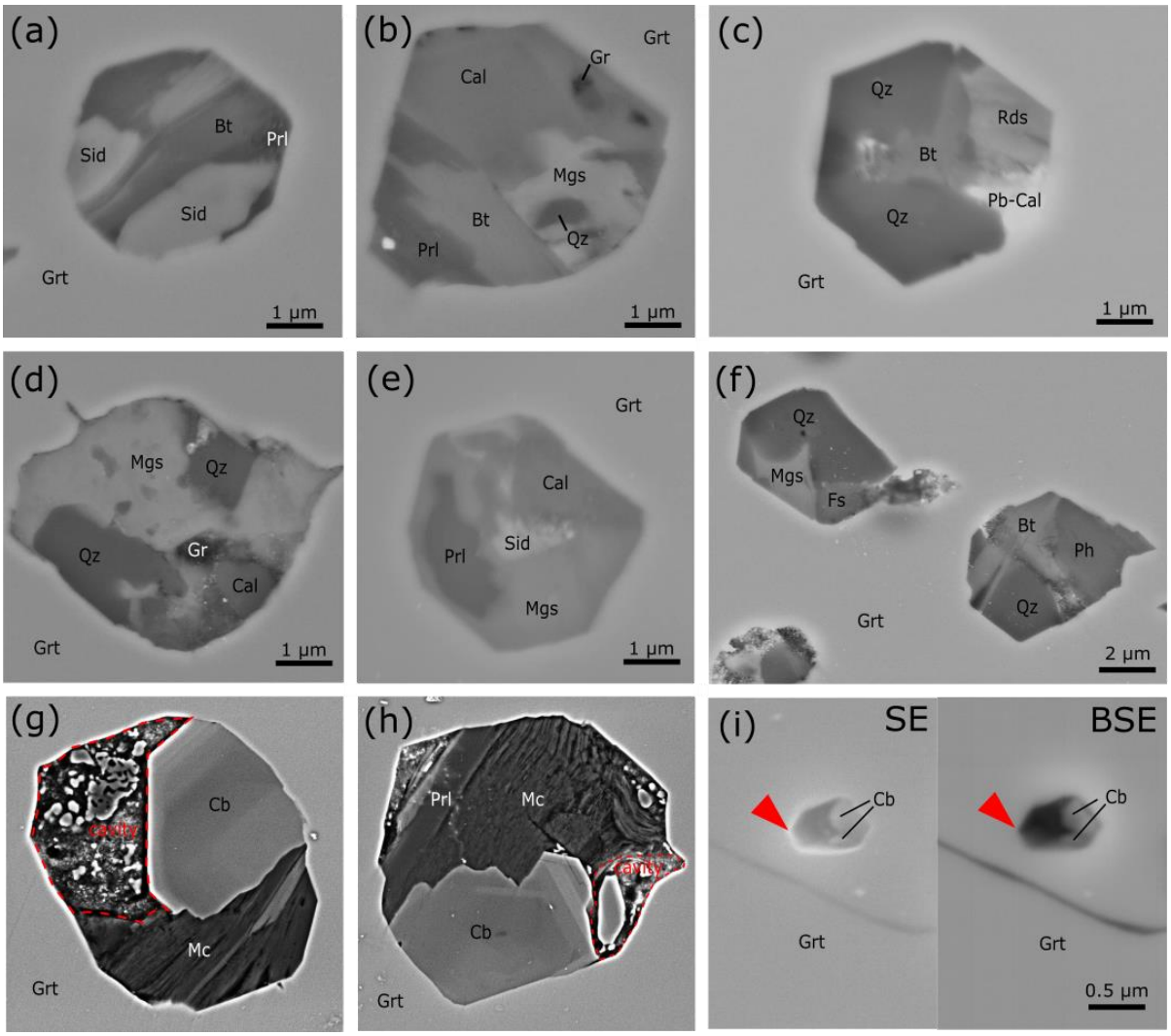

Figure 6.5 BSE images of MPI from (a) to (h). **(a)** – MPI composed of Sid, Bt and Prl. **(b)** – MPI composed of Cal, Mgs, Bt, Prl and Gr. **(c)** – MPI composed of Qz, Rds, Bt and Pb-Cal with well-developed hexagonal negative crystal shape. **(d)** – MPI composed of Mgs, Cal, Qz, and Gr. **(e)** - MPI composed of Mgs, Cal, Qz and Gr. **(f)** – two mixed inclusions composed of Qz, Mgs, Fs and Qz, Ph and Bt. **(g)** and **(h)** – High resolution (FE-SEM) images of MPI composed of Cb, Mc, and Prl with visible cavity filled with polishing material (dashed red line). Cb show oscillatory zonation in composition, darker zone is calcite, brighter zones are enriched in Mg and Fe. **(i)** – BSE and SE image of small (1 µm) MPI mostly composed of fluid with visible Cb crystals, grown on the garnet wall. Red arrows indicate well developed negative crystal shape.

The most common minerals detected in MPI by micro-Raman spectroscopy are carbonates (Fig. 6.6a) such as magnesite, siderite, calcite, vaterite (polymorph of calcite), and dolomite. Other minerals are phlogopite (Fig. 6.6b), pyrophyllite (Fig. 6.6c), quartz (Fig. 6.6d) or cristobalite (Fig. 6.6f), rarely kaolinite (Fig. 6.6d), and sulphates such as Mg-sulphate pentahydrate shown in Fig. 6.6e, recognized based on peak position from Frezzotti et al. (2012). Residual fluids were also detected such as CO_2, N_2 and CH_4 (Fig. 6.6g). In one MPI, diamond (Fig. 6.6h) was recognized coexisting together with graphite, carbonates, and pyrophyllite. The density of CO_2 was calculated based on peak position of Fermi diad (Wang et al. 2011) and varies from 0.25 g/cm^3 in MPI composed mostly of solid phases to 1.02 g/cm^3 in fluid dominated inclusions.

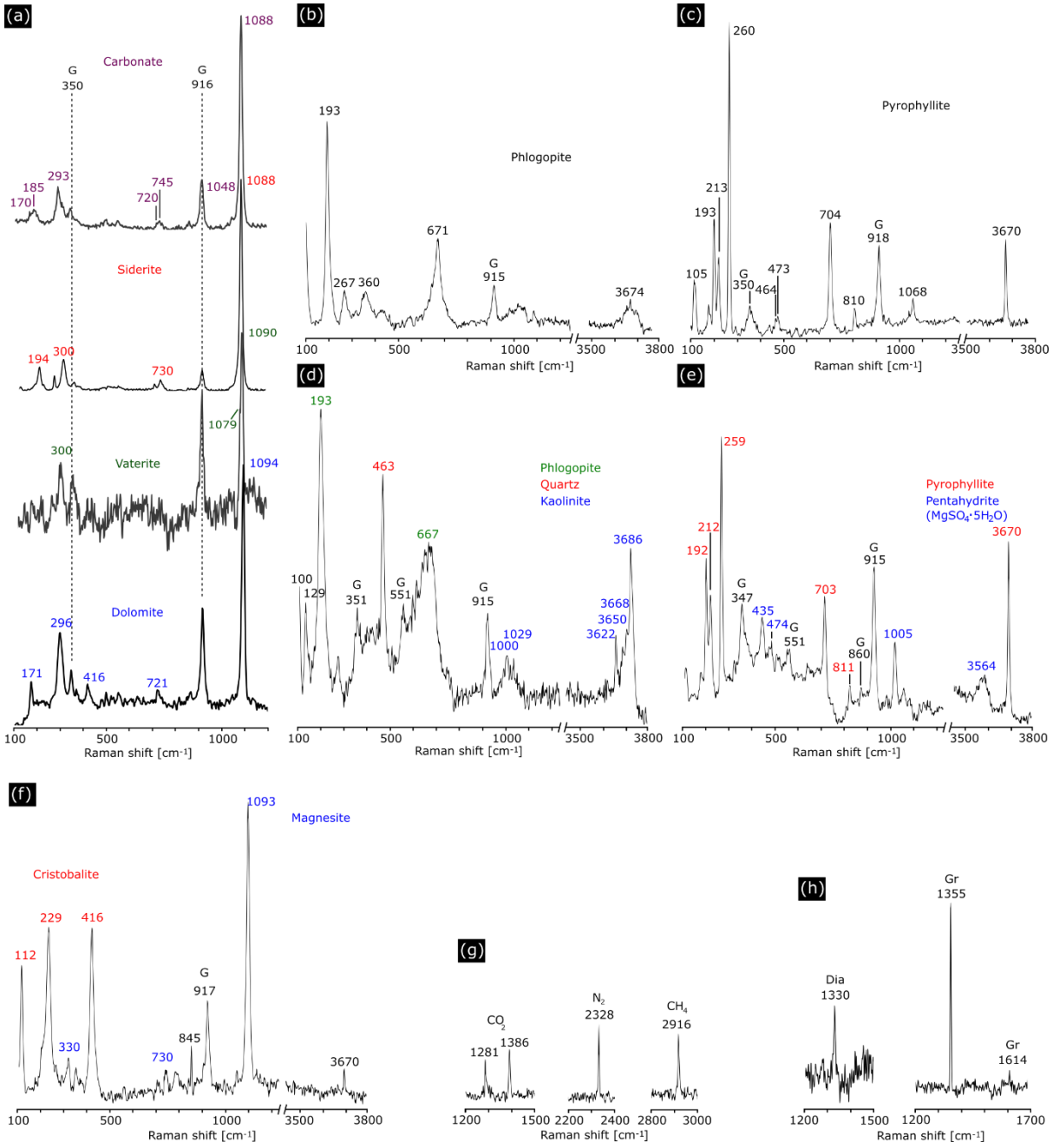

Figure 6.6 Representative Raman spectra (cm^{-1}) of minerals and fluids within MPI. **(a)** – overlayed spectra of carbonates, from the top: carbonate, siderite, vaterite and dolomite, **(b)** – mixed spectrum of cristobalite, magnesite and biotite, **(c)** – mixed spectrum of phlogopite and quartz, **(d)** – quartz, **(e)** – phengite, **(f)** – rarely observed mixed spectrum of feldspar – albite and mica.

6.4 Metamorphic diamond in MPI

Three diamond crystals were found by Raman spectroscopy during this study, confirming the discovery of Klonowska et al. (2017). Microdiamonds can occur as a single mineral inclusion within the cluster or as a part of MPI assemblage alongside carbonates, pyrophyllite, graphite, carbon dioxide and methane. All microdiamonds

were detected as single mineral inclusions or as part of MPI entirely enclosed in the host garnet (i.e., the investigated microdiamonds occur beneath the garnet surface). Downshifted position of the main diamond peak 1330 cm^{-1} (sp3-bonded carbon) is typical for the metamorphic microdiamonds (Majka et al., 2014; Klonowska et al., 2017, 2021). The sample preparation and verification procedure were described in the Chapter III. Only one diamond spectrum (Fig. 6.8h) was of sufficient quality to calculate the full width half maximum (FWHM) = 8.2 cm^{-1} with use of Omnic Software. Plotted on a peak position vs. FWHM diagram (Fig. 6.7), the microdiamond shows characteristic features of other diamonds found in Åreskutan area (Klonowska et al., 2021), which contrast to diamonds used in abrasives and polishing pasts used in preparation laboratories.

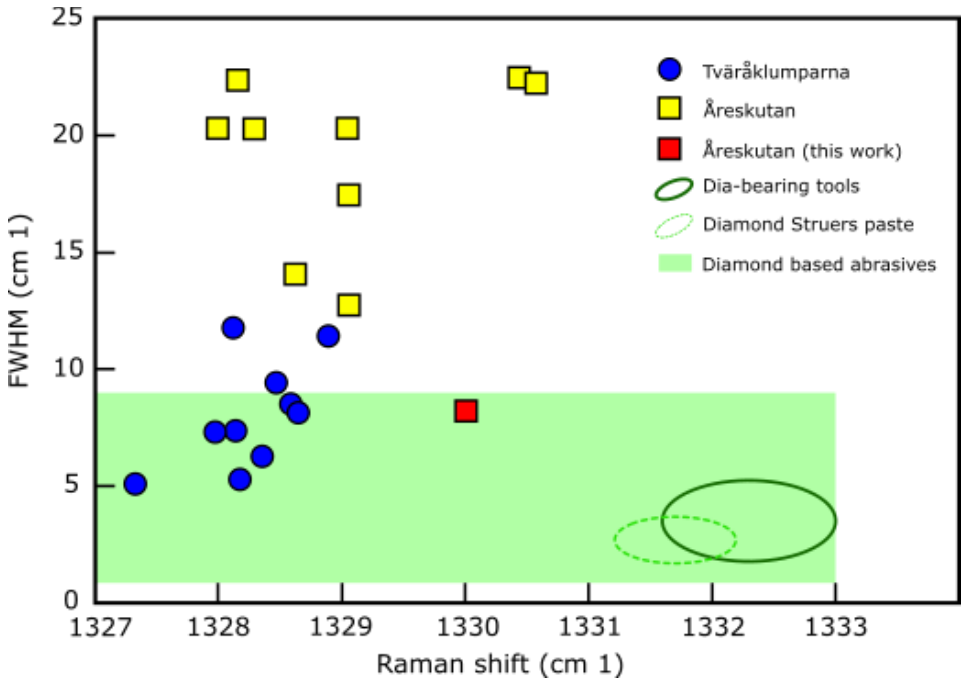

Figure 6.7 Plot of the full width of half maximum (FWHM) vs. the position of the main first-order Raman band of diamond. The plot includes natural metamorphic diamonds from SNC, and diamonds used in abrasives. After Klonowska et al. (2021)

Chapter VII

Re-melting experiments and melt composition

7.1 Homogenization of nanogranitoids

The P-T conditions used for the experimental re-melting were defined based on petrographic observations, ZiR geothermometry and previous estimates of Klonowska et al. (2017), in order to closely reproduce the trapping conditions of NG (Tab. 7.1). After the first series of experiments (Exp1-3), the degree of homogenization of NGs was assessed by preliminary SEM imaging. Formation of matrix melts was also assessed. Drilled sample was usually larger than the garnet and contained small portion of the matrix, molten matrix creates a risk of contamination of inclusions. Complete homogenization was obtained in Exp1 and Exp2 runs, however many of remelted NG contained glass with other phases, inferred as unmelted relicts. In both Exp1 and Exp2, minerals in the matrix recrystallized, but quenched glass was not detected. In Exp3 run, all remelted NGs contained glass and relict or newly formed minerals. Therefore, for the following runs at 900˚C, the duration of experiments was extended to 48h, and pressure was raised to 4.5 GPa. The same changes were applied also for the 950˚C run. In experimental runs Exp4, Exp6, Exp7 the result was identical to Exp2: quenched melt was not observed in the matrix, some of the NGs were totally remelted, while many of them contained solid phases. In the Exp5 run NGs were fully remelted, but the presence of healed fractures across the garnet was observed, most of the former matrix was composed of quenched melt.

Table 7.1 Conditions and products of all experimental runs, rec. – recrystallized.

Exp. run	P (GPa)	T (˚C)	t (h)	Matrix	Inclusion homogeneity
Exp1	4	850	24	rec. minerals	glass, glass + relict phases
Exp2	4	900	24	rec. minerals	glass, glass + relict phases
Exp3	4	950	24	rec. minerals + glass	glass + relict phases, glass + new phases
Exp4	4.5	900	48	rec. minerals	glass, glass + relict phases
Exp5	4.5	950	48	glass + rec. minerals	glass + new phases
Exp6	4.5	900	48	rec. minerals	glass, glass + relict phases
Exp7	4.5	900	48	rec. minerals	glass, glass + relict phases

The best homogenization was acquired at 850, 900˚C, and 4 - 4.5 GPa, where fully remelted NGs have been observed (Fig. 7.1a-e), with preserved primary negative shape and no interaction with hosting garnet. However, also in these runs many of NGs did not re-homogenise completely at these conditions. Glass is observed to coexist with unmelted minerals like mica (Fig. 7.1f), quartz (Fig. 7.1g) or feldspar (Fig. 7.1h). Sometimes graphite can be observed occurring as flakes or rounded grains (Fig. 7.1g). In some remelted NGs, rounded cavities are present, interpreted as bubbles (Fig. 7.1e). In one inclusion remelted at 900˚C and 4 GPa, pyroxene was found. Sometimes slight reaction with the garnet was observed, especially in glasses containing unmelted phases (Fig. 7.1f-h). NGs remelted at 950˚C and 4 GPa usually contain other phases e.g., mica (Fig. 7.1i) inferred as unmelted phases, or clinopyroxene (Fig. 7.1j) ascribed as newly formed peritectic phase. Rims of recrystallized garnet are often present indicating interaction between melt and host; in this case the primary the negative shape of NG is not preserved (Fig. 7.1j, i). These portions of brighter garnet in the reaction zone (Fig. 7.1i) are enriched in Fe and depleted in Mg with respect to the composition of garnet before the experiment. Fe-enriched garnet is also observed as bright rims surrounding healed fractures. Fractures are sometimes widened and filled with glass (Fig. 7.1l), that indicate percolation of melt within the garnet during the experiment. This feature is only observed in garnets from 950˚C experimental runs. A darker garnet reaction zone is sometimes observed around inclusions from 950˚C run (Fig. 7.1j), but rarely in inclusions remelted at 900˚C. In this case the newly formed garnet contains more Mg and less Fe than the garnet before the experiment.

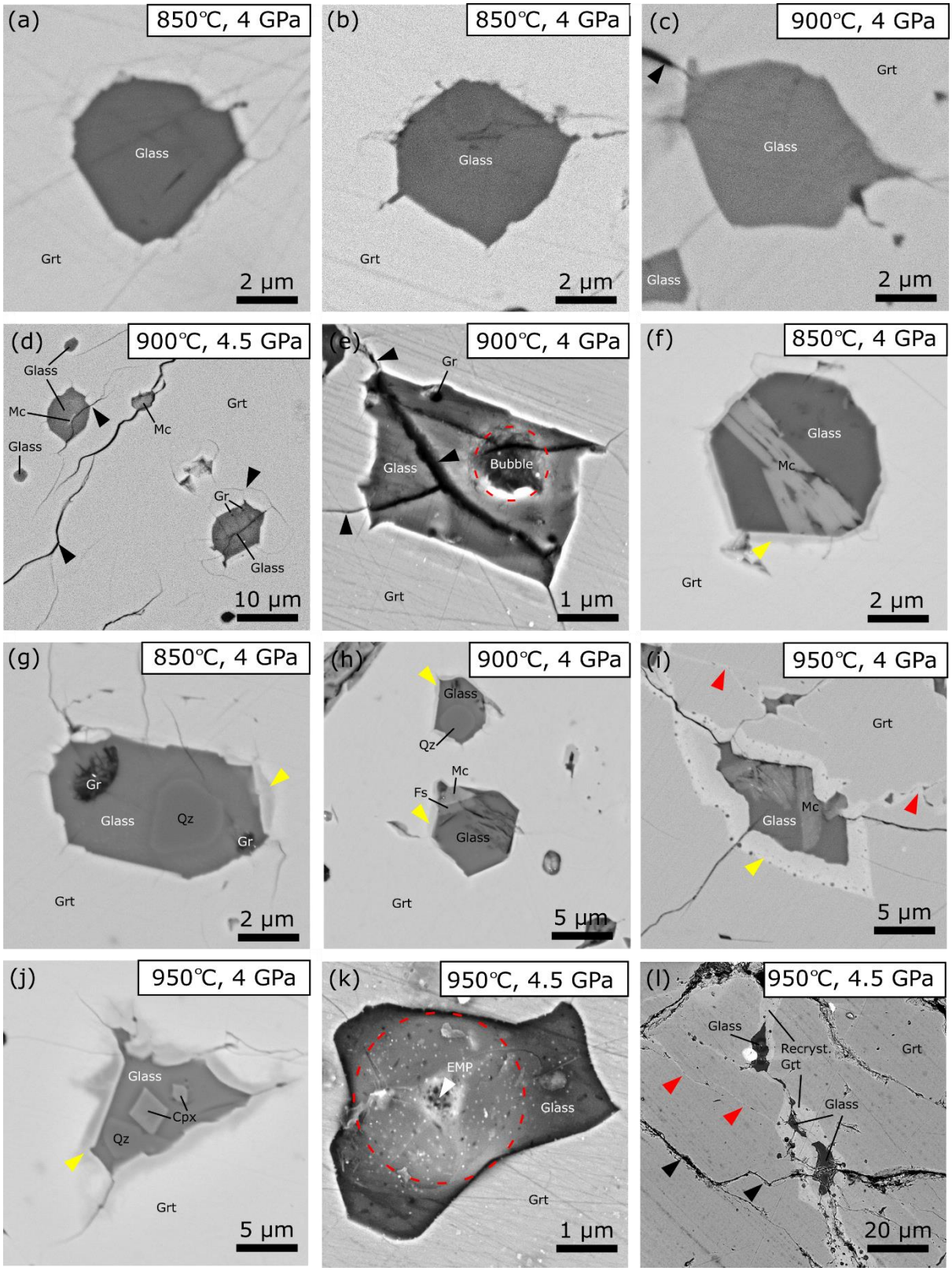

Figure 7.1 BSE images of experimentally remelted NG, **(a), (b), (c)** – homogenous glass with well-preserved negative shape, **(d)** – cluster of homogenous glassy inclusions, **(e)** – glass with bubble, fractures formed after quenching are marked with black arrow **(f)** – glass with relict mica crystal; the negative shape of the inclusion is preserved, **(g)** – glass with relict quartz crystal and graphite flakes, a slight reaction with garnet is visible (yellow arrow), **(h)** – two remelted nanogranitoids with unmelted

quartz, mica and feldspar. Notice the slight reaction with garnet (yellow arrow), **(i)** – glass with mica crystals. A strong reaction with garnet (yellow arrow) and healed fractures (red arrow) are visible, **(j)** – glass with quartz and clinopyroxene; the negative crystal shape of the inclusion is not preserved, **(k)** – glass, negative shape is not preserved, dashed red circle shows damage zone on the surface after EMP analysis (analytical point marked with white arrow), **(l)** – melt pockets within the garnet following the fractures, a newly formed garnet is visible, healed fractures formed during the experimental run (red arrow), and fractures formed after quenching (black arrow)

7.3 Composition of UHP anatectic melt

In total, 160 remelted NGs were analysed by EMP from all 7 experimental runs. The chemical composition of quenched glasses remelted at 950˚C confirmed earlier SEM observations as being contaminated by percolation of the melt within the garnet and matrix. These melts contain significant enrichment in Cl and P_2O_5 with respect to glasses remelted at 850˚C and 900˚C (Fig. 7.2a). The same trend might be observed in the K_2O content (Fig. 7.2b). These elements probably were liberated throughout melting of the matrix (mostly mica and K-feldspar) and contaminated remelted inclusions within the garnet. Therefore, glasses formed at 950 ˚C cannot be considered as primary UHP anatectic melts. Composition of the glasses from 850˚C and 900˚C runs was carefully examined taking into account texture of remelted NG, degree of homogeneity and chemical composition. One of the steps of chemical verification is shown in Fig. 7.2c, d where ratio of MgO, FeO and CaO contents were compared with composition of the garnet. All compositions altered by reaction with garnet, or other interactions, or contaminated during the EMP analysis (contamination related to the small size of some inclusions) were disregarded.

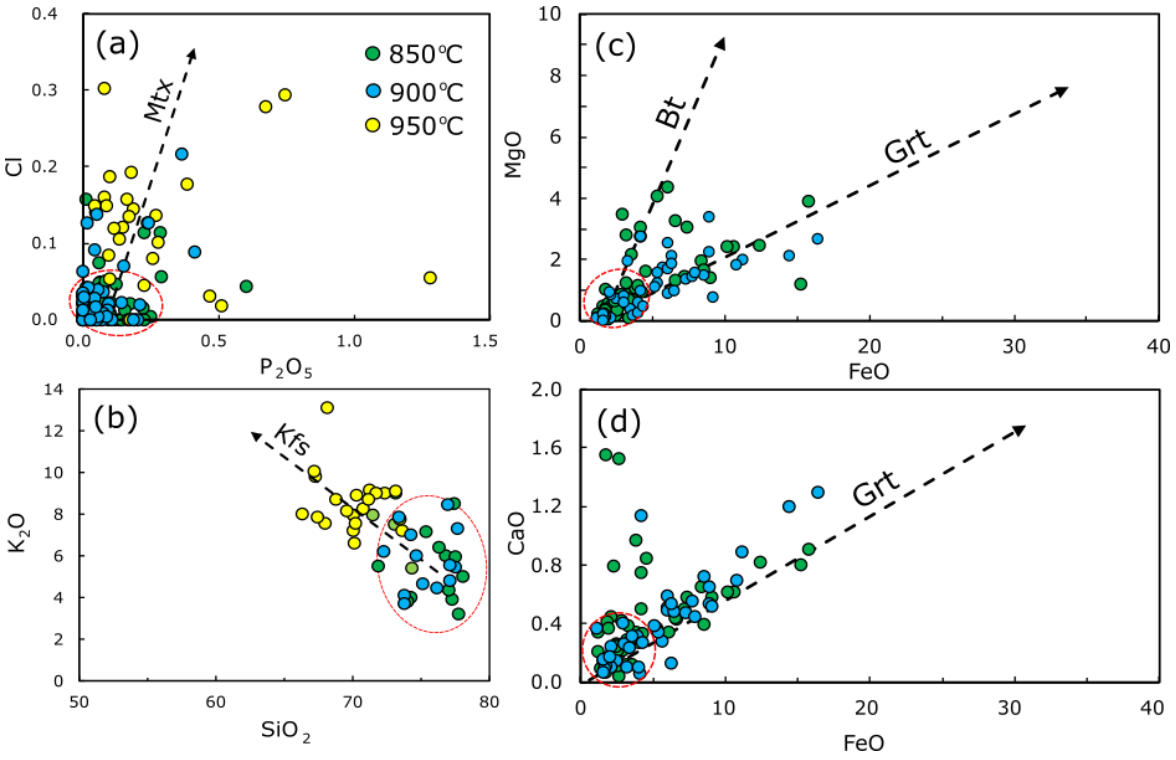

Figure 7.2 Bivariate plots, with all chemical analyses at different stage of data examination, details in the text. Values are expressed in wt%. Plots of MgO vs. FeO **(c)** and CaO vs. FeO **(d)** with marked dashed arrows pointing to composition of Grt and Bt. **(a)**, plot of Cl vs. P_2O_5, dashed black arrow points towards the composition of matrix melts, **(b)**, plot of K_2O vs. SiO_2, dashed arrow points towards composition of Kfs. Green circles represent composition of glasses from 850˚C experimental runs, blue from 900˚C and yellow from 950˚C. Red dashed circles are marking the area of reliable glasses.

Twelve analyses from homogenous inclusions with considered primary composition were selected and used for further interpretation (Tab. 7.2). Sixteen more compositions of glasses containing small modal amounts of relict phases (quartz, mica) or other minor imperfections (interaction rim with garnet or visible bubble) were also considered and plotted on diagrams.

Natural melts derived from re-homogenized NGs are rhyolitic in composition, with SiO_2 content ranging between 72 and 77.5 wt%, and high alkali content (Na_2O+K_2O = 8.1 - 11.7 wt%), similarly to experimentally produced UHP melts and MI from eclogite. Compositions derived from glasses with other phases and bubbles display more variable contents of alkalis ranging from 6.5 wt% up to 11% (Fig. 7.3a). These melts are from peralkaline to peraluminous in composition (Fig. 7.3b). Homogenous glasses show a more restricted range of values, clustering around AI=0,

ASI=1, while most of compositions derived from glasses with other phases and bubbles fall into the peraluminous field, with exception of 3 analyses located in peralkaline field. Experimentally produced melts show a similar compositional range.

Table 7.2 Major element composition of homogenous NG on anhydrous basis. Total iron as FeO.

No. anal.	2	3	10	16	27	44	5	6a	6b	32	73	8		
P (GPa)	4	4	4	4	4	4	4	4	4	4.5	4.5	4		
T (˚C)	850	850	850	850	850	850	850	850	850	900	900	850		
Size (µm)	˜10	˜10	>10	˜10	<10	˜10	>10	>10	>10	>10	˜10	>10	**Avg.**	**SD**
Wt%														
SiO_2	73.82	73.81	72.29	73.45	75.13	74.30	77.53	77.13	76.18	77.73	76.97	74.69	75.25	1.73
TiO_2	0.03	0.05	0.11	0.06	0.09	0.06	0.00	0.03	0.00	0.08	0.00	0.42	0.08	0.11
Al_2O_3	12.47	13.11	13.65	13.36	11.98	12.23	11.36	11.63	11.61	10.52	11.78	11.48	12.10	0.87
FeO	3.35	3.90	2.67	1.75	1.78	3.14	2.51	2.56	2.56	1.61	1.56	1.24	2.39	0.78
MnO	0.09	0.10	0.00	0.06	0.01	0.17	0.06	0.00	0.09	0.05	0.04	0.00	0.06	0.05
MgO	0.83	0.62	0.40	0.30	1.01	0.59	0.18	0.35	0.35	0.23	0.02	0.19	0.42	0.28
CaO	0.25	0.34	0.04	0.12	0.13	0.26	0.26	0.22	0.25	0.07	0.16	0.21	0.19	0.09
Na_2O	4.91	4.29	4.59	3.02	4.95	2.17	2.60	2.51	4.45	2.31	0.94	5.62	3.53	1.38
K_2O	4.13	3.73	6.22	7.86	4.69	6.99	5.46	5.57	4.46	7.30	8.47	6.03	5.91	1.46
Cl	0.05	<0.01	0.02	0.00	0.00	0.01	0.03	<0.01	0.01	0.01	0.00	<0.01	0.02	0.02
P_2O_5	0.06	0.05	0.00	0.04	0.23	0.07	0.00	0.00	0.05	0.09	0.06	0.10	0.06	0.06
H_2O^a							4.58	6.85						
CO_2^a							0.72	0.12						
EMP Total	84.03	89.31	90.11	90.97	96.41	88.58	88.16	93.10	90.66	92.57	87.44	92.02	90.28	3.03
K_2O+Na_2O	9.04	8.02	10.81	10.88	9.63	9.17	8.05	8.07	8.91	9.61	9.42	11.65	9.44	1.13
$MgO+FeO+TiO_2$	4.21	4.57	3.18	2.10	2.89	3.79	2.70	2.94	2.91	1.92	1.57	1.85	2.89	0.91
K_2O/N_2O	0.84	0.87	1.35	2.60	0.95	3.22	2.10	2.22	1.00	3.16	8.97	1.07	2.36	2.16
Na#	0.64	0.64	0.53	0.37	0.62	0.32	0.42	0.41	0.60	0.33	0.14	0.71	0.48	0.17
ASI	0.96	1.12	0.95	0.98	0.89	1.05	1.07	1.10	0.92	0.89	1.07	0.71	0.98	0.11
AI	-0.001	0.020	-0.006	-0.001	-0.012	0.011	0.012	0.015	-0.005	-0.012	0.010	-0.042	-0.001	0.016
CIPW normative minerals														
Q	28	34	22	25	32	34	42	41	34	40	39	33	34	6
Ab	45	41	38	26	38	20	24	23	37	14	8	28	29	11
Or	27	25	39	49	30	46	35	36	28	45	52	39	38	9

ASI = molar $Al_2O_3/(CaO+K_2O+Na_2O)$, AI = molar $Al_2O_3 – (K_2O+Na_2O)$, Na# = molar $Na_2O/(Na_2O+K_2O)$, a – measured by NanoSIMS

These melt compositions coming from natural samples have been compared with experimentally produced UHP melts, selected from previous works (Schmidt et al., 2004; Hermann and Spandler, 2008; Schmidt, 2015). These experimental melts were produced from pelitic starting materials, which have been pressurized and heated to desired conditions. In total, 7 analyses from the literature were chosen for comparison, based on composition of starting material, volatile content, and pressure-

temperature conditions. In addition, other natural melt compositions from melt inclusions (MI) and re-homogenized NGs trapped in UHP eclogite from Saidenbach Bohemian Massif, Germany, (Borghini et al. 2023) were plotted. These natural melts are interpreted as a result of anatexis of metapelite at UHP conditions, that subsequently migrated from their source lithologies, and were trapped as melt inclusions during garnet growth in UHP eclogite. The comparison is shown in Fig. 7.3 and Fig. 7.4.

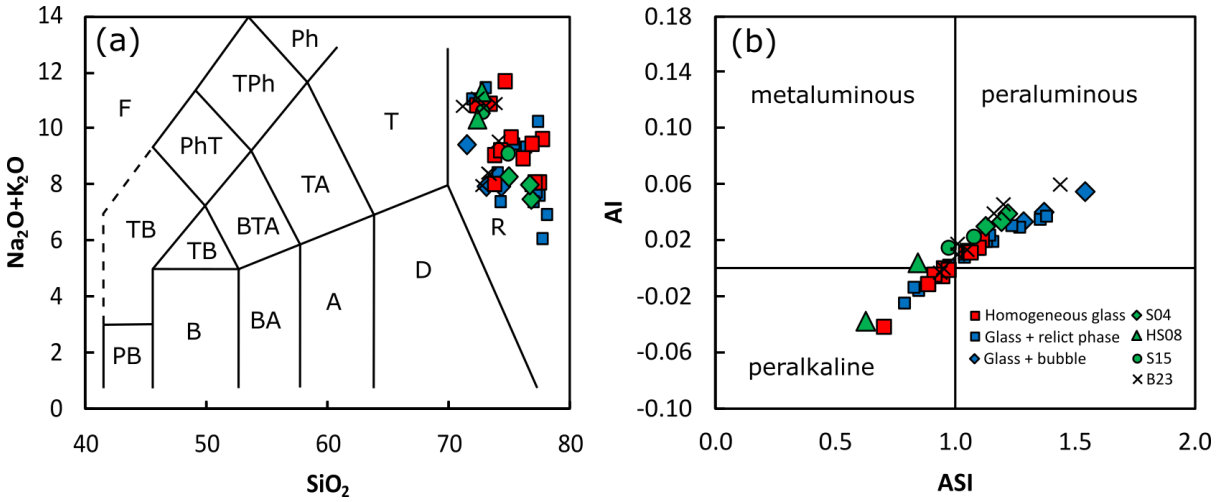

Figure 7.3 Chemical classification of remelted NG from this study, of experimentally produced melts and of other melt inclusions in UHP metapelites from the literature (normalized to 100% on anhydrous basis). **(a)** – TAS diagram after Le Maitre et al. (2002), plotted in wt%. Abbreviations: R – rhyolite, D – dacite, A – andesite, BA – basaltic andesite, B – basalt, PB – picrobasalt, T – trachyte, TA – trachy-andesite, BTA – basaltic trachy-andesite, TB – trachy-basalt, Ph – phonolite, TPh – tephri-phonolite, PhT – phono-tephrite, TB – tephrite, basanite, F – foidite, **(b)** – alkalinity index (AI = molar Al_2O_3 – (K_2O+Na_2O)) versus aluminum saturation index (ASI = molar Al_2O_3/(CaO+K_2O+Na_2O)). Red squares: homogenous glass, blue squares: glass with minor presence of relict phases (Qz, Ms), blue diamonds: homogenous glass with bubble, green symbols: experimentally produced UHP melts from the literature (diamonds **S04** from Schmidt et al. 2004; triangles **HS08** from Hermann and Spandler 2008; circles **S15** from Schmidt 2015); black crosses **B23** natural UHP melts produced by metapelite and trapped in UHP eclogite (Borghini et al. 2023)

Natural anatectic melts of this study contain from 10 to 14 wt% Al_2O_3 (Fig. 7.4a). They are slightly shifted towards lower Al_2O_3 and higher SiO_2 with respect to experimental UHP melts and melts from MI trapped in UHP eclogite. They also contain much lower concentrations of CaO (< 0.5 wt%) (Fig 7.4b). Contents of alkalis range from <1 to 6 wt% for Na_2O and from 3 to 9 wt% for K_2O (Fig 7.4c, d). This variability is

also observed in experimental UHP melts and MI from UHP eclogite. Contents of $FeO+MgO+TiO_2$ are significantly higher (2 - 5 wt%), than those of UHP melts produced in experiments and MI in eclogite (Fig.7.4e). The K_2O/Na_2O ratio is from 0.84 up to 3.22 (2.4 in average), with one exception of 8.8 (Fig. 7.4f) and displays similar variability as in the compared UHP melts.

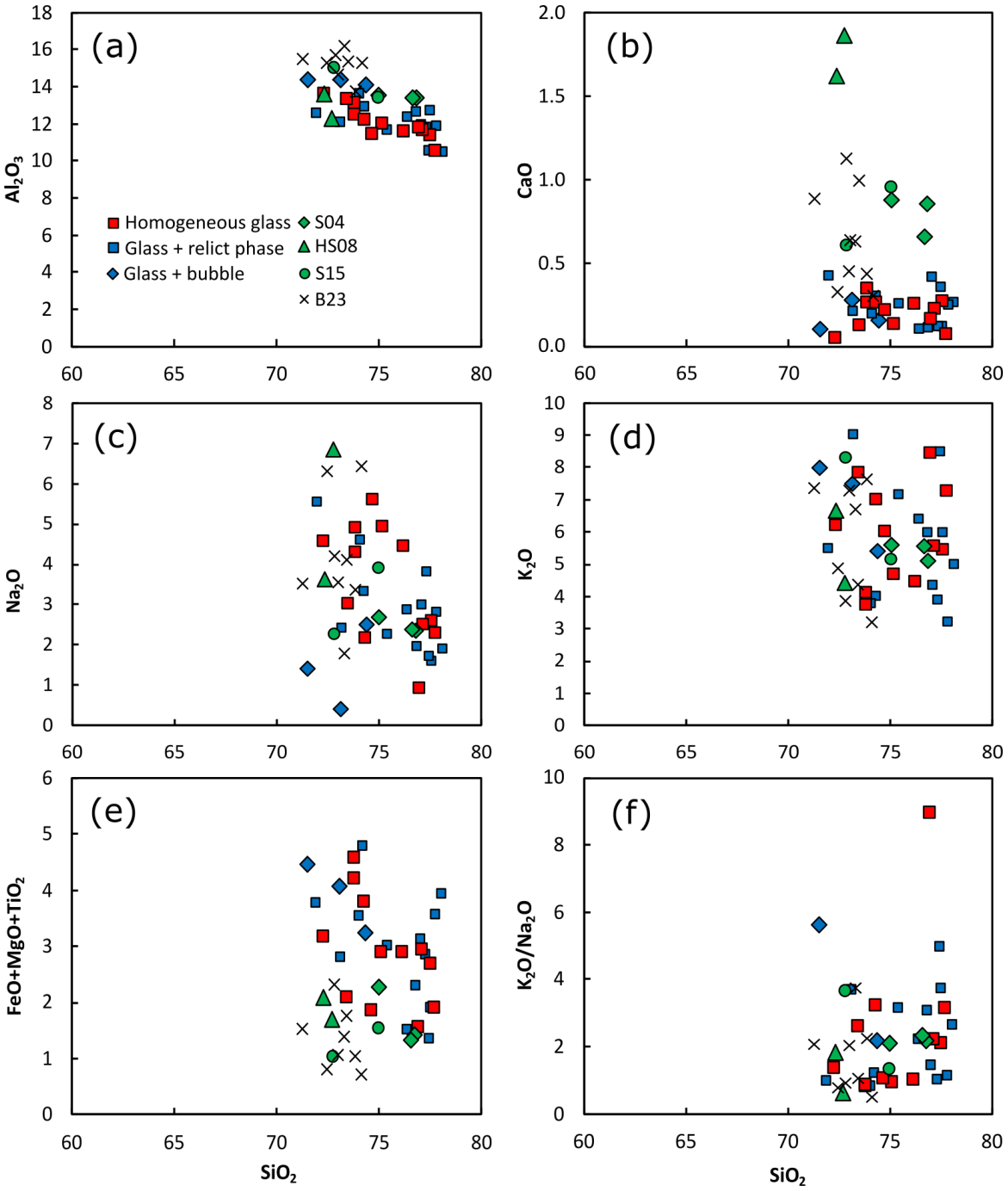

Figure 7.4 Chemical composition of glasses from experimentally remelted nanogranitoids from Åreskutan and experimentally produced UHP melts. Normalized on anhydrous basis, plotted in wt%. Symbols as in Figure 7.3.

7.4 Volatile content of remelted nanogranitoids

NanoSIMS analysis of remelted NG allowed the quantification of the volatile component dissolved in melt. In total, 70 glassy inclusions were measured. Careful

examination and cross-comparison of data allow to reject analyses considered unreliable. After this procedure, 23 analyses of glass were selected (Tab. 7).

Table 5.3 Volatile contents of re-homogenized NG determined by NanoSIMS. Analyses marked with asterisk were disregarded from interpretation of CO_2 concentrations in melt.

No. analysis	P (GPa)	T (˚C)	Size (μm)	Homogeneity	H_2O (wt%)	1σ error	CO_2 (ppm)	1σ error
1B_ROI1_03[a]	4	850	>10	homogenous	4.58	0.02	7158	126
1B_ROI2_05[b]	4	850	>10	homogenous	6.85	0.03	1152	58
1B_ROI2_06	4	850	>10	homogenous	4.24	0.02	7472	160
1B_ROI2_07	4	850	<10	homogenous	4.78	0.02	1178	45
1B_ROI4_08	4	850	10	glass, bubble	4.38	0.03	11504	220
1B_ROI1_11	4	850	10	glass, mica	6.25	0.02	2255	53
1B_ROI1_12	4	850	10	homogenous	3.78	0.02	10366	209
1A_ROI1_4	4	850	<10	homogenous	3.75	0.02	12843	198
1A_ROI1_6*	4	850	<10	glass, bubble	5.53	0.03	29399	387
1A_ROI1_7*	4	850	<10	glass, bubble	3.95	0.02	66176	763
1A_ROI1_8	4	850	<10	glass, bubble	5.22	0.02	19289	262
1A_ROI1_9*	4	850	10	glass, graphite	3.88	0.02	61626	705
1A_ROI1_10*	4	850	<10	glass, bubble	4.56	0.02	51516	594
1A_ROI2_13	4	850	<10	homogenous	4.83	0.02	4945	106
7A_ROI1_1	4.5	900	>10	homogenous	4.96	0.02	20932	273
7A_ROI5_6*	4.5	900	>10	homogenous	3.50	0.02	34328	470
7A_ROI3_7	4.5	900	>10	homogenous	3.65	0.02	3291	89
7B_ROI1_1	4.5	900	10	glass, quartz	5.89	0.02	21058	272
6A_ROI3_4	4.5	900	<10	homogenous	4.47	0.02	5526	113
6A_ROI3_6	4.5	900	<10	homogenous	3.31	0.02	2518	66
6A_ROI3_7	4.5	900	<10	homogenous	4.60	0.02	14992	224
4_ROI1_1*	4.5	900	10	glass, mica	3.84	0.02	45323	562
4_ROI1_2	4.5	900	10	glass, mica	5.14	0.02	2404	72
4_ROI1_4	4.5	900	<10	homogenous	4.58	0.02	7158	126
Average					4.61		8758	

a – chemical composition in Tab. 5 (n. anal. 5), b – chemical composition in Tab. 5 (n. anal. 6a)

The analysed melts contain 4.6 wt% of H_2O in average, ranging from 3.3 to 6.6 wt% (Fig. 7.5a). These H_2O concentrations are similar to the contents measured in MI trapped in UHP eclogite reported by Borghini et al. (2023), (4 wt% in average, ranging from 3.42 to 5.23 wt%) The CO_2 concentrations display a wide range, from 0.12 to 6.63 wt%, with most analyses clustering at < 2 wt%. Few analyses showing CO_2 concentrations between 3.4 and 6.6 wt% form a second cluster (Fig. 7.5b).

The maximum CO_2 solubility in rhyolitic melts was calculated for the P-T conditions at which NG were remelted, in order to verify the reliability of the higher

CO_2 concentrations detected in glasses (> 2 wt%). The CO_2 solubility values (lines NK13, DD14 and M20 in Fig. 7.5b) were calculated for rhyolitic melts based on previous works (Ni and Keppler, 2013; Duncan and Dasgupta, 2014; Muth et al., 2020). Line NK13 was calculated using the experimentally calibrated relationship between C (CO_2 solubility) and P (pressure), quantified as: 0.57 ppm CO_2/bar, and valid up to 4 GPa (Ni and Keppler, 2013). Line DD14 was calculated applying formula (3) by Duncan and Dasgupta, (2014) experimentally constrained within 1.5 – 3 GPa,

$$CO_2\,(wt\%) = (-0.01108\,H_2O + 0.03969)P^2 + (0.10328\,H_2O + 0.41165)P \quad (3)$$

where H_2O is in wt% and P in GPa. Line M20 was calculated according to formula (4) by Muth et al. (2020), where composition of the melt, pressure, temperature and H_2O content are considered. The calibration for this model was done at 1.5 – 3 GPa,

$$CO_2\,(wt\%) = (a_1 Na\# + a_2 X_{H2O} + a_3)P^2 + (b_1 T + b_2 X_{H2O} + b_3)P \quad (4)$$

where $Na\# = {}_{molar}\, Na_2O/(Na_2O+K_2O)$, P in GPa, T in ˚C, X_{H2O} is the molar fraction of H_2O in the melt. The constants are as follow: $a1 = 2.16\times10^{-1}$, $a2 = -4.07\times10^{-1}$, $a3 = -2.8\times10^{-1}$, $b_1 = -5.6\times10^{-4}$, $b_2 = 3.7\times10^{0}$, $b_3 = 9.9\times10^{-1}$. It is important to notice that calculated CO_2 solubility lines are extrapolation to 4 and 4.5 GPa. The currently available models are not well calibrated for pressures exceeding 4 GPa. Therefore, I decided to use the 3 above mentioned equations as the best available?? approximation of actual CO_2 solubilities for rhyolitic melts at UHP conditions. Considering calculated CO_2 solubilities, analyses clustering above 3 wt % of CO_2 are considered less reliable, therefore they are disregarded from further interpretation. Excluding those values, the average CO_2 concentration dissolved in melts is 0.88 wt%, ranging from 0.12 to 2.11 wt% These concentrations are lower, than CO_2 contents from MI in eclogite (2 wt% in average, ranging from 1.51 to 2.89 wt%) after gas bubble reintegration reported by Borghini et al. (2023).

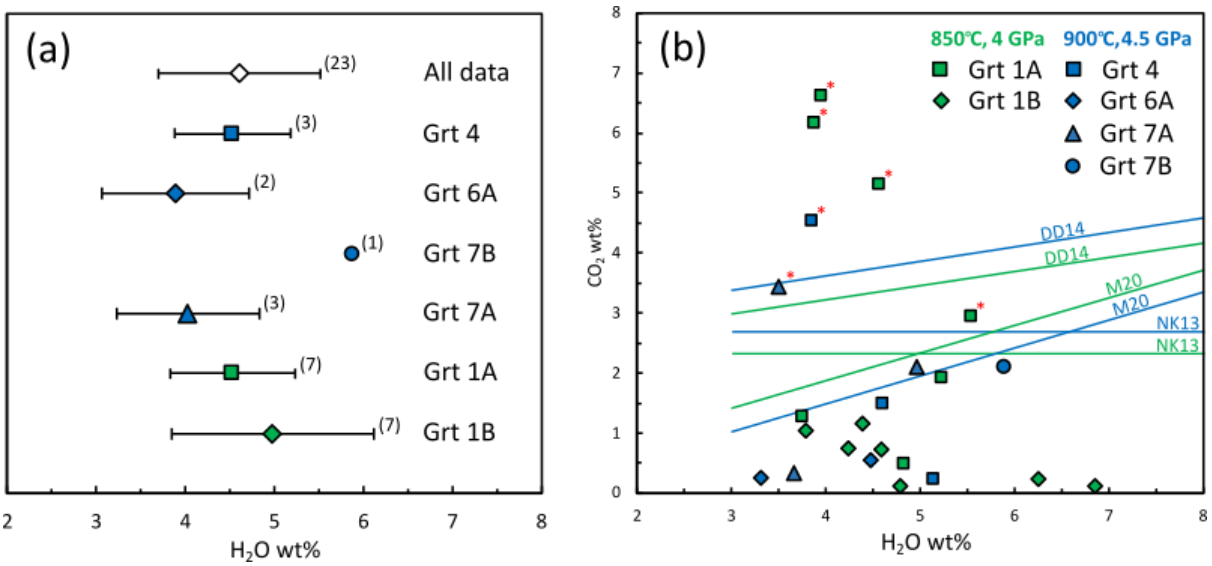

Figure 7.5 (a) – H_2O concentration of remelted NG from 6 garnet crystals measured by NanoSIMS. White diamond represents the average of all analysed inclusions. Horizontal bars are one standard deviation on average values. The number of analyses is written in parenthesis next to horizontal bars. Green and blue colour represent analyses from experiments conducted at 850˚C, 4 GPa, and 900˚C, 4.5 GPa, respectively. **(b)** – H_2O and CO_2 measured in remelted NG; solid lines indicate maximum CO_2 solubility calculated for rhyolitic melts at 850˚C, 4 GPa (green) and 900˚C, 4.5 GPa (blue) **NK13** – Ni and Keppler (2013), **DD14** – calculated for Na#=0.71, Duncan and Dasgupta (2014), **M20** – Muth et al. (2020). Analyses marked with red star are disregarded from further interpretation and discussion of CO_2 in natural melts.

Chapter VIII

Discussion

8.1 Composition of UHP melts

Crystalized droplets of melt are commonly found in UHP rocks and are often called multiphase solid inclusions (MSI) (Stöckhert et al., 2009; Gao et al., 2012; Chen et al., 2014; Stepanov et al., 2016; Liu et al., 2018) even though some authors propose an origin from supercritical silicate-rich aqueous fluids (Ferrando et al., 2005; Malaspina et al., 2006, 2009). Despite an inferred similar origin, most of MSIs differ substantially from NGs in terms of microstructure and mineral composition.MSI do not usually do not display negative crystal shape of host mineral in contrast to NGs. Mineral assemblage of MSI usually comprise more phases than assemblage of NGs, A recent study of Borghini et al. (2023) documented the first occurrence of NGs coexisting with melt inclusions (MI) in a UHP eclogite from Saidenbach in the Bohemian Massif. The present work adds and discusses another case of re-homogenized NGs coexisting with diamonds from paragneisses, i.e., the SNC in the Scandinavian Caledonides.

NGs are the result of entrapment of anatectic melt in a peritectic host phase, and of its subsequent crystallization upon cooling (See Chapter I). However, there are other processes proposed in the literature that may lead to the formation of mineral aggregates in inclusions similar to NGs, and that must be considered: 1) entrapment of mineral aggregates without melt during porphyroblast growth, 2) entrapment of melt together with crystals (Acosta-Vigil et al., 2016), 3) entrapment of mineral inclusions during the prograde metamorphism and later decomposition to melt or aggregates of mineral (Perchuk et al., 2005). Several features indicate that the above processes are not applicable to the case study reported here, and that the compositions of glasses derived from remelted NGs are indeed trapped primary UHP melts; 1) the investigated NGs display the typical microstructural features associated with entrapment and crystallization of melt inclusions described in the literature, e.g. negative crystal shape, simple and consistent mineral assemblage Qtz + Pl + Kfs +

Ms/Bt, (Ferrero et al., 2012; Bartoli et al., 2013; Cesare et al., 2015), 2) NGs have been successfully re-homogenized to a single melt phase at inferred conditions of entrapment. Thus, these observations allow to conclude that these NGs indeed originated from entrapped anatectic melts.

Homogenization of inclusions by experimental heating under confining pressure could result in a modification of the primary composition of trapped melt. Indeed, portion of melt produced by the matrix surrounding the garnet crystal loaded into the experimental capsule can penetrate along fractures, resulting in meaningless compositions of remelted NGs (Kamenetsky and Danyushevsky, 2005). Careful examination of features in remelted NGs from Åreskutan paragneisses were conducted to avoid this potential issue. In the experimental runs at 850˚C and 900˚C matrix melt has not been observed. Therefore, the possibility of contamination of remelted NG by matrix melt was ruled out (Chapter XVII, Tab. 4).

Another possibility of altering NG composition, described by Stepanov et al. (2016), is the interaction of melt with host garnet during the experiment. In this study, such interaction was observed in some inclusions containing melt with other phases (see Chapter XVII, Fig. XX) and thus these analyses were disregarded. However, in order to validate and quantify the possible occurrence of garnet dissolution and contamination of original melts during the experiment, the correction proposed by Stepanov et al. (2016) was applied. This correction is based on the assumption that the maximum FeO concentration in UHP melts should approach the values obtained in the experiments of Hermann and Spandler (2008). For experimentally derived solubilities of all elements in UHP melts see also Hermann et al., (2013). The correction for garnet-melt interactions is expressed as (Stepanov et al., 2016):

$$x = \frac{C_{measured} - C_{Grt}}{C_{inclusion} - C_{Grt}}, \quad (5)$$

where, the **x** value is the proportion of the original melt in the inclusion, $\mathbf{C_{measured}}$ is the FeO content measured in the inclusion, and $\mathbf{C_{Grt}}$ is the FeO content of garnet, $\mathbf{C_{inclusion}}$ is the assumed value of FeO in UHP melts from experimental studies (Hermann and

Spandler, 2008). With the calculated **x** value, all concentrations of other elements are corrected according to the formula:

$$C_{inclusion} = \frac{C_{measured} - C_{Grt}(1-x)}{x} \quad (6)$$

These calculations have been done for homogenous glasses (Chapter XVII, Tab. 4) under the assumption of 0.94 wt% of FeO (FeO content in melt formed at 900˚C, 4.5 GPa reported by Hermann and Spandler, (2008) and considering the composition of the garnet in proximity of NGs. The result of this calculation (formula 5) provides the estimated percentage of theoretical garnet component dissolved in the glass, which, in the case of NGs investigated in this study, ranges from 1 to 10% (avg. 5%). This theoretical contribution of garnet is significantly lower than the values reported by Stepanov et al. (2016), from 10 – 25% of garnet component in the glass. Subsequent correction of the other elements (formula 6) results in unrealistic values of SiO_2 (~80% wt%). Therefore, we conclude that the compositions of homogenous glasses were not contaminated by garnet during the experiment at 850 - 900°C and that the FeO concentrations reflect the original contents of these melts.

The same correction (formula 5) was applied to previously rejected glasses with visible interaction between garnet and melt, but with the assumption of average FeO content measured in homogenous glasses (FeO = 2.39 wt%). The calculated portion of dissolved garnet ranges from 10 to 23% with average 16%, similarly to glasses corrected by Stepanov et al., (2016). The concentrations of other elements were subsequently corrected and display contents comparable with homogenous glasses. Thus, in case of previously rejected glasses with visible garnet-melt interaction this correction was successfully applied.

The UHP melts derived from re-homogenized NGs from Åreskutan are rhyolitic (avg. SiO_2 = 75.25 wt%), with high alkali content (avg. K_2O+Na_2O = 9.44 wt%). They are peralkaline to peraluminous with avg. ASI = 0.98, AI = -0.001. These melts contain low CaO (< 0.5 wt%) and high FeO concentrations (avg. 2.39 wt%). The K_2O/Na_2O ratio is high (avg. = 2.36), as expected for UHP melts with low volatile content and in presence

of CO_2 (see section 8.2) (Schmidt, 2015). The relative compositional uniformity of UHP melts was attributed to equilibrium between melt and the residuum (Schmidt, 2015).

The compositions of UHP melts retrieved from NGs in this work are compared with compositions of experimentally produced UHP melts from metapelitic material (Schmidt et al., 2004; Hermann and Spandler, 2008; Schmidt, 2015) and MIs (with one re-homogenized NG) from UHP eclogite of Bohemian Massif (Borghini et al., 2023) (Fig. 1). In addition, composition of UHP melts from Åreskutan are also compared with remelted Dia-bearing NGs from felsic granulites of the Bohemian Massif, and other re-homogenized NGs trapped at lower pressure conditions (< 2GPa) from several studies (Fig. 8.1).

Generally, the chemical composition of natural UHP melts from Åreskutan paragneiss overlaps with experimentally produced UHP melts (Fig. (Schmidt et al., 2004; Hermann and Spandler, 2008; Schmidt, 2015) and MIs and re-homogenised NG from UHP eclogite (Borghini et al., 2023) in terms of SiO_2, Al_2O_3, Na_2O, K_2O and K_2O/Na_2O ratio (Fig. 7.4). However, two components display significant differences: the concentration of CaO in experimental UHP melts is significantly higher (>0.5 wt%), than in natural UHP melts from Åreskutan (<0.5 wt%). In comparison with MI from eclogite, Åreskutan melts show more restricted and generally lower contents of CaO. This discrepancy might be a result of compositional differences in protolith or an indication that in general melting experiments may not reproduce the entire compositional range of melts formed in nature.

The most striking difference observed refers to the concentration of FeO. The UHP melts from Åreskutan contain in average 2.39 wt% of FeO (ranging from 1.2 wt% to 5 wt%) while MI from eclogite contain <2 wt%. The experimental UHP melts contain even less FeO (<1 wt%). One possible explanation of such high FeO concentration might be post-entrapment diffusion/interaction between MIs/NGs with garnet. However, textural features (e.g., negative crystal shape) of NGs suggest their preservation (see above). Therefore, most likely the high FeO content is an intrinsic feature of UHP melts from Åreskutan related to the composition of the photolith.

Moreover, Dia-bearing NGs from Saidebach (Stöckhert et al., 2009) re-melted at 975 - 1100 ˚C and 2.5-4.5 GPa show slightly lower but comparable contents of FeO+MgO (2 wt%, 2.8 wt% for glass from Åreskutan) (Acosta-vigil et al., 2017). The content of FeO+MgO from remelted Åreskutan NGs is also consistent with previous studies of inclusions in partially molten rocks at lower pressures (< 2 GPa) (see Fig. 8.1). Regardless of pressure, NGs from Åreskutan fall into a linear trend defined by FeO+MgO vs. temperature. That would suggest that in case of re-homogenized NGs the main factors controlling FeO concentration in partial melts are the protolith bulk composition and the melting temperature. The discrepancy observed in FeO content between natural UHP melts from Åreskutan and experimentally produced melts might be explained by alloying effect of Fe. Experimentally produced melts could lose some of its original FeO contents due to alloying with the capsule, following the reaction (Balta et al., 2011):

$$FeO_{melt} \leftrightarrow Fe_{alloy} + 0.5O_2 \quad (1)$$

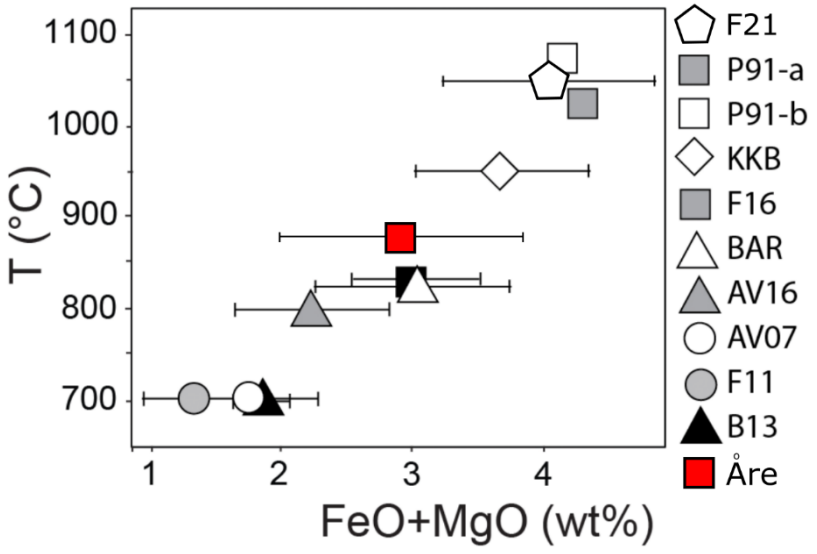

Figure 8.1 FeO+MgO vs. temperature diagram comparing remelted NGs compositions from this study (**Åre**) with previous studies of melt inclusions in partially melted rocks from metasedimentary protolith. Modified after Ferrero et al. (2021). Black bars represent 2 standard deviations. Abbreviations: Central Maine Terrane (**F21**) from Ferrero et al. (2021), Karela Khondalite Belt (**KKB**) and Braun gneiss (**BAR**) from Ferrero et al. (2012), Oberpflatz migmatites (**F16**) from Ferrero et al. (2016), Jubrique migmatites (**AV16**) from Acosta-Vigil et al. (2016), Grt+Bt granulitic enclaves of El Hoyazo (**AV07**) from Acosta-Vigil et al. (2007), Spl+Crd granulitic enclaves of El Hoyazo (**F11**) from Ferrero et al. (2011), Sierra Alpujata metatexites (**B13**) from (Bartoli et al., 2013b), experimental melts (**P91a,b**) from Patiño Douce and Johnston, (1991).

8.2 Volatiles in UHP melts

The droplets of melt trapped in the garnet and crystallized as NGs, may preserve the volatile content of the melt at the moment of entrapment (Bartoli et al., 2014; Nicoli and Ferrero, 2021). Through the re-homogenization of NGs minerals are melted and volatiles are redissolved into the melt, therefore allowing the recovery of the original H_2O and CO_2 concentrations of the melt by NanoSIMS analysis in situ (Bartoli et al., 2014; Rasmussen et al., 2020).

The concentration of H_2O in the UHP melt from Åreskutan is relatively low (avg. 4.6 wt%), especially when compared to experimentally derived predictions of H_2O contents in melts at 900˚C, 4 – 4.5 GPa (~14 wt%), in the CO_2-free haplogranitic system constrained by Hermann and Spandler, (2008), and refined by Hermann et al., (2013) (see Fig. 8.3a). However, the range of H_2O concentrations in natural melts measured in MI and re-homogenized NG from UHP eclogite (Borghini et al., 2023) is almost identical to the contents obtained in this study (see Fig. 8.2). Similar contents of H_2O are also observed in other natural melts formed at lower pressure (in mid- to lower crust, Fig. 8.2), and pose doubts on the applicability to natural rocks of solubilities determined in synthetic simplified systems. These low concentrations might be a result of continuous dehydration melting of phengite that was source of H_2O in H_2O-undersaturated system.

The speciation of carbonic volatile species in a rhyolitic melt is dominated by the two species molecular CO_2 and CO_3^{2-}. The dissolution reactions are (Duncan and Dasgupta, 2014):

$$CO_{2\ vapour} \leftrightarrow CO_{2\ melt} \quad (2)$$

$$CO_{2\ vapour} + O_{2\ melt} \leftrightarrow CO_3^{2-}{}_{melt} \quad (3)$$

Experiments of Duncan and Dasgupta (2014) have demonstrated that, at lower pressures conditions (~1.5 GPa) and H_2O-poor systems (~0.5 wt%), the dominant species is molecular CO_2. The presence of carbonate species (CO_3^{2-}) is increasing with

pressure and H_2O concentration. At the studied conditions of 4 - 4.5 GPa and with the measured H_2O contents (avg. 4.6 wt%) in the melt, the major carbonic species should be carbonate, with marginal content of molar CO_2. We could not verify the speciation of carbonic species in the remelted NGs, as their size is too small for such determination.

The content of CO_2 in UHP melts from Åreskutan is high (avg. = 0.88 wt%) and is ranging from 0.12 to 2.11 wt%. The variability of CO_2 contents might be a result of degassing and loss of CO_2 that may have occurred during the experiment. Bubbles have been observed in the glass of remelted NGs (Fig. 7.1e, Tab. 7.3). Nevertheless, the CO_2 concentrations in UHP melts from Åreskutan are similar to the contents retrieved from MIs and remelted NG from UHP eclogite (ranging 1.6 – 2.9 wt%, Fig. 8.2) by Borghini et al. (2023). In comparison to CO_2 contents of melt inclusions from rocks of mid- and lower crust (Ivera Zone, Gruf Complex, and CMT) the UHP melts from Åreskutan paragneiss and Saidenbach eclogite contain much higher concentrations of CO_2. Thus, it is notable that the content of crustal carbon dissolved in melts decreases with pressure i.e., depth.

The organic carbon transformed to graphite during the high-grade metamorphism is the main source of CO_2 in metasedimentary non carbonatic rocks (Tumiati et al., 2022). Graphite is present in Åreskutan paragneiss as flakes in the rock matrix and as inclusions in the garnet (See Chapter IV). There are two possible decomposition reactions that can liberate CO_2: Fe^{3+} reduction during the biotite melting, that forms CO_2 and Fe^{2+} that is incorporated in the minerals (e.g., garnet) during the metamorphic reactions (Cesare et al., 2005):

$$2Fe_2O_3^{(Bt)} + C^{(Gr)} \rightarrow 4FeO^{(Crd,Grt,Ilm,Opx)} + CO_2^{(fluid,melt,Crd)} \quad (4)$$

or H_2O-present redox reaction of graphite that produces CO_2 and CH_4 (Connolly and Cesare, 1993)

$$2C + 2H_2O \rightarrow CO_2^{(fluid,melt)} + CH_4^{(fluid)} \quad (5)$$

In the case of Åreskutan paragneisses, melting most likely occurred at UHP conditions (NGs coexisting with diamonds, Fig. 6.4b), therefore biotite would not be present in the rock. Moreover, CH_4 was detected in residual fluid in MPIs (see Fig.6.6g). These observations allow to conclude that the carbonic species in the melt and in the immiscible fluid are those of a CO-O-H fluid in equilibrium with graphite, where the H_2O component probably derived from decomposition of phengite. Such fluid would contain H_2O, CO_2 and CH_4 as predicted by Connolly and Cesare (1993).

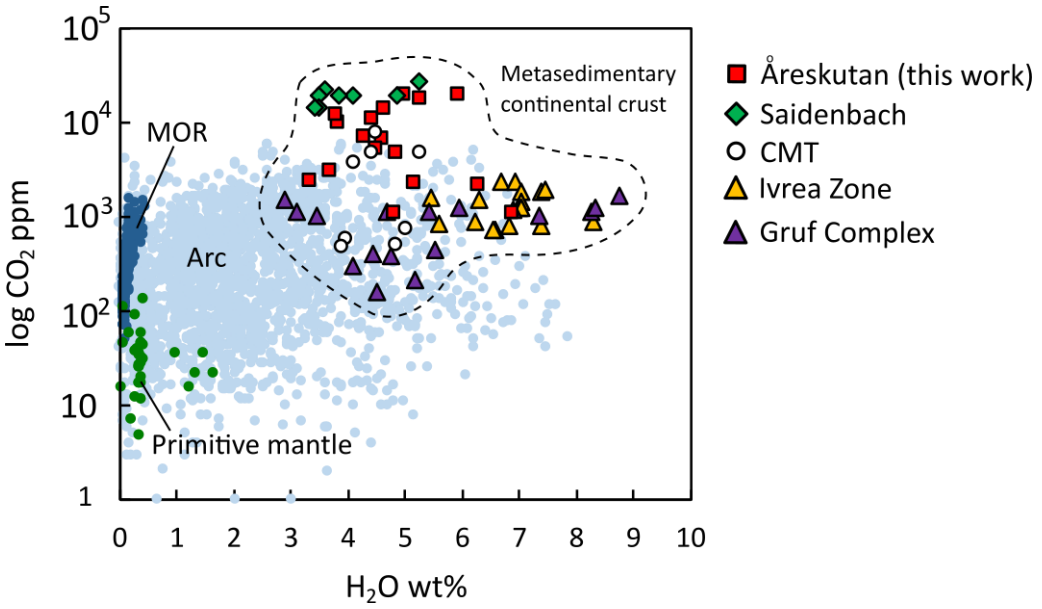

Figure 8.2 H_2O vs. CO_2 content of re-homogenized NGs from **Åreskutan** compared with glassy inclusions and re-homogenized NG from eclogite of **Saidenbach**. Analyses marked with asterisk indicate the same glassy inclusions before reintegration of CO_2 present in the vapour bubble (Borghini et al., 2023). In addition, volatile content of MI from lower continental crustal rocks was plotted; Central Meine Terrane (**CMT**) (Ferrero et al., 2021), **Ivrea Zone** (Carvalho et al., 2019), **Gruf Complex** (Gianola et al., 2021). Primitive mantle, mid-oceanic ridges (MOR), and arc volcanoes are taken from Nicoli and Ferrero (2021). The dashed line indicates composition of melt from the metasedimentary continental crust. Diagram modified after Borghini et al. (2023).

8.3 Record of UHP fluid

The record of former presence of fluids in the rock is often preserved as fluid inclusions (FI) (Bodnar and Frezzotti, 2020). Droplets of fluid are trapped as primary inclusions in minerals during their growth (e.g., garnet). The FI may then crystallize upon cooling producing the so-called daughter crystals. When crystallization occurs by simultaneous involvement of the host, the crystallized phases are called *stepdaughters*. For example, the multiphase inclusion (MPI) in garnet from Åreskutan are made of stepdaughter minerals. Very often the MPI contain a residual fluid, as the crystallization of (step)daughter minerals cannot fill the entire cavity. A series of retrograde reactions between COH-fluid inclusions and garnet host was proposed to explain the minerals observed within MPIs(Carvalho et al., 2020). This process involves dissolution of garnet and precipitation of new phases – including carbonates and hydroxylated minerals - consuming part the of trapped fluid. Despite the final volume of the inclusion is reduced, fluid consumption leads to a net decrease of the fluid density in within inclusion. Recent studies of Tacchetto et al. (2019) and Carvalho et al. (2020) revealed textural features and mineral composition of MPIs. The proposed reaction identified by Tacchetto et al. (2019) is:

garnet + CO_2 = carbonate + corundum + quartz (6)

In the presence of H_2O in the fluid, additional reactions may occur forming hydrated phases. These fluid consuming reactions were identify through thermodynamic modelling and detailed examination of mineral assemblages in MPIs conducted by Carvalho et al. (2020):

corundum + quartz + H_2O = pyrophyllite (7)

pyrophyllite + corundum + H_2O = kaolinite (8)

The investigation of inclusions in garnet of Åreskutan paragneiss shows that the MPIs are coexisting with NGs. The MPI are composed of solids, mainly: carbonates + pyrophyllite + quartz + phlogopite ± graphite ± diamond ± sulphate, and residual fluid (CO_2 + CH_4 + N_2) (for the details see Chapter VI).

The MPIs from Åreskutan paragneiss are compared with MPIs from Athabasca granulite (Tacchetto et al., 2019), Gruf Complex (Carvalho et al., 2020; Gianola et al., 2021) and Ivrea Zone (Carvalho et al., 2019, 2020). The comparison of MPI mineral assemblages is shown in Tab. 8.1.

Table 8.1 Comparison of mineral assemblages of MPIs from different localities. For the references see text above.

MPI Locality / Mineral	Cal	Mgs	Sid	Dol	Qz	Prl	Kaol	Crn	Ms	Bt	Gr	Dia	Zn-Spl	Fe-S	Sulphate
Åreskutan paragneiss	x	x	x	x	x	x	x			x	x	x			x
Ivrea Zone migmatite	x	x	x		x	x	x				x				
Gruf Complex granulite	x	x	x		x	x		x	x	x				x	
Athabasca granulite	x	x		x	x	x		x			x		x		

The MPIs from Åreskutan contain almost all phases observed in the other localities supporting the process of stepdaughter formation of the mineral assemblage in the polycrystalline inclusions. One of the important observations done in MPIs from Åreskutan is the absence of corundum, similarly to MPIs from Ivrea Zone. Considering reactants and products of fluid-consuming reactions, it is possible that corundum was consumed entirely (reaction 8) and formed more stable phases (pyrophyllite). There is also a possibility that corundum did not precipitate at all, and thus had never been present in MPIs from Åreskutan.

The presence of biotite suggests that MPIs from Åreskutan contain melt component i.e., mixed inclusions, as observed in melt inclusions in crustal xenoliths from the Neogene Volcanic Province of SE Spain (e.g., Cesare et al., 2007). Mixed inclusions may also contain feldspars (Fig. 6.8). Mixed inclusions are formed by entrapment of immiscible fluid and melt within one inclusion, melt provide e.g.,

potassium to form micas or feldspars. The same process of heterogeneous trapping can be observed in MPIs from Gruf Complex, however not to such high degree (absence of feldspars). Some MPIs from Åreskutan contain sulphides and vaterite in contrast to other former fluid inclusions. Vaterite is the metastable polymorph of $CaCO_3$ that can be stabilised by the presence of SO_4^{2-} in the system (Fernández-Díaz et al., 2010). The presence of diamond in one MPI from Åreskutan (see Chapter VI) indicates pressure conditions of primary fluid entrapment. CO_2 was often detected by Raman spectroscopy and the intensity of characteristic Fermi diad allowed to estimate the density of residual fluid in few inclusions (Chapter VI). Calculated densities are variable (0.25 – 1.02 g/cm^3), from values corresponding to vapor (0.25 g/cm^3) measured in bigger MPIs (∼10 μm) to higher densities typical of FI formed at high-pressure conditions (1.02 g/cm^3) measured in smaller MPIs (∼3 μm). The variability of CO_2 density can be explained by the degree of fluid-consuming reactions that have occurred (Carvalho et al. 2020). In bigger MPIs more fluid was consumed that resulted in lower density in comparison to smaller MPIs that preserved more intact fluid.

The investigation carried out on MPIs from Åreskutan, combined with identification of their mineral assemblages and detection the residual fluids, has allowed to reconstruct qualitatively the primary composition of UHP fluids trapped in these inclusions. We infer that this UHP fluid was composed of $CO_2 + H_2O + CH_4 + N_2 \pm SO_4$, and that it was present together with the melt. The occurrence of MPIs and NGs in the same inclusion cluster is strong textural evidence for immiscibility of melt and fluid phases at UHP conditions. The compositional spectrum of mixed inclusions represents different proportions of entrapped immiscible COH-fluid and silicate melt within one inclusion. Therefore, the origin of carbonic species trapped in NGs and MPIs is the same i.e., fluid equilibration in the presence of graphite as described in paragraph 8.2.

The simultaneous entrapment of two immiscible phases - melt and fluid - indicates that entrapment occurred below second critical endpoint (SCP). Above that

point complete fluid/melt miscibility would be expected i.e., formation of a supercritical phase. Experimental studies of Hermann and Green (2001), Hermann et al. (2006, 2013), and Hermann and Spandler (2008) have constrained the second critical endpoint at 3.7 GPa and c. 750 °C in the CO_2-free H2O-haplogranite system (Fig. 8.3a). However, the presence of diamond, contents of volatiles and immiscibility of two phases present in the rock suggests that this model cannot be applied for MPIs and NGs from Åreskutan. A more representative system that includes most of the possible combinations of H_2O and CO_2 as volatiles was proposed by Schmidt (2015) (Fig. 8.3b). Their SCP, located at 5.5 GPa, is at greater pressure than those estimated for formation and entrapment of NGs and MPIs from Åreskutan. These experimental constrains are consistent with observations from paragneiss at Åreskutan made in this thesis and support the conclusion that silicate melt, and a COH-fluid can be immiscible at 850 - 900˚C, 4 – 4.5 GPa.

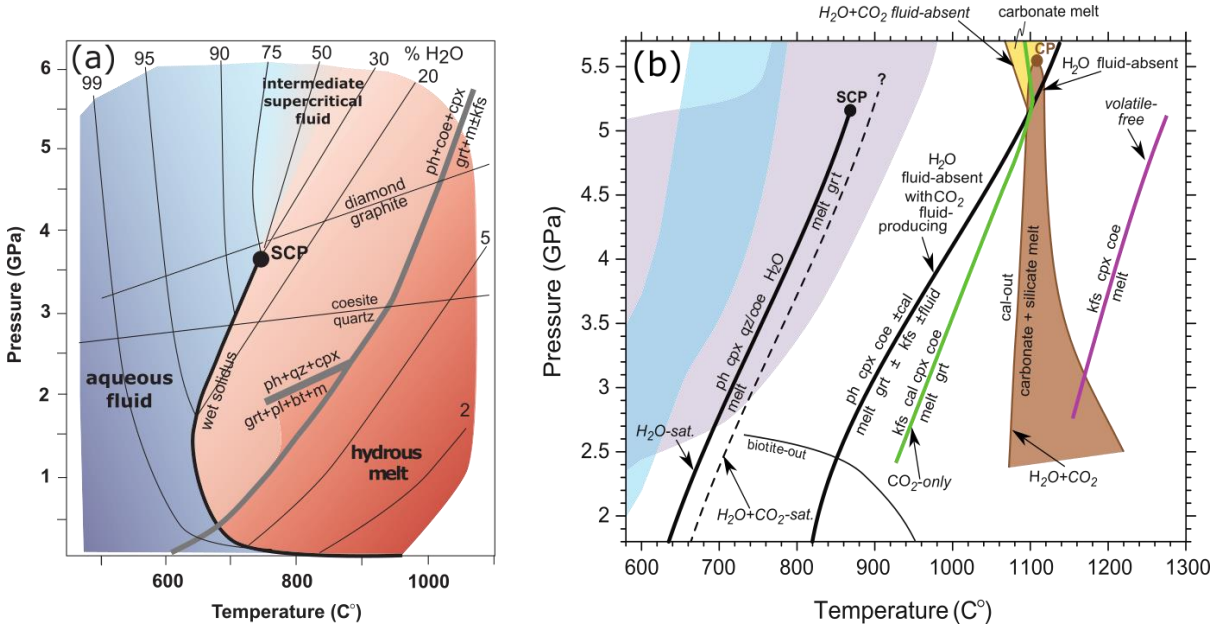

Figure 8.3 (a) – Pressure-temperature diagram modified after Hermann et al. (2013) of metapelites and granitic rocks in the presence of H_2O. The wet solidus terminates at the second critical endpoint (SCP). The fine black lines show the wt% of H_2O in the fluid and melt phase. The grey lines mark melting reactions (Schmidt et al., 2004; Auzanneau et al., 2006; Hermann and Spandler, 2008) that consume phengite. **(b)** – P-T-locations of solidi of metasediments for all combinations of H_2O and CO_2, modified after Schmidt, (2015), all references therein. The H_2O-saturated solidus (wet solidus) is compiled by Mann and Schmidt (2015), Schmidt (2015). The wet melting reaction (Ph + Cpx + Qz + H_2O = melt) changes at ~4 GPa from eutectic to peritectic (+ grt) end terminates at critical endpoint near 5 GPa

----------Continue to the next page

The H_2O+CO_2 saturated solidus is determined at 3 GPa where it locates ~30˚C higher than wet solidus. The presence and position of critical point remains unknow. The fluid-absent solidus is compiled by Mann and Schmidt (2015), Schmidt (2015). The melting of subsolidus assemblages in fluid-absent system occurs as reaction Ph + Cpx + Coe = melt + Grt ± Kfs ± fluid and appears to not vary in temperature with or without of CO_2. This solidus is truly fluid-absent with H_2O as the only volatile but with H_2O + CO_2, fluid-absent subsolidus assemblages produce fluid upon melting. The solidus for CO2-only system was determined by Grassi and Schmidt (2011), Tsuno and Dasgupta (2011). The volatile free-solidus is from Spandler et al. (2010).

8.4 Metamorphic evolution and partial melting in Åreskutan gneiss

The detailed petrographic and petrological investigation shown in chapters IV, V, VI allowed to identify three mineral assemblages related to different stages in the evolution of the paragneiss from Åreskutan (Tab. 8.2).

The mineral assemblage associated with the first stage inferred as formed at UHP metamorphic conditions (M1) is Grt, Phe, Ky, Rt, Coe, Jd. The metamorphic conditions estimated for M1 stage are 850 – 900˚C, 4 – 4.5 GPa, similar conditions were estimated by Klonowska et al. (2017). In particular, the key minerals identified in the paragneiss ascribed as part of M1 assemblage are Grt (interpreted as Grt I, that contains NGs, MPIs and Dia inclusions), Ky (included in Grt I), and Rt (included in Grt I). The presence of NGs and MPIs indicates the coexistence of the silicate melt and COH-fluid in the rock during M1 stage. Grt I is characterized texturally by anhedral shape (i.e., embayment) and coalescence of the grains (Grt I in Fig. 4.4a and b). It is characterized chemically by high Ca, Fe and Y content (Fig. 5.1d and e, Fig. 5.3c and d). The presence of Ph included in garnet cores (probably Grt I in this work) was well documented by Klonowska et al. (2014, 2017) and therefore this mineral has been included in the UHP M1 assemblage. Coesite was not found in the rock. However, the common presence of inclusions in garnet (Grt I) composed of polygonal quartz surrounded by radial cracks (Fig. 4.4e and Klonowska et al., 2014) suggest that the coesite may have been part of the primary assemblage at UHP conditions, but it did not survive the exhumation. The presence of polygonal quartz with radial cracks and the position of the quartz-coesite transition reaction allowed to include coesite in the primary assemblage of M1. Jadeite was not found in the rock, but thermodynamic modelling

of UHP assemblage performed by Klonowska et al. (2017) predicted its presence at peak conditions. Therefore, Jd was included in M1 stage assemblage.

The M2 stage is interpreted as formed at HP granulite condition. The P-T conditions are mostly based on work of Klonowska et al. (2017), however presence of sillimanite support these estimations. The mineral assemblage associated with this stage is composed of Grt (Grt II with Sil needles), Bt (Bt in Grt), Sil (prismatic crystals in the matrix and needles included in the Grt), Rt (Rt in Grt rim, corresponding to Grt II), Mnz (in the matrix and included in the Grt rim), Qz, Pl, Kfs, and Ilm. Grt II is characterized texturally by euhedral to subhedral shape (Fig. 4.4d) and compositionally by low Ca, Fe and Y content (Fig. 5.1d and e, Fig. 5.3). Bt in Grt has higher Ti (apfu) and X_{Mg} than Bt from the matrix and cracks in the Grt (Fig. 5.4). Rutile (Rt in Grt rim) contains much higher concentrations of zirconium (up to 875 ppm). Melt pseudomorphs are observed around prismatic sillimanite crystals (Fig. 4.5c). These microstructural observations support the presence of melt during stage M2. Therefore, a second anatectic event likely occurred in the sillimanite stability field, in agreement with thermodynamic modelling of Klonowska et al. (2017).

The latest stage (M3) is interpreted as formed during the retrograde metamorphism. The mineral assemblage assigned to this stage was mostly identified by detailed study of textural position of minerals and their chemical composition. All minerals formed in fractures or cracks are inferred to be the result of retrogression. The minerals observed in such a textural position are Pl, Ms, Bt (Bt in the matrix and in the cracks of Grt), Sil (needles in the matrix), Cb, Fe-Ox, Ilm, Rt (Rt in Corona), and Mnz. Biotite crystals in the matrix have low Ti (apfu) and X_{Mg}, similar to Bt from the cracks in the Grt. Monazite was included in M3 stage based on work of Majka et al. (2012), and Klonowska et al. (2017). The presence of carbonates associated with Fe-oxides indicate percolation of fluid in the rock.

Table 8.6 Summary of the P-T estimates and petrological observations from Åreskutan paragneiss based on this study and the literature (Majka et al., 2012; Klonowska et al., 2014, 2017, 2021)

Stage	Met. facies	P (GPa)	T (˚C)	Inc. in Grt	Melt/Fluid	Garnet	Mineral assemblage
M1	UHP eclogite	4.1 - 4.2[(a)] 4.0 - 4.5[(b)]	830 - 840[(a)] 850 - 900[(b)] 850 - 880[(c)]	NG, MPI Dia-MPI Dia[(a)]	melt[(b)] fluid[(b)]	Grt I	Grt, Ph[(a)], Ky, Rt, Coe[(a)], Jd[(a)] Dia
M2	HP granulite	1.0 - 1.1[(a)]	850 - 870[(a)]	Sil, Mnz	melt[(a), (d)]	Grt II	Grt, Bt, Qz, Sil, Rt, Ilm, Kfs, Pl, Mnz
M3	LP facies	0.5 - 0.8[(a)]	<680[(c)]		fluid[(d)]		Pl, Ms, Bt, Sil, Cb, Fe-Ox, Ilm, Rt, Mnz[(a)]

(a) – based on previous studies (Majka et al., 2012; Klonowska et al., 2014, 2017, 2021), **(b)** – based on results of re-homogenization experiments, **(c)** – based on ZiR geothermometry, **(d)** – based on microstructural observations, Met. - metamorphic

Multiple stages of garnet growth were interpreted based on major element composition, Y and P elemental maps acquired in single thin section and occurrences of the inclusions. Three main stages of growth were recognized, and they were subsequently correlated to the metamorphic phases (M1, M2 and M3) described in Tab. 8.2, and the monazite evolution documented by Klonowska et al. (2017). The monazites usually display an older Y-rich dark core and a younger Y-depleted bright mantle. In some cases, youngest rims might be also distinguished. The simplified evolution of the garnet and monazite is shown in Fig. 8.4.

Phase (1) reflects the growth of peritectic garnet in presence of anatectic melt and COH-fluid that led to entrapment and formation of NGs and Dia-bearing MPIs at UHP conditions (Fig. 8.4a); therefore, it is ascribed as Grt I and belongs to M1 assemblage. The garnet is enriched in Ca, Fe, Y, but depleted in P (Fig. 8.4b). The negative correlation of P and Y in Grt I might be explained by decupling of these elements during the garnet growth. Yttrium is more compatible with garnet than with melt, thus was incorporated into its structure (Acosta-Vigil et al., 2010), while phosphorus remained in the melt (Yakymchuk and Acosta-Vigil, 2019). This observation is also confirmed by relatively high concentrations of P_2O_5 in re-homogenized NGs (up to 0.23 wt%). In the next phase (2) garnet continues to grow with high Y and high P concentrations, coalescing previously crystallized grains. Phases

(1) and (2) comprise textural generation of garnet called here Grt I, that formed at UHP conditions.

The next phase of garnet growth – (3) occurred in the sillimanite stability field, entrapping sillimanite needles (Fig. 4). This garnet was ascribed as Grt II in the M2 assemblage. It is characterized by lower contents of Fe, Ca, Y and higher P compared to Grt I. Low concentration of Y is most likely a result of monazite growth (dark cores in monazite grains documented by Klonowska et al. (2017). The phase (4) of garnet growth is defined by the second high Y concentration zone positively corelated to P. This portion of garnet is overgrowth with low-P and low-Y garnet that might be correlated to second anatectic event and formation of low-Y monazite (bright mantles). High temperature event probably accelerated diffusion of elements in the garnet and led to homogenous composition in major elements and diffused older high-Y zone. (Fig. 4c,d).

The final stage of garnet evolution – phase (5) – consists in the formation of high P, low Y overgrowths, probably simultaneously with fracturing of the garnet and diffusive mobilisation of P along the fractures in the garnet (red arrow in Fig. 8.4b). This garnet can be correlated to the high-Y monazite rim.

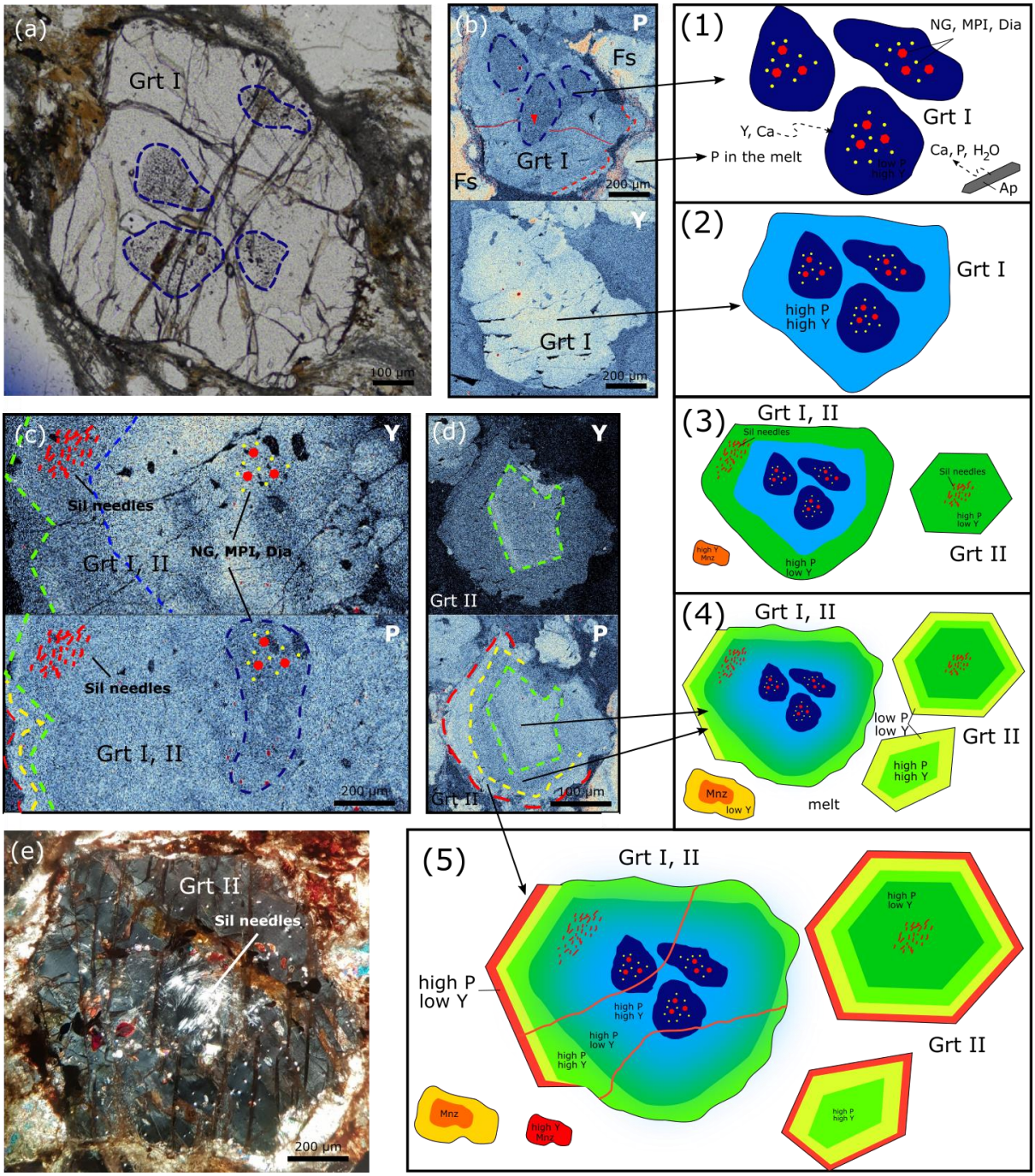

Figure 8.4 Schematic reconstruction of garnet growth stages from 1) to 5). **(a)** – photomicrograph in PPL of garnet I with marked (dashed blue line) clusters of NGs, MPIs, Dia. **(b)** – P and Y elemental map of Grt I, red arrow indicates fracture with higher P content. **(c)** – Y and P elemental map of Grt I overgrown with Grt II. (d) Y and P elemental map of Grt II. **(e)** – photomicrograph in XPL of garnet II, the sillimanite needles and the characteristic euhedral shape of garnet are visible. Shading of internal garnet in the image (4) and (5) represent diffusion.

The summary of geochronological data for Åreskutan Nappe was gathered from previous studies as reported in Tab. 3. In addition, ages from two adjacent units were also included: the Tväråklumparna Gneiss located c. 50 km SW from Åreskutan Nappe, and the Avardo Gneiss located c. 250 km towards NE. In the Åreskutan Nappe the record of prograde metamorphism is rarely preserved and shows ages >449 Ma. The age of migmatization and crystallization of melt is well constrained as monazite was also crystallizing and its age is c. 440 Ma. Then there is a record of deformation events related to the retrograde metamorphism connected to Early Scandian Collision (ESC), dated at c. 424 Ma, and to the Late Scandian Collision (LSC), dated at 417 Ma. Considering Tväråklumparna Gneiss, it is noticeable that migmatization (439 Ma) and deformation (410 Ma) occurred almost at the same age as in Åreskutan Nappe. However, the age of metamorphic peak - i.e., subduction - is much older (482 Ma). This older age (482.5 Ma) can be also found in Avardo Gneiss and is interpreted as the age of the metamorphic pressure peak. The ages of prograde metamorphism (454 - 460 Ma) and ESC (437 – 420 Ma) comparable with Åreskutan Nappe are also recorded. Therefore, it seems that on both sides of Åreskutan, the 482 Ma is an age of earliest metamorphism, and it is possible that rocks from Åreskutan Nappe were subducted much earlier that currently thought (455 Ma), but this record is not well preserved. Thus, the age of 482 Ma was also considered in reconstructing P-T-t path. The compilation of the data from Tab. 2 and Tab 3 allowed to constrain the possible P-T-t evolution (Fig. 8.5) for Åreskutan paragneiss and two possible P-T scenarios for exhumation are proposed. The first scenario implies two metamorphic stages: 1) prograde metamorphism, 2) anatexis at UHP (M1) and decompression, 3) prograde metamorphism, 4) anatexis at HP (M2) and decompression, 5) deformation related retrogression (M3). The second scenario assumes 1) prograde metamorphism, 2) anatexis at HP (M2) and almost isothermal decompression from UHP to HP conditions, 3) deformation related retrograde metamorphism (M3). The first scenario is in agreement with the proposed geodynamic evolution of rocks from SNC and observed

process of so called ‘dunk tectonics’ (Brueckner and van Roermund, 2004; Majka et al., 2014).

Table 8.7 Geochronological summary of (U)HP rocks from Åreskutan Nappe and related units to SW (50 km) Tväråklumparna Gneiss and NE (250 km) Avardo Gneiss.

Ages (Ma)	Method	Interpretation	Stage	Reference
Tväråklumparna Gneiss				
482 ± 3.8	U-Pb in Zrn	migmatization	Sub.	(Walczak et al., 2022)[a]
439 ± 3.8	U-Pb in Zrn	migmatization	Ex.	(Walczak et al., 2022)
~410	Ar-Ar in Hbl, Bt, Kfs	deformation	LSC	(Hacker and Gans, 2005)
Åreskutan Nappe				
~455	U-Pb in Mnz	prograde met.	Sub.	(Majka et al., 2012)[a]
449 ± 3.3	Lu-Hf in Grt	prograde met.	Sub.	(Klonowska, unpublished)
~439	U-Pb in Mnz	migmatization	Ex.	(Majka et al., 2012)
~424	U-Pb in Mnz	deformation	ESC	(Majka et al., 2012)[a]
441 ± 3.2	U-Pb in Mnz	migmatization	Ex.	(Klonowska et al., 2017)[a]
442 ± 4.0	U-Pb in Zrn	migmatization	Ex.	(Ladenberger et al., 2014)
437.8 ± 3.9	Rb-Sr multi-mineral	migmatization	Ex.	(Bender et al., 2019)
426.3 ± 3.1	Rb-Sr multi-mineral	deformation	ESC	(Bender et al., 2019)
417 ± 9.0	U-Pb in Spn	deformation	LSC	(Giuntoli et al., 2020)
Avardo Gneiss				
482.5 ± 3.7	U-Pb in Zrn	migmatization	Sub.	(Barnes et al., 2022)
420.6 ± 2.0	U-Pb in Zrn	deformation	ESC	(Barnes et al., 2022)
~454	Sm-Nd multi-mineral	prograde met.	Sub.	(Brueckner and van Roermund, 2004)
457.9 ± 4.5	Sm-Nd multi-mineral	prograde met.	Sub.	(Brueckner and Van Roermund, 2007)
460 ± 3.7	Sm-Nd multi-mineral	prograde met.	Sub.	(Brueckner and Van Roermund, 2007)
437 ± 4.5	Rb-Sr multi-mineral	deformation	ESC	(Grimmer et al., 2015)
423 ± 5.0	U-Th-Pb	deformation	ESC	(Williams and Claesson, 1987)

Sub. – subduction, Ex. – exhumation, ESC – Early Scandinavian Collision, LSC – Late Scandinavian Collision, met. – metamorphism, a – ages plotted in Fig. 5

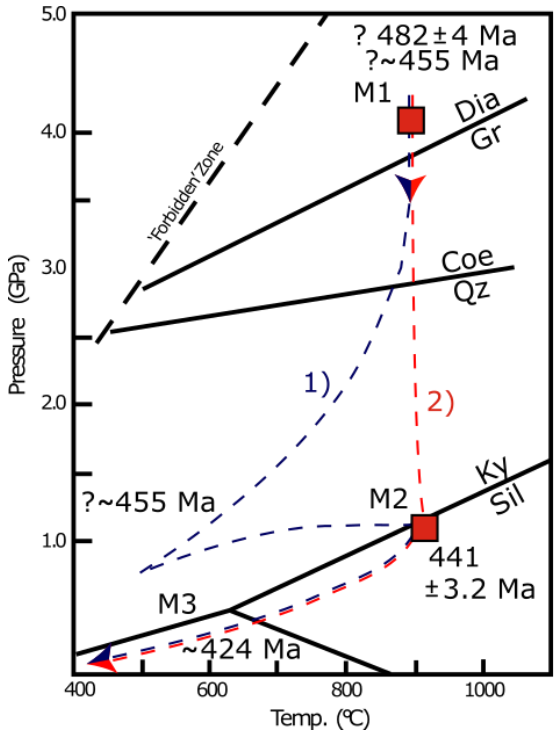

Figure 8.5 P-T-t diagram showing two partial melting events (M1 and M2) with associated mineral assemblage and M3 mineral assemblage associated to later deformation related retrogression. 1) is a possible scenario explaining two partial events involving two metamorphic stages. 2) is a scenario explaining two anatectic events by isothermal decompression. Ages plotted in P-T diagram according to works of: Majka et al., (2012), Klonowska et al. (2017), Walczak et al. (2022). For the details, see Tab 8.3.

8.5 Fate of UHP melts

Fates of rhyolitic UHP melts derived from subducting slab might be diverse. Melts formed through UHP anatexis might simply crystalize forming leucosome. If they will separate and migrate from their source rock, they might interact with other lithologies. For example these melts may interact with peridotites from mantle wedge inducing metasomatic reactions and producing pyroxenites as observed and documented by Malaspina et al. (2009). However, apparently even throughout multiple interaction with mantle rocks major element composition of partial melts remain mostly unaltered as was recently demonstrated by Rebaza et al. (2023) Rhyolitic melts due to its H_2O contents may also induce melting of ultramafic rocks (Naemura et al., 2018; Qin et al., 2018). Partial melts may subsequently mix with mantle derived melts forming e.g., shoshonitic magmas (Campbell et al., 2014; Jacob

et al., 2021). This type of magmas often contains mantle geochemical signature contaminated with crustal component.

Considering possible fate of UHP melts generated by Åreskutan paragneiss their composition is compared with shoshonites form Tromsø Nappe (Dalslåen et al., 2020) (Fig. 8.6). The UHP melts are one endmember component, while the second endmember is composition of mantle wedge peridotite or mantle derived melts. Shoshonitic magmas can be the result of mixing these two components.

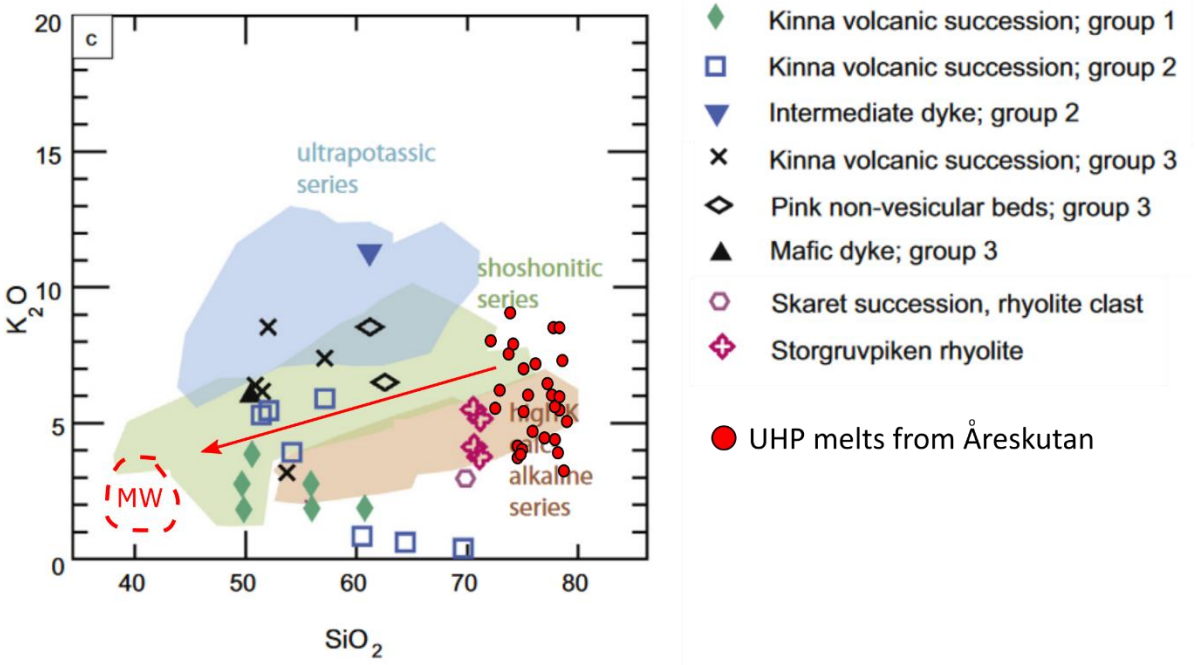

Figure 8.6 K_2O vs. SiO_2 diagram showing comparison of volcanic rocks from Skrvatatnet unit with UHP melts from Åreskutan paragneiss. The blue field represent ultrapotassic series, green field, shoshonitoc series and brown high-K calc-alkaline series. Red dashed circle indicates position of mantle wedge peridotite (MW), red arrow shows mixing trend.

8.6 Concluding remarks and future developments

The studies of inclusions such as NGs and MPIs trapped in garnet provide insights into anatectic processes at mantle depth in collisional setting. The case study from Åreskutan is a great example of possibilities of retrieving information that these inclusions preserve. In this work:

Metamorphic diamond was documented in one MPI, confirming the UHP character of the metamorphism in Åreskutan paragneisses.

1) The NGs were characterized, proving that they indeed are former droplets of anatectic melt. They were successfully re-homogenized at 850 – 900˚C and 4 – 4.5 GPa, and subsequently analysed for their major elements, H_2O and CO_2. These results provide the first compositions of natural UHP melt coexisting with diamond. The melts are rhyolitic with high alkali content just as predicted by experimental studies.
2) The contents of H_2O and CO_2 that were measured in re-homogenized UHP melts shed more light on the fate of volatiles during subduction of crustal rocks at mantle depth.
3) The presence of UHP fluids was detected in the form of MPI. The detailed examination of mineral compositions and residual fluids in the MPI allowed to reconstruct the primary composition of the UHP fluid present in the rock during the anatexis, which was made of $H_2O + CO_2 + N_2 + CH_4 \pm SO_4$.
4) Occurrence and spatial relationship between NGs and MPIs indicate simultaneous entrapment of two immiscible phases – fluid and melt. The present work reports for the first time an example of immiscibility of melt and fluid during UHP anatexis.
5) During the petrological investigation two partial melting events were identified in Åreskutan paragneiss: one at UHP eclogite facies conditions and the second at HP granulite facies conditions.

This thesis contributed to understanding how anatexis takes please during the ultradeep subduction, however some petrological problems remain unaddressed. In order to characterize more completely and better understand the chemistry of the UHP melts studied here, it would be necessary to measure the concentrations of trace elements. Geochemical signature would provide important constraints for understanding the fate of those melts. Similar knowledge gaps exist in regard to the UHP fluid present in Åreskutan paragneiss, which was not quantified owing to the modifications induced by formation of stepdaughter phases in the MPI. An interesting follow-up might be the comparison of the geochemical signatures of remelted NGs and MPIs. Finally, the multi-stage growth of the studied garnets is still not satisfactorily resolved. In order to verify the interpretation presented in this work it would be necessary to perform detailed trace element (Y and P) elemental mapping in a larger number of samples

Acknowledgments

First, I would like to thank my supervisors: Bernardo Cesare, Omar Bartoli and Jaroslaw Majka for showing me how the scientific work should look like, for the patience of explaining me complexities of inclusions studies and for guidance during whole my PhD project. Work in this help me to grow as a scientist, and as a person.

I would like to thank all people that make this work possible. My gratitude goes to Leonardo Tauro for teaching me how to prepare thin sections, and Andrea Risplendente for valuable suggestions and hours that we spent working on microprobe. My work on nanogranitoids wouldn't be possible without involvement of Stefano Poli and Sula Milani who showed me how to plan, prepare and perform re-homogenization experiments. My gratitude goes also to Richard Taylor and whole team in Zeiss facilities for giving me possibility to work on new state-of-art analytical instruments.

I want also to thank all my colleagues, officemates and friends in the department for constant presence and support.

Last but not least, I would like to thank my parents and sisters that despite of the distance they always supported me in all my choices.

References

Acosta-Vigil, A., Barich, A., Bartoli, O., Garrido, C.J., Cesare, B., Remusat, L., Poli, S., and Raepsaet, C., 2016, The composition of nanogranitoids in migmatites overlying the Ronda peridotites (Betic Cordillera, S Spain): the anatectic history of a polymetamorphic basement: Contributions to Mineralogy and Petrology, v. 171, p. 24, doi:10.1007/s00410-016-1230-3.

Acosta-Vigil, A., Buick, I., Hermann, J., Cesare, B., Rubatto, D., London, D., and Morgan, G.B., 2010, Mechanisms of Crustal Anatexis: a Geochemical Study of Partially Melted Metapelitic Enclaves and Host Dacite, SE Spain: Journal of Petrology, v. 51, p. 785–821, doi:10.1093/petrology/egp095.

Acosta-Vigil, A., Cesare, B., London, D., and Morgan, G.B., 2007, Microstructures and composition of melt inclusions in a crustal anatectic environment, represented by metapelitic enclaves within El Hoyazo dacites, SE Spain: Chemical Geology, v. 237, p. 450–465, doi:10.1016/j.chemgeo.2006.07.014.

Acosta-Vigil, A., London, D., Morgan, G.B., and Dewers, T.A., 2003, Solubility of excess alumina in hydrous granitic melts in equilibrium with peraluminous minerals at 700–800 °C and 200 MPa, and applications of the aluminum saturation index: Contributions to Mineralogy and Petrology, v. 146, p. 100–119, doi:10.1007/s00410-003-0486-6.

Acosta-vigil, A., Stöckhert, B., Hermann, J., Yaxley, G., Cesare, B., and Bartoli, O., 2017, Remelting of nanogranitoids in UHP felsic granulites from Erzgebirge (Bohemian Massif, Germany), *in* AGU Fall Meeting Abstracts, v. 2017, p. V24B-06.

Aubaud, C., Withers, A.C., Hirschmann, M.M., Guan, Y., Leshin, L.A., Mackwell, S.J., and Bell, D.R., 2007, Intercalibration of FTIR and SIMS for hydrogen measurements in glasses and nominally anhydrous minerals: American Mineralogist, v. 92, p. 811–828, doi:10.2138/am.2007.2248.

Auzanneau, E., Vielzeuf, D., and Schmidt, M.W., 2006, Experimental evidence of decompression melting during exhumation of subducted continental crust:

Contributions to Mineralogy and Petrology, v. 152, p. 125–148, doi:10.1007/s00410-006-0104-5.

Balta, J.B., Beckett, J.R., and Asimow, P.D., 2011, Thermodynamic properties of alloys of gold-74/palladium-26 with variable amounts of iron and the use of Au-Pd-Fe alloys as containers for experimental petrology: American Mineralogist, v. 96, p. 1467–1474, doi:10.2138/am.2011.3637.

Barich, A., Acosta-Vigil, A., Garrido, C.J., Cesare, B., Tajčmanová, L., and Bartoli, O., 2014, Microstructures and petrology of melt inclusions in the anatectic sequence of Jubrique (Betic Cordillera, S Spain): Implications for crustal anatexis: Lithos, v. 206–207, p. 303–320, doi:10.1016/j.lithos.2014.08.003.

Barnes, C.J., Bukała, M., Callegari, R., Walczak, K., Kooijman, E., Kielman-Schmitt, M., and Majka, J., 2022, Zircon and monazite reveal late Cambrian/early Ordovician partial melting of the Central Seve Nappe Complex, Scandinavian Caledonides: Contributions to Mineralogy and Petrology, v. 177, p. 92, doi:10.1007/s00410-022-01958-x.

Bartoli, O., Acosta-Vigil, A., Ferrero, S., and Cesare, B., 2016, Granitoid magmas preserved as melt inclusions in high-grade metamorphic rock: American Mineralogist, v. 101, p. 1543–1559, doi:10.2138/am-2016-5541CCBYNCND.

Bartoli, O., and Cesare, B., 2020, Nanorocks: a 10-year-old story: Rendiconti Lincei. Scienze Fisiche e Naturali, v. 31, p. 249–257, doi:10.1007/s12210-020-00898-7.

Bartoli, O., Cesare, B., Poli, S., Acosta-Vigil, A., Esposito, R., Turina, A., Bodnar, R.J., Angel, R.J., and Hunter, J., 2013a, Nanogranite inclusions in migmatitic garnet: behavior during piston-cylinder remelting experiments: Geofluids, v. 13, p. 405–420, doi:10.1111/gfl.12038.

Bartoli, O., Cesare, B., Poli, S., Bodnar, R.J., Acosta-Vigil, A., Frezzotti, M.L., and Meli, S., 2013b, Recovering the composition of melt and the fluid regime at the onset of crustal anatexis and S-type granite formation: Geology, v. 41, p. 115–118, doi:10.1130/G33455.1.

Bartoli, O., Cesare, B., Remusat, L., Acosta-Vigil, A., and Poli, S., 2014, The H2O content of granite embryos: Earth and Planetary Science Letters, v. 395, p. 281–290, doi:10.1016/j.epsl.2014.03.031.

Behrens, H., and Jantos, N., 2001, The effect of anhydrous composition on water solubility in granitic melts: American Mineralogist, v. 86, p. 14–20, doi:10.2138/am-2001-0102.

Bender, H., Glodny, J., and Ring, U., 2019, Absolute timing of Caledonian orogenic wedge assembly, Central Sweden, constrained by Rb–Sr multi-mineral isochron data: Lithos, v. 344–345, p. 339–359, doi:10.1016/j.lithos.2019.06.033.

Bodnar, R.J., and Frezzotti, M.L., 2020, Microscale Chemistry: Raman Analysis of Fluid and Melt Inclusions: Elements, v. 16, p. 93–98, doi:10.2138/gselements.16.2.93.

Borghini, A., Nicoli, G., Ferrero, S., Remusat, L., Borghini, G., and Milani, S., 2023, The role of continental subduction in mantle metasomatism and carbon recycling revealed by melt inclusions in UHP eclogites: SCIENCE ADVANCES,.

Brown, M., 2007, Metamorphic Conditions in Orogenic Belts: A Record of Secular Change: International Geology Review, v. 49, p. 193–234, doi:10.2747/0020-6814.49.3.193.

Brown, M., Schulmann, K., and White, R.W., 2011, Granulites, partial melting and the rheology of the lower crust: PROCESSES IN THE LOWER CRUST: Journal of Metamorphic Geology, v. 29, p. 1–6, doi:10.1111/j.1525-1314.2010.00917.x.

Brueckner, H.K., and van Roermund, H.L.M., 2004, Dunk tectonics: A multiple subduction/eduction model for the evolution of the Scandinavian Caledonides: DUNK TECTONICS, SCANDINAVIAN CALEDONIDES: Tectonics, v. 23, p. n/a-n/a, doi:10.1029/2003TC001502.

Brueckner, H.K., and Van Roermund, H.L.M., 2007, Concurrent HP metamorphism on both margins of Iapetus: Ordovician ages for eclogites and garnet pyroxenites from

the Seve Nappe Complex, Swedish Caledonides: Journal of the Geological Society, v. 164, p. 117–128, doi:10.1144/0016-76492005-139.

Bukała, M., Klonowska, I., Barnes, C., Majka, J., Kośmińska, K., Janák, M., Fassmer, K., Broman, C., and Luptáková, J., 2018, UHP metamorphism recorded by phengite eclogite from the Caledonides of northern Sweden: *P-T* path and tectonic implications: Journal of Metamorphic Geology, v. 36, p. 547–566, doi:10.1111/jmg.12306.

Bureau, H., Trocellier, P., Shaw, C., Khodja, H., Bolfan-Casanova, N., and Demouchy, S., 2003, Determination of the concentration of water dissolved in glasses and minerals using nuclear microprobe: Nuclear Instruments and Methods in Physics Research Section B: Beam Interactions with Materials and Atoms, v. 210, p. 449–454, doi:10.1016/S0168-583X(03)01074-7.

Campbell, I.H., Stepanov, A.S., Liang, H.-Y., Allen, C.M., Norman, M.D., Zhang, Y.-Q., and Xie, Y.-W., 2014, The origin of shoshonites: new insights from the Tertiary high-potassium intrusions of eastern Tibet: Contributions to Mineralogy and Petrology, v. 167, p. 983, doi:10.1007/s00410-014-0983-9.

Carswell, D.A., Cuthbert, S.J., and Krogh Ravna, E.J., 1999, Ultrahigh-Pressure Metamorphism in the Western Gneiss Region of the Norwegian Caledonides: International Geology Review, v. 41, p. 955–966, doi:10.1080/00206819909465182.

Carvalho, B.B., Bartoli, O., Cesare, B., Tacchetto, T., Gianola, O., Ferri, F., Aradi, L.E., and Szabó, C., 2020, Primary CO2-bearing fluid inclusions in granulitic garnet usually do not survive: Earth and Planetary Science Letters, v. 536, p. 116170, doi:10.1016/j.epsl.2020.116170.

Carvalho, B.B., Bartoli, O., Ferri, F., Cesare, B., Ferrero, S., Remusat, L., Capizzi, L.S., and Poli, S., 2019, Anatexis and fluid regime of the deep continental crust: New clues from melt and fluid inclusions in metapelitic migmatites from Ivrea Zone (NW Italy): Journal of Metamorphic Geology, v. 37, p. 951–975, doi:10.1111/jmg.12463.

Cesare, B., Acosta-Vigil, A., Bartoli, O., and Ferrero, S., 2015, What can we learn from melt inclusions in migmatites and granulites? Lithos, v. 239, p. 186–216, doi:10.1016/j.lithos.2015.09.028.

Cesare, B., Ferrero, S., Salvioli-Mariani, E., Pedron, D., and Cavallo, A., 2009, "Nanogranite" and glassy inclusions: The anatectic melt in migmatites and granulites: Geology, v. 37, p. 627–630, doi:10.1130/G25759A.1.

Cesare, B., Maineri, C., Baron Toaldo, A., Pedron, D., and Acosta Vigil, A., 2007, Immiscibility between carbonic fluids and granitic melts during crustal anatexis: A fluid and melt inclusion study in the enclaves of the Neogene Volcanic Province of SE Spain: Chemical Geology, v. 237, p. 433–449, doi:10.1016/j.chemgeo.2006.07.013.

Cesare, B., Meli, S., Nodari, L., and Russo, U., 2005, Fe3+ reduction during biotite melting in graphitic metapelites: another origin of CO2 in granulites: Contributions to Mineralogy and Petrology, v. 149, p. 129–140, doi:10.1007/s00410-004-0646-3.

Chen, Y.-X., Zheng, Y.-F., Gao, X.-Y., and Hu, Z., 2014, Multiphase solid inclusions in zoisite-bearing eclogite: evidence for partial melting of ultrahigh-pressure metamorphic rocks during continental collision: Lithos, v. 200, p. 1–21, doi:10.1016/j.lithos.2014.04.004.

Chopin, C., 1984, Coesite and pure pyrope in high-grade blueschists of the Western Alps: a first record and some consequences: Contributions to Mineralogy and Petrology, v. 86, p. 107–118, doi:10.1007/BF00381838.

Chopin, C., 2003, Ultrahigh-pressure metamorphism: tracing continental crust into the mantle: Earth and Planetary Science Letters, v. 212, p. 1–14, doi:10.1016/S0012-821X(03)00261-9.

Christensen, N.I., and Mooney, W.D., 1995, Seismic velocity structure and composition of the continental crust: A global view: Journal of Geophysical Research: Solid Earth, v. 100, p. 9761–9788, doi:10.1029/95JB00259.

Clemens, J.D., 2006, Melting of the continental crust: fluid regimes, melting reactions, and source-rock fertility, *in* Brown, M. and Rushmer, T. eds., Cambridge, UK, Cambridge University Press, p. 297–331, http://dx.doi.org/10.2277/0521782376 (accessed January 2023).

Clemens, J.D., Stevens, G., and Bryan, S.E., 2020, Conditions during the formation of granitic magmas by crustal melting – Hot or cold; drenched, damp or dry? Earth-Science Reviews, v. 200, p. 102982, doi:10.1016/j.earscirev.2019.102982.

Compagnoni, R., and Rolfo, F., 2003, UHPM units in the Western Alps, *in* Papp, G., Weiszburg, T.G., Carswell, D.A., Compagnoni, R., and Rolfo, F. eds., Ultrahigh Pressure Metamorphism, Budapest, Mineralogical Society of Great Britain and Ireland, p. 13–49, doi:10.1180/EMU-notes.5.2.

Connolly, J. a. D., and Cesare, B., 1993, C-O-H-S fluid composition and oxygen fugacity in graphitic metapelites: Journal of Metamorphic Geology, v. 11, p. 379–388, doi:10.1111/j.1525-1314.1993.tb00155.x.

Créon, L., Levresse, G., Remusat, L., Bureau, H., and Carrasco-Núñez, G., 2018, New method for initial composition determination of crystallized silicate melt inclusions: Chemical Geology, doi:10.1016/j.chemgeo.2018.02.038.

Dalslåen, B.H., Gasser, D., Grenne, T., Augland, L.E., and Corfu, F., 2020, Ordovician shoshonitic to ultrapotassic volcanism in the central Norwegian Caledonides: The result of sediment subduction, mantle metasomatism and mantle partial melting: Lithos, v. 356–357, p. 105372, doi:10.1016/j.lithos.2020.105372.

Dobrzhinetskaya, L., Faryad, S.W., Wallis, S., and Cuthbert, S., 2011, Ultrahigh-Pressure Metamorphism: 25 Years After The Discovery Of Coesite And Diamond: Elsevier B.V., Elsevier Insights.

Duncan, M.S., and Dasgupta, R., 2014, CO2 solubility and speciation in rhyolitic sediment partial melts at 1.5–3.0GPa – Implications for carbon flux in subduction

zones: Geochimica et Cosmochimica Acta, v. 124, p. 328–347, doi:10.1016/j.gca.2013.09.026.

Ewing, T.A., Hermann, J., and Rubatto, D., 2013, The robustness of the Zr-in-rutile and Ti-in-zircon thermometers during high-temperature metamorphism (Ivrea-Verbano Zone, northern Italy): Contributions to Mineralogy and Petrology, v. 165, p. 757–779, doi:10.1007/s00410-012-0834-5.

Fernández-Díaz, L., Fernández-González, Á., and Prieto, M., 2010, The role of sulfate groups in controlling CaCO3 polymorphism: Geochimica et Cosmochimica Acta, v. 74, p. 6064–6076, doi:10.1016/j.gca.2010.08.010.

Ferrando, S., Frezzotti, M.L., Dallai, L., and Compagnoni, R., 2005, Multiphase solid inclusions in UHP rocks (Su-Lu, China): Remnants of supercritical silicate-rich aqueous fluids released during continental subduction: Chemical Geology, v. 223, p. 68–81, doi:10.1016/j.chemgeo.2005.01.029.

Ferrero, S., Ague, J.J., O'Brien, P.J., Wunder, B., Remusat, L., Ziemann, M.A., and Axler, J., 2021, High-pressure, halogen-bearing melt preserved in ultrahigh-temperature felsic granulites of the Central Maine Terrane, Connecticut (U.S.A.): American Mineralogist, v. 106, p. 1225–1236, doi:10.2138/am-2021-7690.

Ferrero, S., Bartoli, O., Cesare, B., Salvioli-Mariani, E., Acosta-Vigil, A., Cavallo, A., Groppo, C., and Battiston, S., 2012, Microstructures of melt inclusions in anatectic metasedimentary rocks: ANATECTIC MELT INCLUSIONS IN MIGMATITES: Journal of Metamorphic Geology, v. 30, p. 303–322, doi:10.1111/j.1525-1314.2011.00968.x.

Ferrero, S., Bodnar, R.J., Cesare, B., and Viti, C., 2011, Re-equilibration of primary fluid inclusions in peritectic garnet from metapelitic enclaves, El Hoyazo, Spain: Lithos, v. 124, p. 117–131, doi:10.1016/j.lithos.2010.09.004.

Ferrero, S., Braga, R., Berkesi, M., Cesare, B., and Laridhi Ouazaa, N., 2014, Production of metaluminous melt during fluid-present anatexis: an example from the Maghrebian

basement, La Galite Archipelago, central Mediterranean: Journal of Metamorphic Geology, v. 32, p. 209–225, doi:10.1111/jmg.12068.

Ferrero, S., O'Brien, P.J., Borghini, A., Wunder, B., Wälle, M., Günter, C., and Ziemann, M.A., 2019, A treasure chest full of nanogranitoids: an archive to investigate crustal melting in the Bohemian Massif: Geological Society, London, Special Publications, v. 478, p. 13–38, doi:10.1144/SP478.19.

Ferrero, S., Wunder, B., Walczak, K., O'Brien, P.J., and Ziemann, M.A., 2015, Preserved near ultrahigh-pressure melt from continental crust subducted to mantle depths: Geology, v. 43, p. 447–450, doi:10.1130/G36534.1.

Ferrero, S., Wunder, B., Ziemann, M.A., Wälle, M., and O'Brien, P.J., 2016, Carbonatitic and granitic melts produced under conditions of primary immiscibility during anatexis in the lower crust: Earth and Planetary Science Letters, v. 454, p. 121–131, doi:10.1016/j.epsl.2016.08.043.

Frezzotti, M.L., Tecce, F., and Casagli, A., 2012, Raman spectroscopy for fluid inclusion analysis: Journal of Geochemical Exploration, v. 112, p. 1–20, doi:10.1016/j.gexplo.2011.09.009.

Ganzhorn, A.C., Labrousse, L., Prouteau, G., Leroy, C., Vrijmoed, J.C., Andersen, T.B., and Arbaret, L., 2014, Structural, petrological and chemical analysis of syn-kinematic migmatites: insights from the Western Gneiss Region, Norway: Journal of Metamorphic Geology, v. 32, p. 647–673, doi:10.1111/jmg.12084.

Gao, X.-Y., Zheng, Y.-F., and Chen, Y.-X., 2012, Dehydration melting of ultrahigh-pressure eclogite in the Dabie orogen: evidence from multiphase solid inclusions in garnet: Journal of Metamorphic Geology, v. 30, p. 193–212, doi:10.1111/j.1525-1314.2011.00962.x.

Gee, D.G., Fossen, H., Henriksen, N., and Higgins, A.K., 2008, From the Early Paleozoic Platforms of Baltica and Laurentia to the Caledonide Orogen of Scandinavia and

Greenland: Episodes Journal of International Geoscience, v. 31, p. 44–51, doi:10.18814/epiiugs/2008/v31i1/007.

Gee, D.G., Janák, M., Majka, J., Robinson, P., and van Roermund, H., 2013, Subduction along and within the Baltoscandian margin during closing of the Iapetus Ocean and Baltica-Laurentia collision: Lithosphere, v. 5, p. 169–178, doi:10.1130/L220.1.

Gianola, O., Bartoli, O., Ferri, F., Galli, A., Ferrero, S., Capizzi, L.S., Liebske, C., Remusat, L., Poli, S., and Cesare, B., 2021, Anatectic melt inclusions in ultra high temperature granulites: Journal of Metamorphic Geology, v. 39, p. 321–342, doi:10.1111/jmg.12567.

Gilotti, J.A., 2013, The Realm of Ultrahigh-Pressure Metamorphism: Elements, v. 9, p. 255–260, doi:10.2113/gselements.9.4.255.

Giuntoli, F., Menegon, L., Warren, C.J., Darling, J., and Anderson, M.W., 2020, Protracted Shearing at Midcrustal Conditions During Large-Scale Thrusting in the Scandinavian Caledonides: Tectonics, v. 39, p. e2020TC006267, doi:10.1029/2020TC006267.

Grassi, D., and Schmidt, M.W., 2011, The Melting of Carbonated Pelites from 70 to 700 km Depth: Journal of Petrology, v. 52, p. 765–789, doi:10.1093/petrology/egr002.

Grimmer, J.C., Glodny, J., Drüppel, K., Greiling, R.O., and Kontny, A., 2015, Early- to mid-Silurian extrusion wedge tectonics in the central Scandinavian Caledonides: Geology, v. 43, p. 347–350, doi:10.1130/G36433.1.

Hacker, B.R., and Gans, P.B., 2005, Continental collisions and the creation of ultrahigh-pressure terranes: Petrology and thermochronology of nappes in the central Scandinavian Caledonides: Geological Society of America Bulletin, v. 117, p. 117, doi:10.1130/B25549.1.

Hacker, B.R., McClelland, W.C., and Liou, J.G., 2006, Ultrahigh-pressure metamorphism: Deep continental subduction: Geological Society of America, doi:10.1130/SPE403.

Hermann, J., and Green, D.H., 2001, Experimental constraints on high pressure melting in subducted crust: Earth and Planetary Science Letters, v. 188, p. 149–168, doi:10.1016/S0012-821X(01)00321-1.

Hermann, J., and Rubatto, D., 2014, Subduction of Continental Crust to Mantle Depth, *in* Treatise on Geochemistry, Elsevier, p. 309–340, doi:10.1016/B978-0-08-095975-7.00309-0.

Hermann, J., and Spandler, C.J., 2008, Sediment Melts at Sub-arc Depths: an Experimental Study: Journal of Petrology, v. 49, p. 717–740, doi:10.1093/petrology/egm073.

Hermann, J., Spandler, C., Hack, A., and Korsakov, A., 2006, Aqueous fluids and hydrous melts in high-pressure and ultra-high pressure rocks: Implications for element transfer in subduction zones: Lithos, v. 92, p. 399–417, doi:10.1016/j.lithos.2006.03.055.

Hermann, J., Zheng, Y.-F., and Rubatto, D., 2013, Deep Fluids in Subducted Continental Crust: Elements, v. 9, p. 281–287, doi:10.2113/gselements.9.4.281.

Hirajima, T., and Nakamura, D., 2003, The Dabie Shan–Sulu orogen, *in* Carswell, D.A., Compagnoni, R., and Rolfo, F. eds., Ultrahigh Pressure Metamorphism, Mineralogical Society of Great Britain and Ireland, v. 5, p. 0, doi:10.1180/EMU-notes.5.5.

Holness, M.B., and Isherwood, C.E., 2003, The aureole of the Rum Tertiary Igneous Complex, Scotland: Journal of the Geological Society, v. 160, p. 15–27, doi:10.1144/0016-764901-098.

Holness, M.B., and Sawyer, E.W., 2008, On the Pseudomorphing of Melt-filled Pores During the Crystallization of Migmatites: Journal of Petrology, v. 49, p. 1343–1363, doi:10.1093/petrology/egn028.

Jacob, J.-B., Moyen, J.-F., Fiannacca, P., Laurent, O., Bachmann, O., Janoušek, V., Farina, F., and Villaros, A., 2021, Crustal melting vs. fractionation of basaltic magmas: Part 2, Attempting to quantify mantle and crustal contributions in granitoids: Lithos, v. 402–403, p. 106292, doi:10.1016/j.lithos.2021.106292.

Jamieson, R.A., Unsworth, M.J., Harris, N.B.W., Rosenberg, C.L., and Schulmann, K., 2011, Crustal Melting and the Flow of Mountains: Elements, v. 7, p. 253–260, doi:10.2113/gselements.7.4.253.

Janák, M., Krogh Ravna, E.J., Kullerud, K., Yoshida, K., Milovský, R., and Hirajima, T., 2013, Discovery of diamond in the Tromsø Nappe, Scandinavian Caledonides (N. Norway): Journal of Metamorphic Geology, v. 31, p. 691–703, doi:10.1111/jmg.12040.

Johnson, M.C., and Plank, T., 2000, Dehydration and melting experiments constrain the fate of subducted sediments: Geochemistry, Geophysics, Geosystems, v. 1, doi:10.1029/1999GC000014.

Kamenetsky, V., and Danyushevsky, L., 2005, Metals in quartz-hosted melt inclusions: Natural facts and experimental artifacts: American Mineralogist - AMER MINERAL, v. 90, p. 1674–1678, doi:10.2138/am.2005.1969.

Kennedy, C.S., and Kennedy, G.C., 1976, The equilibrium boundary between graphite and diamond: Journal of Geophysical Research (1896-1977), v. 81, p. 2467–2470, doi:10.1029/JB081i014p02467.

Klonowska, I., Janák, M., Majka, J., Petrík, I., Froitzheim, N., Gee, D.G., and Sasinková, V., 2017, Microdiamond on Åreskutan confirms regional UHP metamorphism in the Seve Nappe Complex of the Scandinavian Caledonides: Journal of Metamorphic Geology, v. 35, p. 541–564, doi:10.1111/jmg.12244.

Klonowska, I., Majka, J., Janák, M., Gee, D.G., and Ladenberger, A., 2014, Pressure–temperature evolution of a kyanite–garnet pelitic gneiss from Åreskutan: evidence of ultra-high-pressure metamorphism of the Seve Nappe Complex, west-central

Jämtland, Swedish Caledonides: Geological Society, London, Special Publications, v. 390, p. 321–336, doi:10.1144/SP390.7.

Klonowska, I., Majka, J., Janák, M., Petrík, I., Froitzheim, N., Gee, D.G., and Cuthbert, S., 2021, Comment on the paper: “Evolution of a gneiss in the Seve nappe complex of central Sweden – Hints at an early Caledonian, medium-pressure metamorphism” by: Lithos, v. 400–401, p. 106067, doi:10.1016/j.lithos.2021.106067.

Kohn, M.J., 2020, A refined zirconium-in-rutile thermometer: American Mineralogist, v. 105, p. 963–971, doi:10.2138/am-2020-7091.

Kooijman, E., Smit, M.A., Mezger, K., and Berndt, J., 2012, Trace element systematics in granulite facies rutile: implications for Zr geothermometry and provenance studies: Journal of Metamorphic Geology, v. 30, p. 397–412, doi:10.1111/j.1525-1314.2012.00972.x.

Korsakov, A.V., and Hermann, J., 2006, Silicate and carbonate melt inclusions associated with diamonds in deeply subducted carbonate rocks: Earth and Planetary Science Letters, v. 241, p. 104–118, doi:10.1016/j.epsl.2005.10.037.

Labrousse, L., Duretz, T., and Gerya, T., 2015, H2O-fluid-saturated melting of subducted continental crust facilitates exhumation of ultrahigh-pressure rocks in continental subduction zones: Earth and Planetary Science Letters, v. 428, p. 151–161, doi:10.1016/j.epsl.2015.06.016.

Labrousse, L., Prouteau, G., and Ganzhorn, A.-C., 2011, Continental exhumation triggered by partial melting at ultrahigh pressure: Geology, v. 39, p. 1171–1174, doi:10.1130/G32316.1.

Ladenberger, A., Be’eri-Shlevin, Y., Claesson, S., Gee, D.G., Majka, J., and Romanova, I.V., 2014, Tectonometamorphic evolution of the Åreskutan Nappe – Caledonian history revealed by SIMS U–Pb zircon geochronology: Geological Society, London, Special Publications, v. 390, p. 337–368, doi:10.1144/SP390.10.

Lanari, P., Vho, A., Bovay, T., Airaghi, L., and Centrella, S., 2019, Quantitative compositional mapping of mineral phases by electron probe micro-analyser: Geological Society, London, Special Publications, v. 478, p. 39–63, doi:10.1144/SP478.4.

Lanari, P., Vidal, O., De Andrade, V., Dubacq, B., Lewin, E., Grosch, E.G., and Schwartz, S., 2014, XMapTools: A MATLAB©-based program for electron microprobe X-ray image processing and geothermobarometry: Computers & Geosciences, v. 62, p. 227–240, doi:10.1016/j.cageo.2013.08.010.

Le Maitre, R.W., Streckeisen, A., Zanettin, B., Le Bas, M.J., Bonin, B., and Bateman, P. (Eds.), 2002, Igneous Rocks: A Classification and Glossary of Terms: Recommendations of the International Union of Geological Sciences Subcommission on the Systematics of Igneous Rocks: Cambridge, Cambridge University Press, doi:10.1017/CBO9780511535581.

Liou, J.G., Ernst, W.G., Zhang, R.Y., Tsujimori, T., and Jahn, B.M., 2009, Ultrahigh-pressure minerals and metamorphic terranes – The view from China: Journal of Asian Earth Sciences, v. 35, p. 199–231, doi:10.1016/j.jseaes.2008.10.012.

Liu, P., Zhang, J., Massonne, H.-J., and Jin, Z., 2018, Polyphase solid-inclusions formed by interactions between infiltrating fluids and precursor minerals enclosed in garnet of UHP rocks from the Dabie Shan, China: American Mineralogist, v. 103, p. 1663–1673, doi:10.2138/am-2018-6395.

Majka, J., Be'eri-Shlevin, Y., Gee, D.G., Ladenberger, A., Claesson, S., Konečný, P., and Klonowska, I., 2012, Multiple monazite growth in the Åreskutan migmatite: evidence for a polymetamorphic Late Ordovician to Late Silurian evolution in the Seve Nappe Complex of west-central Jämtland, Sweden: Journal of GEOsciences, p. 3–23, doi:10.3190/jgeosci.112.

Majka, J., Rosén, Å., Janák, M., Froitzheim, N., Klonowska, I., Manecki, M., Sasinková, V., and Yoshida, K., 2014, Microdiamond discovered in the Seve Nappe (Scandinavian

Caledonides) and its exhumation by the “vacuum-cleaner” mechanism: Geology, v. 42, p. 1107–1110, doi:10.1130/G36108.1.

Malaspina, N., Hermann, J., and Scambelluri, M., 2009, Fluid/mineral interaction in UHP garnet peridotite: Lithos, v. 107, p. 38–52, doi:10.1016/j.lithos.2008.07.006.

Malaspina, N., Hermann, J., Scambelluri, M., and Compagnoni, R., 2006, Polyphase inclusions in garnet–orthopyroxenite (Dabie Shan, China) as monitors for metasomatism and fluid-related trace element transfer in subduction zone peridotite: Earth and Planetary Science Letters, v. 249, p. 173–187, doi:10.1016/j.epsl.2006.07.017.

Mann, U., and Schmidt, M.W., 2015, Melting of pelitic sediments at subarc depths: 1. Flux vs. fluid-absent melting and a parameterization of melt productivity: Chemical Geology, v. 404, p. 150–167, doi:10.1016/j.chemgeo.2015.02.032.

Meinhold, G., 2010, Rutile and its applications in earth sciences: Earth-Science Reviews, v. 102, p. 1–28, doi:10.1016/j.earscirev.2010.06.001.

Morgan, G.B., and London, D., 2005, Effect of current density on the electron microprobe analysis of alkali aluminosilicate glasses: American Mineralogist, v. 90, p. 1131–1138, doi:10.2138/am.2005.1769.

Morgan, G.B., and London, D., 1996, Optimizing the electron microprobe analysis of hydrous alkali aluminosilicate glasses: American Mineralogist, v. 81, p. 1176–1185, doi:10.2138/am-1996-9-1016.

Muth, M., Duncan, M.S., and Dasgupta, R., 2020, The Effect of Variable Na/K on the CO2 Content of Slab-Derived Rhyolitic Melts, *in* Carbon in Earth’s Interior, American Geophysical Union (AGU), p. 195–208, doi:10.1002/9781119508229.ch17.

Naemura, K., Hirajima, T., Svojtka, M., Shimizu, I., and Iizuka, T., 2018, Fossilized Melts in Mantle Wedge Peridotites: Scientific Reports, v. 8, p. 10116, doi:10.1038/s41598-018-28264-6.

Ni, H., and Keppler, H., 2013, Carbon in Silicate Melts: Reviews in Mineralogy and Geochemistry, v. 75, p. 251–287, doi:10.2138/rmg.2013.75.9.

Nichols, G.T., Wyllie, P.J., and Stern, C.R., 1994, Subduction zone melting of pelagic sediments constrained by melting experiments: Nature, v. 371, p. 785–788, doi:10.1038/371785a0.

Nicoli, G., and Ferrero, S., 2021, Nanorocks, volatiles and plate tectonics: Geoscience Frontiers, v. 12, p. 101188, doi:10.1016/j.gsf.2021.101188.

Parisatto, M., Turina, A., Cruciani, G., Mancini, L., Peruzzo, L., and Cesare, B., 2018, Three-dimensional distribution of primary melt inclusions in garnets by X-ray microtomography: American Mineralogist, v. 103, p. 911–926, doi:10.2138/am-2018-6216CCBYNCND.

Park, C., Kim, N., Choi, S.-J., and Song, Y., 2020, Mg-Phengite in Carbonate Rock Syngenetically Formed from Hydrothermal Fluid: Micro-Textural Evidence and Mineral Chemistry: Minerals, v. 10, p. 668, doi:10.3390/min10080668.

Patiño Douce, A.E., and Johnston, A.D., 1991, Phase equilibria and melt productivity in the pelitic system: implications for the origin of peraluminous granitoids and aluminous granulites: Contributions to Mineralogy and Petrology, v. 107, p. 202–218, doi:10.1007/BF00310707.

Perchuk, A.L., Burchard, M., Maresch, W.V., and Schertl, H.-P., 2005, Fluid-mediated modification of garnet interiors under ultrahigh-pressure conditions: Terra Nova, v. 17, p. 545–553, doi:10.1111/j.1365-3121.2005.00647.x.

Perrillat, J.P., 2003, Kinetics of the Coesite-Quartz Transition: Application to the Exhumation of Ultrahigh-Pressure Rocks: Journal of Petrology, v. 44, p. 773–788, doi:10.1093/petrology/44.4.773.

Petrík, I., Janák, M., Klonowska, I., Majka, J., Froitzheim, N., Yoshida, K., Sasinková, V., Konečný, P., and Vaculovič, T., 2019, Monazite behaviour during metamorphic

evolution of a diamond-bearing gneiss: a case study from the Seve Nappe Complex, Scandinavian Caledonides: Journal of Petrology, p. egz051, doi:10.1093/petrology/egz051.

Qin, J.-F., Lai, S.-C., Long, X.-P., Li, Y.-F., Ju, Y.-J., Zhao, S.-W., Zhu, R.-Z., Wang, J.-B., and Zhang, Z.-Z., 2018, Hydrous melting of metasomatized mantle wedge and crustal growth in the post-collisional stage: Evidence from Late Triassic monzodiorite and its mafic enclaves in the south Qinling (central China): Lithosphere, v. 11, p. 3–20, doi:10.1130/L1006.1.

Rasmussen, D.J., Plank, T.A., Wallace, P.J., Newcombe, M.E., and Lowenstern, J.B., 2020, Vapor-bubble growth in olivine-hosted melt inclusions: American Mineralogist, v. 105, p. 1898–1919, doi:10.2138/am-2020-7377.

Rebaza, A.M., Mallik, A., and Straub, S.M., 2023, Multiple episodes of rock-melt reaction at the slab-mantle interface: Formation of high silica primary magmas in intermediate to hot subduction zones: Journal of Petrology, p. egad011, doi:10.1093/petrology/egad011.

Rosenberg, C.L., and Handy, M.R., 2005, Experimental deformation of partially melted granite revisited: implications for the continental crust: Journal of Metamorphic Geology, v. 23, p. 19–28, doi:10.1111/j.1525-1314.2005.00555.x.

Sawyer, E.W., 2008, Atlas of Migmatites: Canadian Science Publishing, doi:10.1139/9780660197876.

Sawyer, E.W., 2001, Melt segregation in the continental crust: distribution and movement of melt in anatectic rocks: Journal of Metamorphic Geology, v. 19, p. 291–309, doi:10.1046/j.0263-4929.2000.00312.x.

Sawyer, E.W., Cesare, B., and Brown, M., 2011, When the Continental Crust Melts: Elements, v. 7, p. 229–234, doi:10.2113/gselements.7.4.229.

Schmidt, M.W., 2015, Melting of pelitic sediments at subarc depths: 2. Melt chemistry, viscosities and a parameterization of melt composition: Chemical Geology, v. 404, p. 168–182, doi:10.1016/j.chemgeo.2015.02.013.

Schmidt, M.W., Vielzeuf, D., and Auzanneau, E., 2004, Melting and dissolution of subducting crust at high pressures: the key role of white mica: Earth and Planetary Science Letters, v. 228, p. 65–84, doi:10.1016/j.epsl.2004.09.020.

Shatsky, V.S., and Sobolev, N.V., 2003, The Kokchetav massif of Kazakhstan, *in* Carswell, D.A., Compagnoni, R., and Rolfo, F. eds., Ultrahigh Pressure Metamorphism, Mineralogical Society of Great Britain and Ireland, v. 5, p. 0, doi:10.1180/EMU-notes.5.4.

Sobolev, N.V., and Shatsky, V.S., 1990, Diamond inclusions in garnets from metamorphic rocks: a new environment for diamond formation: Nature, v. 343, p. 742–746, doi:10.1038/343742a0.

Spandler, C., and Pirard, C., 2013, Element recycling from subducting slabs to arc crust: A review: Lithos, v. 170–171, p. 208–223, doi:10.1016/j.lithos.2013.02.016.

Spandler, C., Yaxley, G., Green, D.H., and Scott, D., 2010, Experimental phase and melting relations of metapelite in the upper mantle: implications for the petrogenesis of intraplate magmas: Contributions to Mineralogy and Petrology, v. 160, p. 569–589, doi:10.1007/s00410-010-0494-2.

Stepanov, A.S., Hermann, J., Rubatto, D., Korsakov, A.V., and Danyushevsky, L.V., 2016, Melting History of an Ultrahigh-pressure Paragneiss Revealed by Multiphase Solid Inclusions in Garnet, Kokchetav Massif, Kazakhstan: Journal of Petrology, p. egw049, doi:10.1093/petrology/egw049.

Stöckhert, B., Trepmann, C.A., and Massonne, H.-J., 2009, Decrepitated UHP fluid inclusions: about diverse phase assemblages and extreme decompression rates (Erzgebirge, Germany): Journal of Metamorphic Geology, v. 27, p. 673–684, doi:10.1111/j.1525-1314.2009.00835.x.

Tacchetto, T., Bartoli, O., Cesare, B., Berkesi, M., Aradi, L.E., Dumond, G., and Szabó, C., 2019, Multiphase inclusions in peritectic garnet from granulites of the Athabasca granulite terrane (Canada): Evidence of carbon recycling during Neoarchean crustal melting: Chemical Geology, v. 508, p. 197–209, doi:10.1016/j.chemgeo.2018.05.043.

Tomkins, H.S., Powell, R., and Ellis, D.J., 2007, The pressure dependence of the zirconium-in-rutile thermometer: Journal of Metamorphic Geology, v. 25, p. 703–713, doi:10.1111/j.1525-1314.2007.00724.x.

Triebold, S., von Eynatten, H., and Zack, T., 2012, A recipe for the use of rutile in sedimentary provenance analysis: Sedimentary Geology, v. 282, p. 268–275, doi:10.1016/j.sedgeo.2012.09.008.

Tsuno, K., and Dasgupta, R., 2011, Melting phase relation of nominally anhydrous, carbonated pelitic-eclogite at 2.5-3.0 GPa and deep cycling of sedimentary carbon: Contributions to Mineralogy and Petrology, v. 161, p. 743–763, doi:10.1007/s00410-010-0560-9.

Tumiati, S., Recchia, S., Remusat, L., Tiraboschi, C., Sverjensky, D.A., Manning, C.E., Vitale Brovarone, A., Boutier, A., Spanu, D., and Poli, S., 2022, Subducted organic matter buffered by marine carbonate rules the carbon isotopic signature of arc emissions: Nature Communications, v. 13, p. 2909, doi:10.1038/s41467-022-30421-5.

Vernon, R.H., 2004, A practical guide to rock microstructure: Cambridge, UK ; New York, Cambridge University Press, 594 p.

Vielzeuf, D., Clemens, J.D., Pin, C., and Moinet, E., 1990, Granites, Granulites, and Crustal Differentiation, *in* Vielzeuf, D. and Vidal, Ph. eds., Granulites and Crustal Evolution, Dordrecht, Springer Netherlands, NATO ASI Series, p. 59–85, doi:10.1007/978-94-009-2055-2_5.

Walczak, K., Barnes, C.J., Majka, J., Gee, D.G., and Klonowska, I., 2022, Zircon age depth-profiling sheds light on the early Caledonian evolution of the Seve Nappe

Complex in west-central Jämtland: Geoscience Frontiers, v. 13, p. 101112, doi:10.1016/j.gsf.2020.11.009.

Wang, L., Kusky, T.M., Polat, A., Wang, S., Jiang, X., Zong, K., Wang, J., Deng, H., and Fu, J., 2014, Partial melting of deeply subducted eclogite from the Sulu orogen in China: Nature Communications, v. 5, p. 5604, doi:10.1038/ncomms6604.

Watson, E.B., Wark, D.A., and Thomas, J.B., 2006, Crystallization thermometers for zircon and rutile: Contributions to Mineralogy and Petrology, v. 151, p. 413–433, doi:10.1007/s00410-006-0068-5.

Whitney, D.L., and Evans, B.W., 2010, Abbreviations for names of rock-forming minerals: American Mineralogist, v. 95, p. 185–187, doi:10.2138/am.2010.3371.

Williams, I.S., and Claesson, S., 1987, Isotopic evidence for the Precambrian provenance and Caledonian metamorphism of high grade paragneisses from the Seve Nappes, Scandinavian Caledonides:

Yakymchuk, C., and Acosta-Vigil, A., 2019, Geochemistry of phosphorus and the behavior of apatite during crustal anatexis: Insights from melt inclusions and nanogranitoids: American Mineralogist, v. 104, p. 1765–1780, doi:10.2138/am-2019-7054.

Zack, T., Moraes, R., and Kronz, A., 2004, Temperature dependence of Zr in rutile: empirical calibration of a rutile thermometer: Contributions to Mineralogy and Petrology, v. 148, p. 471–488, doi:10.1007/s00410-004-0617-8.

Zhang, R.Y., Liou, J.G., and Ernst, W.G., 2009, The Dabie–Sulu continental collision zone: A comprehensive review: Gondwana Research, v. 16, p. 1–26, doi:10.1016/j.gr.2009.03.008.

Zheng, Y.-F., 2019, Subduction zone geochemistry: Geoscience Frontiers, v. 10, p. 1223–1254, doi:10.1016/j.gsf.2019.02.003.

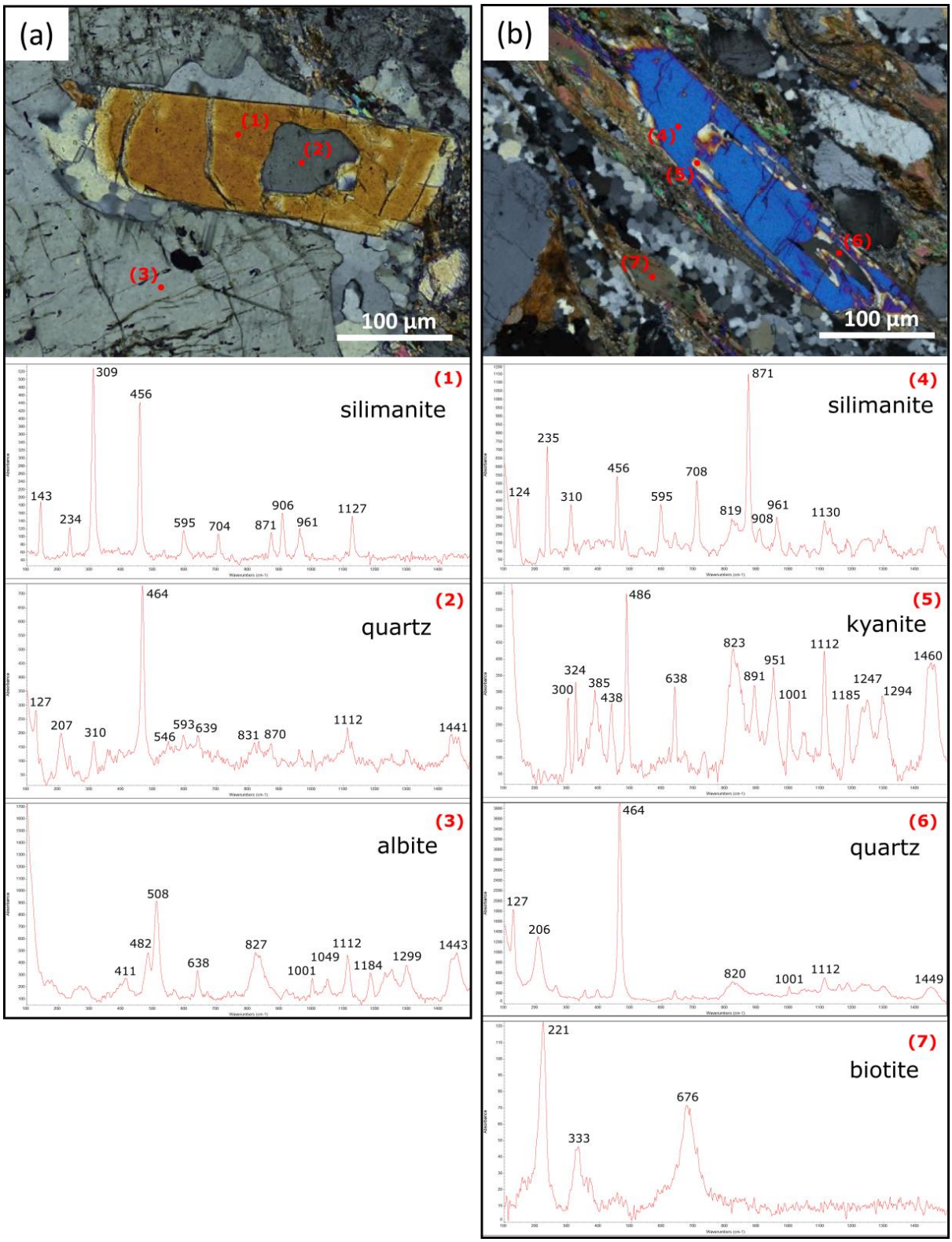

Figure A1 Representative Raman spectra (cm^{-1}) of minerals in the matrix, **(a)** – sillimanite crystal surrounded by melt pseudomorphs (Fig. 4.X), **(b)** – skeletal kyanite substituted by sillimanite

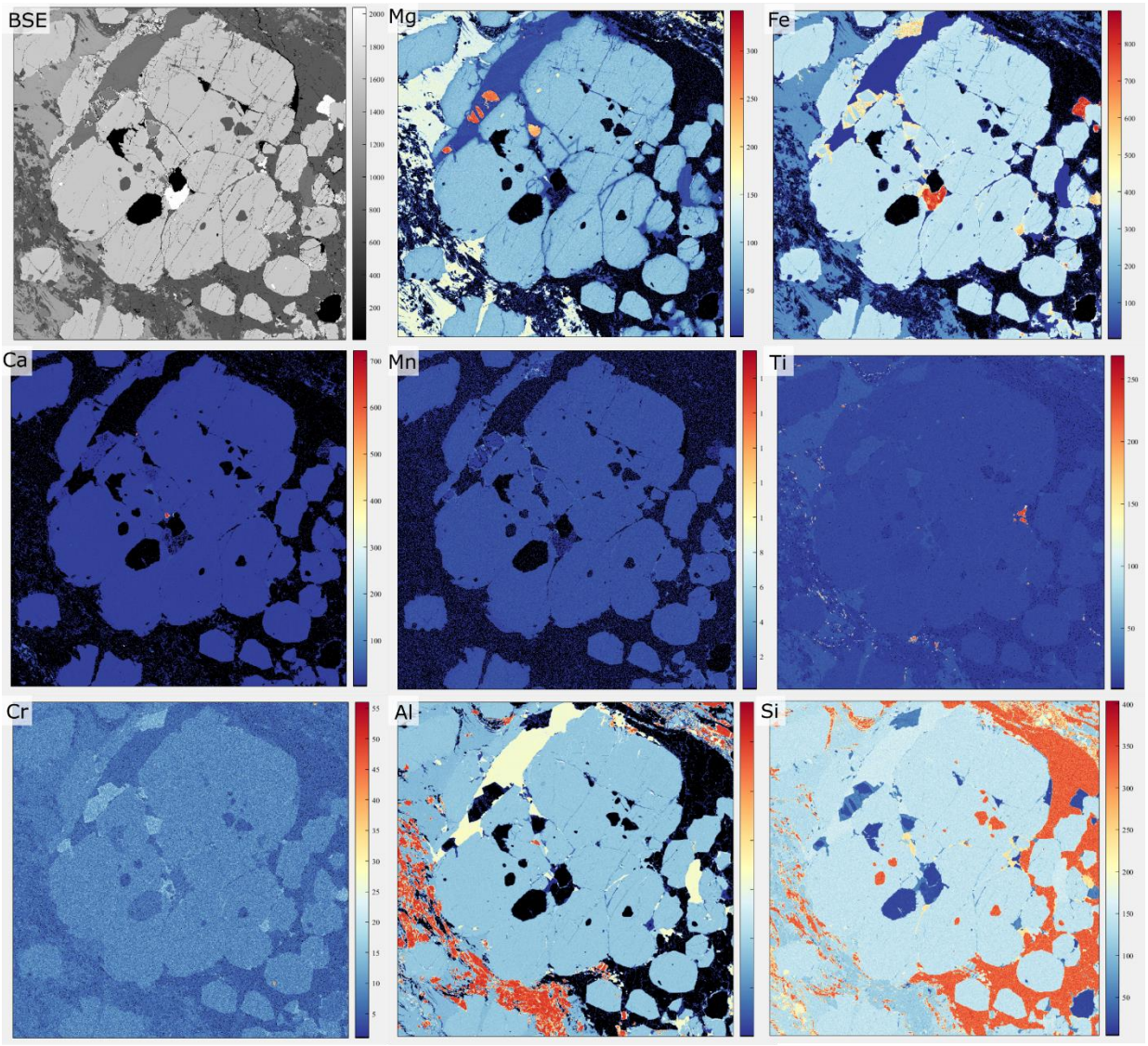

Figure A2 Major elemental map of garnet I.

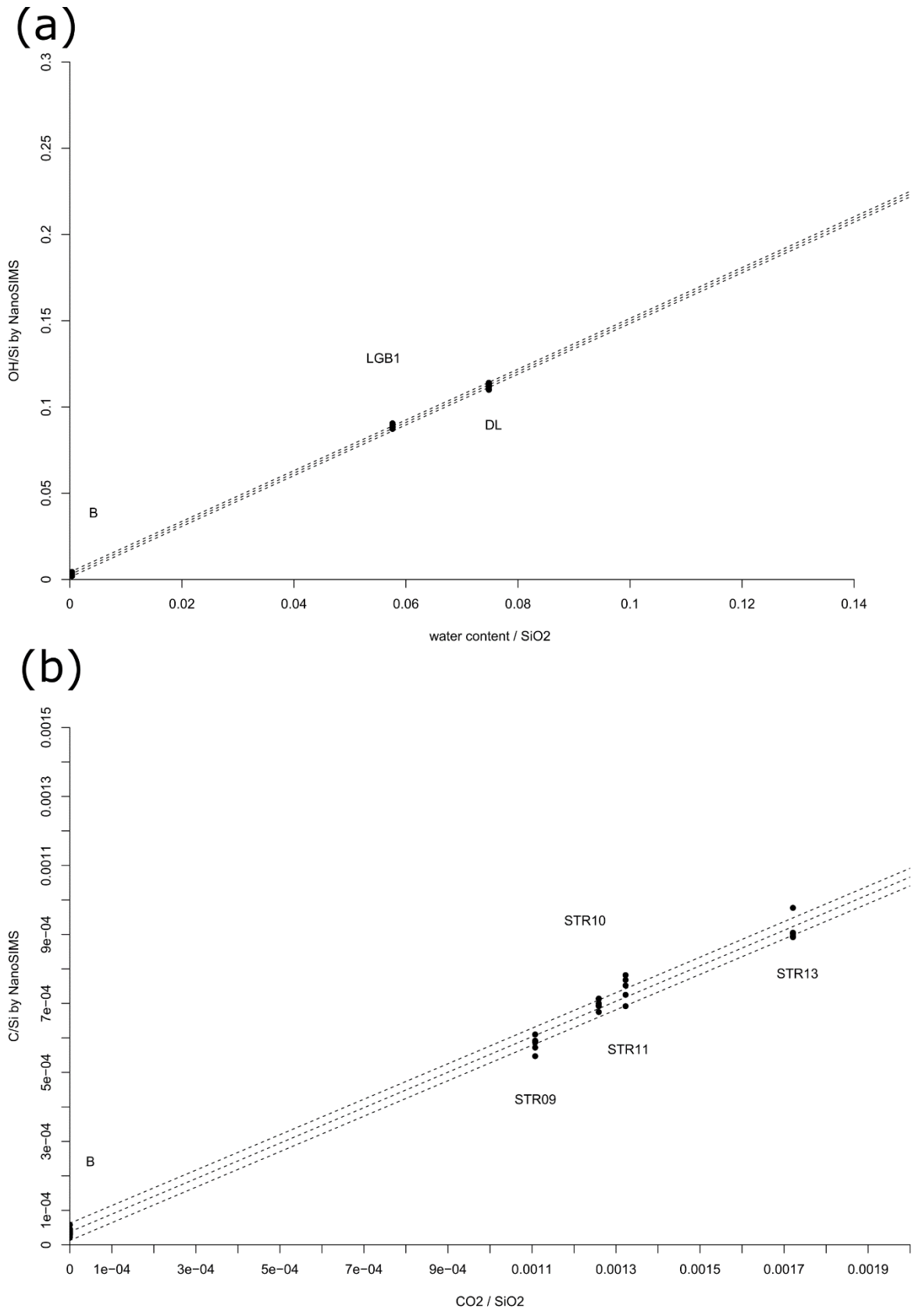

Figure A3 NanoSIMS correction curves.

Table A1 Chemical composition of glasses with bubble, quartz or muscovite.

No.	2	26	5	39	11c	7	11b	4b	11a	4a	9	35	34	77	23	12
Homogeneity	glass, Ms	glass, Ms	glass, Ms	glass, Ms	glass, Qz, Ms	glass Qz, Ms	glass, Qz, Ms	glass, Qz, Ms	glass, Qz, Ms	glass, Qz, Ms	glass, Qz, Gr	glass, Qz	glass, Qz	glass, bubble	glass, bubble	glass, bubble, Qz
P (GPa)	4	4	4	4	4	4	4	4	4	4	4	4.5	4.5	4.5	4	4
T (C)	850	850	850	850	900	850	850	850	850	850	850	900	900	900	900	850
Na_2O	3.00	3.81	4.60	1.72	2.27	2.82	3.34	1.89	5.55	2.89	2.44	1.61	1.96	1.42	2.51	0.43
$Al2O_3$	11.97	11.81	13.63	10.56	11.70	11.90	12.92	10.48	12.55	12.39	12.08	12.68	12.63	14.39	14.09	14.37
Cl	0.02	0.05	0.00	0.02	0.09	0.11	0.11	0.02	0.00	0.00	0.01	0.02	0.04	0.01	0.00	0.01
MnO	0.06	0.03	0.05	0.00	0.04	0.02	0.03	0.20	0.15	0.07	0.15	0.06	0.06	0.10	0.17	0.14
K_2O	4.36	3.90	3.80	8.51	7.17	3.22	4.03	5.02	5.50	6.41	9.01	5.97	6.00	7.98	5.43	7.49
MgO	0.36	0.19	0.77	0.06	0.85	0.62	1.23	0.10	0.85	0.10	0.24	0.15	0.09	0.26	0.72	0.66
SiO_2	77.05	77.32	74.06	77.46	75.42	77.82	74.27	78.09	71.94	76.38	73.15	77.53	76.84	71.51	74.38	73.10
TiO_2	0.93	0.05	0.11	0.05	0.03	0.48	0.33	0.42	0.06	0.01	0.15	0.00	0.10	0.16	0.02	0.00
FeO	1.84	2.61	2.66	1.25	2.14	2.47	3.22	3.42	2.86	1.39	2.41	1.77	2.10	4.03	2.51	3.42
CaO	0.41	0.11	0.19	0.35	0.25	0.24	0.29	0.26	0.42	0.10	0.20	0.11	0.11	0.10	0.15	0.27
P_2O_5	0.00	0.12	0.14	0.01	0.04	0.29	0.23	0.10	0.12	0.25	0.16	0.09	0.08	0.02	0.04	0.10
EMP Total	91.16	89.21	83.64	90.25	88.61	82.29	87.93	86.92	87.44	95.84	91.24	90.58	91.57	94.99	93.20	94.00